The use of subwavelength structures to control and enhance the photoacoustic effect



Isobel Patterson

Jesus College

Department of Engineering Science

University of Oxford

A thesis submitted for the degree of

Doctor of Philosophy

Trinity 2023

Acknowledgements

Thank you to my supervisor, Prof. Paul Stavrinou, for his help and guidance throughout my DPhil studies.

Abstract

The photoacoustic effect describes the conversion of light to sound, via thermoelastic expansion, and is used extensively in cross-media applications as it combines the favourable properties of light in one medium with the favourable properties of sound in the other. Photoacoustic composites are used for efficient photoacoustic conversion and can be made from planar multilayered structures, comprised of thin layers of optically absorbing media, separated by layers of a thermally-responsive medium. The aim of this project was to formulate a one-dimensional model capable of simulating the acoustic signal generated from a multilayered structure with several absorbing layers. Then, using the model, the effect of sub-wavelength structures on the generated acoustic signal was investigated for weakly- and strongly-absorbing layers. The transfer-matrix method was used to solve the governing photoacoustic wave equation in the frequency domain and the source function of the second-order differential equation was kept as general as possible so that the user could choose any function to describe the optical absorption profile of the structure. The model was verified by comparing its results with those from previous studies. It was found that acoustic resonant effects could be induced in structures with optically-thin or optically-thick absorbers but that the effect was more pronounced in the spectra of optically-thick absorbers. Furthermore, the features of the frequency spectrum could be explained by considering the poles and zeros of the transfer-matrix when source terms were included. Thus, these observations stimulated the design of a photoacoustic structure with enhanced directivity by using an acoustic high-reflectance coating. The simulated structure was capable of increasing the amplitude of the generated acoustic signal by about 15% at a target frequency, compared to previous methods. These findings indicate that as new photoacoustic composites have reduced dimensions (<10nm), the resonant properties of both light and sound could be utilised to enhance the conversion from optical to acoustic energy.

Contents

1 Introduction **1**

2 Literature review **4**

2.1 The photoacoustic effect 4

2.2 Applications of photoacoustics 5

2.2.1 Ultrasound 5

2.2.2 Gigahertz and beyond 7

2.3 Recent research advances 7

2.3.1 Photoacoustic composite materials 8

2.3.2 Analytical models 12

2.3.3 Numerical models 15

2.4 Measuring sound 15

2.4.1 Pressure-to-voltage conversion 16

2.4.2 Acoustic energy and the photoacoustic conversion efficiency . 17

2.5 Summary 18

3 The photoacoustic model **19**

3.1 Previous work 20

3.2 The transfer-matrix model 21

3.2.1 Boundary conditions 22

3.2.2 Reflection and transmission at a single interface 25

3.3 Acoustic energy 29

3.4 The heating function 31

3.4.1 The absorption profile and local light fluence 31

3.4.2 The input light function 34

3.5 Resolution and the numeric inverse Fourier transform 36

3.6 Summary 40

4 Single acoustic source **41**

4.1 No mechanical barriers 43

4.2 Mechanical barriers 48

4.2.1 One mechanical barrier . . . 51
4.2.2 Multiple mechanical barriers . . . 53
4.3 Summary . . . 59

5 Distributed heat sources **61**
5.1 No mechanical barriers . . . 64
5.2 Mechanical barriers . . . 70
5.3 Summary . . . 76

6 Sub-wavelength photoacoustic structures **79**
6.1 Anti-reflection coatings . . . 80
6.1.1 Quarter-wave plates . . . 81
6.1.2 Symmetric multilayers . . . 86
6.2 High-reflectance coatings . . . 91
6.3 Using subwavelength layers to improve emission efficiency . . . 99
6.3.1 Subwavelength structures with distributed heat sources . . . 106
6.4 Summary . . . 107

7 Discussion and future work **110**
7.1 Limitations of the model . . . 111
7.1.1 Heat conduction and viscosity . . . 111
7.1.2 Acoustic attenuation . . . 112
7.1.3 Acoustic dispersion . . . 113
7.2 Resonant effects . . . 115
7.2.1 Acoustic resonance . . . 115
7.2.2 Optical resonance . . . 121
7.3 The short- and long-pulse regime . . . 125
7.4 Further work . . . 127
7.5 Summary . . . 128

8 Conclusions **131**

A Deriving Fourier transform pairs of generated acoustic signals **134**
A.1 A single exponential pulse . . . 134
A.2 Five rectangular pulses . . . 136
A.3 Five exponential pulses . . . 137

List of Publications **141**

References **141**

List of Figures

2.1 The photoacoustic effect 5
2.2 Underwater communication by photoacoustic effect 7
2.3 Acoustic sasers 8
2.4 Photoacoustic composite with optical resonant cavity 11
2.5 Asymmetry in acoustic impedance 14
2.6 Modelling a piezoelectric transducer 17

3.1 A multi-layered photoacoustic structure with N layers 22
3.2 Defining the coefficients A_q and B_q 24
3.3 Defining the coefficients A_{q+1} and B_{q+1} 24
3.4 A single interface at $z = z_0$ 26
3.5 Reflections at the copper-water interface: before collision (top panel) the (Gaussian) acoustic pulse propagates to right in layer 0, with amplitude p_0. After collision (bottom panel), the acoustic signal has a reflected component, with amplitude, $-0.93p_0$, and a transmitted component with amplitude $+0.07p_0$, which propagates to the right in layer 1. 28
3.6 Local light fluence, Q_q 32
3.7 The heating function 33
3.8 External acoustic source 35
3.9 The acoustic signal detected at $z = z_s$ in the structure shown in the bottom panel of Fig. 3.8a. 36
3.10 Resolution in the time domain 38
3.11 Spatial resolution 39

4.1 Increasing the optical thickness 42
4.2 The heating function, $h(z)$, in the absorber (layer 1, shaded) depends on the optical thickness, αd. 43
4.3 The effect of optical thickness on the generated acoustic signal in the time domain 44

4.4 The effect of optical thickness on the generated acoustic signal in the frequency domain 47
4.5 Reflections at different backing layers 49
4.6 Two mechanical barriers surround the epoxy absorber (shaded) which is irradiated by light, with fluence, Q_0, from the left. A detector is positioned at $z = z_s$ to record the generated acoustic signal. 50
4.7 Superposition in the long-pulse regime 50
4.8 Reflections at a mechanical barrier 51
4.9 Detected pulse width 52
4.10 An illustration of repeated reflections 53
4.11 Acoustic impedance mismatch 55
4.12 A moveable absorber 57
4.13 Controlling time delay 58

5.1 Mechanical barriers vs. distributed heat sources 62
5.2 Distributed heat sources and no mechanical barriers 65
5.3 Optically thin absorbers 66
5.4 Optically thick absorbers 68
5.5 Distributed heat sources with mechanical barriers 72
5.6 Optically thick absorbers with mechanical barriers 73
5.7 The effect of high and low acoustic impedance mismatch 75
5.8 The multilayered acoustic structure with five alternating layers of absorbing and transparent material, with high and low acoustic impedance, respectively 78

6.1 Out of phase reflections 82
6.2 Zero reflectance 84
6.3 Varying the quarter-wave plate thickness 85
6.4 Comparing the performance of two quarter-wave plates vs. a single quarter-wave plate 86
6.5 Finding the propagation matrix for a single layer irradiated by an external acoustic source 87
6.6 Finding the propagation matrix for a symmetric multilayer irradiated by an external acoustic source 88
6.7 Reflectance of symmetric multilayer 89
6.8 Schematic of symmetric structures 90
6.9 High-reflectance coatings 91

6.10 The performance of high-reflectance coatings 93
6.11 Designing high-reflectance coatings 94
6.12 Low transmittance 95
6.13 Revisiting the two-absorber structure from Ch 5 97
6.14 A two-stack symmetric multilayer 98
6.15 Controlling reflections 100
6.16 Improving emission efficiency 101
6.17 The heating function and acoustic impedance mismatch of the structures shown in Fig. 6.12 102
6.18 Increased reflectance 103
6.19 Positioning the reflective surface 104
6.20 Effect of distributed heat sources on emission efficiency 106

7.1 Acoustic attenuation 113
7.2 Demonstrating the effect of non-dispersive materials on performance of high-reflectance coatings 114
7.3 Resonant effects from optically-thin and optically-thick absorbers . . 117
7.4 Multilayered structures with and without acoustic sources 119
7.5 The effect of zeros in the frequency response function 121
7.6 Far-field optical absorption 122
7.7 Distributed heat sources with optical reflections 123
7.8 Enhanced optical absorption due to optical interference 123
7.9 Optical energy with and without reflections 124
7.10 Highly-absorbing layers in the short-pulse regime 126

A.1 Segmenting and shifting a single pulse 135
A.2 Segmenting and shifting five pulses 137

Chapter 1

Introduction

The aim of this research was to investigate the effect of using subwavelength structures, both optical and acoustical, to generate an acoustic signal using the photoacoustic effect. By formulating a novel one-dimensional model, the frequency-dependent behaviour of subwavelength structures has been explored and the material properties and structural design of a thin-film photoacoustic structure have been optimised to improve the emission efficiency of the signal at a target frequency.

The photoacoustic effect describes the conversion of light to sound via thermoelastic expansion, and has been used in a range of applications, from underwater communications [1,2] to biomedical imaging [3,4]. In general, these applications make use of the favourable properties of light in air, i.e., low attenuation and high speed, with the high penetration depths and reduced scattering of sound propagating in water (or biological tissue). Most applications require acoustic signals in the ultrasound range (>20 kPa) which can be generated by nanosecond laser pulses [5].

Thus, in order to produce high-amplitude, high-frequency acoustic signals, a photoacoustic structure must have good optical absorption properties and a strong thermal-expansion response, characterised by the optical absorption coefficient and thermal expansion coefficient, respectively. Unfortunately, materials with a high optical absorption coefficient usually have a poor thermal expansion coefficient, and vice-versa. Therefore, composites, which combine a material with a good optical absorption coefficient and another with a strong thermal expansion coefficient, have commonly been used in photoacoustic generation. Layers of the optically-absorbing material are sandwiched between optically-transparent, but thermally-responsive, media and advancements in nanofabrication have led to exciting developments in the optical absorption properties of these composites, including the use carbon nanotubes [6–8] or gold nanoparticles [9–11]. However, models that are capable of simulating these structures are less advanced. There are several analytical models, but these only

include a single absorbing layer [12–22]. Numerical models have been derived for structures with multiple absorbing layers but have lacked generality. In Sun et al [23], the absorbing layers were assumed to be optically-thin and thus the acoustic signal generated was always constant, and in work by Hu et al [24, 25], the absorbing layers had exponentially-decaying absorption profiles, i.e., the layers could not be weakly-absorbing, or have an absorption profile influenced by optical interference effects. Therefore, this work aims to fill this gap by formulating a one-dimensional model, capable of simulating the generated acoustic signal from a multilayered structure with distributed heat sources and unlike previous work, the formulation retains its generality such that the strength of the absorbing layers has not been limited.

In summary, the objectives of the thesis are:

1. to derive a one-dimensional model capable of simulating a multilayered structure in which any layer is optically absorbing and the optical absorption can be weak or strong and can include any enhancements to the absorption profile due to interference effects;

2. to formulate the model in the frequency-domain such that the resonant behaviour of the generated acoustic signal can be explored and understood, and;

3. to use the formulated model to optimise the efficiency of a photoacoustic structure using subwavelength layers and careful material selection.

The transfer-matrix method has been used, which is ideal for modelling thin-film multilayered structures, and the coefficients of the left- and right-propagating components of the generated acoustic signal in every layer of a structure have been found. The inclusion of a local light fluence means that the attenuation of light in any layer can be modelled by either making it constant (optically-thin absorbers), using the commonly-used assumption that it follows Beer's Law of absorption (optically-thick absorbers), or by using a more realistic function that takes in account the interference of light. The effect of optically-thin versus optically-thick absorbers on the generated acoustic signal has been investigated in the time and frequency domain and it was found that additional resonant peaks appear in the frequency spectrum of structures with optically-thick absorbers. The effect of acoustic subwavelength layers on the frequency spectrum of the generated acoustic signal has also been explored and by using a high-reflectance coating, comprised of a stack of quarter-wave plates, the photoacoustic signal propagating in one direction can be enhanced at a target frequency.

A literature review can be found in the next chapter (**Chapter 2**) and includes the theory of the photoacoustic effect, its applications, and recent advances in material research. A discussion of the previous work on modelling the photoacoustic effect in multilayered structures has also been covered. In **Chapter 3**, the transfer-matrix method has been used to solve the governing photoacoustic equation when heat transport has been neglected. The heating function, which represents the source term in the governing equation, has been discussed and the importance of the local light fluence, which describes the attenuation of light through the structure, has been highlighted. In this way, objective 1 has been attained. In **Chapter 4**, the model has been used to simulate the acoustic signal generated by a single acoustic source for a structure with and without mechanical barriers, where the absorbing layer is optically-thin and thick, and the resulting differences in the generated acoustic signal in the time and frequency domain have been investigated. In **Chapter 5**, the photoacoustic structures modelled have several optically absorbing layers and the effect of mechanical barriers and the optical thickness of the absorbing layers on the generated acoustic signal have been explored. With distributed heat sources, interesting resonant behaviour appears in the frequency spectra of the generated signals and thus, in **Chapter 6**, subwavelength acoustic structures have been analysed in order to satisfy objective 2. A subwavelength structure has been used to increase the amplitude of the photoacoustic signal detected on one side of the structure at a target frequency and hence, the third objective has been achieved. Finally in **Chapter 7**, the work presented in the thesis has been discussed, placed in the context of existing research, and further work has been identified. Conclusions have been given in **Chapter 8**.

Chapter 2

Literature review

2.1 The photoacoustic effect

Acoustic waves can be produced from pulsed incident light. Photoacoustic (PA) conversion occurs when incident light is absorbed by a medium. The absorbing medium experiences a temperature rise and transfers heat to the surrounding media. As the materials warm and then cool, they expand and contract, resulting in pressure waves. The process is shown in Fig. 2.1 and can be broken down into four steps: irradiation, absorption, heat transfer and expansion, and generation. At each step, optimisations can be made to improve the efficiency of the process. First, the properties of the input light source must be carefully chosen. Increasing the applied optical energy, or laser fluence, will result in larger photoacoustic amplitudes. However, in practice, the laser fluence is limited by the thermal threshold of the material, beyond which the material will melt and a plasma will form [26]. The duration of the input light pulse also controls the shape and bandwidth of the generated acoustic signal and in general, nanosecond laser pulses generate acoustic signals in the mega-hertz (MHz) frequency range [5]. Then, the absorption of light is dependent on the optical thickness of the absorbing material. The optical thickness is defined as the product of the optical absorption coefficient, α, and the thickness of the absorber, d and an absorber with a very large optical thickness, i.e. $\alpha d >> 1$, will absorb all the applied optical energy. Finally, most light-absorbing materials have low thermal expansion coefficients. However, if the absorber has a low specific heat capacity then the heat energy can be transferred to the surrounding media. A surrounding media with a favourable thermal expansion coefficient will produce a strong thermal response and therefore, a large photoacoustic amplitude. In this way, composites which combine a light-absorbing material with a thermally-responsive medium are ideal photoacoustic convertors.

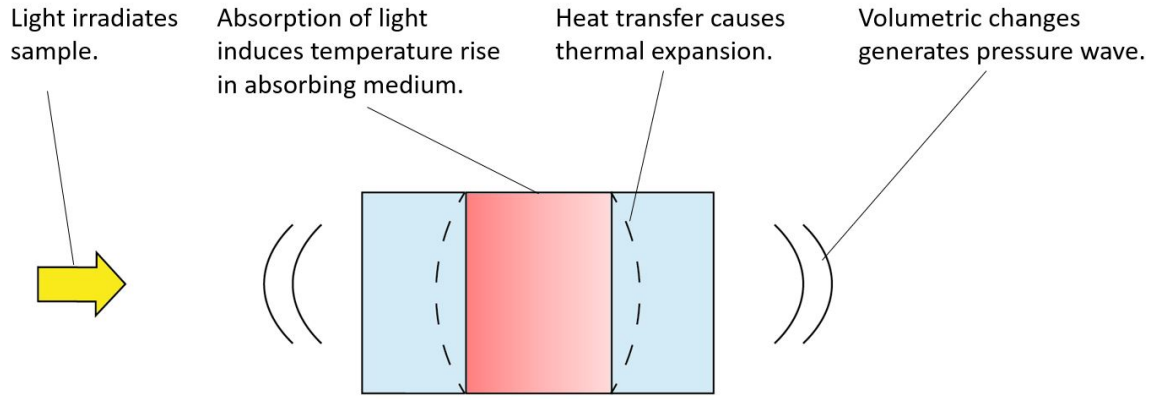


Figure 2.1: The photoacoustic effect: when light is absorbed by a material, it experiences a temperature rise. After heat transfer to the surrounding media, the resultant thermal expansion of the media generates a pressure wave.

2.2 Applications of photoacoustics

The PA effect was first observed by Alexander Graham Bell in 1880 and stimulated a brief period of interest in the phenomenon [27]. The PA effect was first applied for analysis of gases. However, it wasn't until the early 1970s that the PA effect provided a competitive alternative to conventional gas spectroscopy methods. By using a tunable laser, Kreuzer and Patel [28] were able to detect nitric oxide from smaller volumes of polluted air. The improved method of gas spectroscopy enabled more sensitive measurements to be made with shorter integration times. Furthermore, in 1973, the PA effect in solids was used by Rosencwaig [29] to produce an optical absorption spectra for any type of solid; and because the detected acoustic signal was produced only by absorbed light, the complications, which normally arise in conventional techniques from scattered light, were avoided.

2.2.1 Ultrasound

Since establishing its robustness against scattering, the photoacoustic effect has experienced a surge in popularity in biomedical imaging [3,4]. Conventional light-based imaging techniques, such as optical microscopy, suffer from poor penetration depths in biological tissue due to scattering [30]. In contrast, ultrasound-based imaging modalities have greater penetration depths but rely on the acoustic mismatch between different tissues. The mechanical properties of different soft tissue structures do not differ enough to produce a significant acoustic mismatch. Thus, photoacoustic imaging combines the high optical absorption contrast of light-based modalities with

the deeper penetration depth of sound waves to produce high resolution images.

Photoacoustic sources also provide an attractive alternative to piezoelectric transducers operating at frequencies higher than 30MHz. At these frequencies, piezoceramic elements must be micron-scale and require individual electrical connections with large amounts of cabling. In contrast, a photoacoustic array overcomes these difficulties because the transducer surface does not need to be diced and no electrical connections are needed [9]. Furthermore, recent advances in nanofabrication methodologies have allowed photoacoustic composites to be coated on the ends of optical fibres and used as miniaturised all-optical ultrasound transmitters in minimally invasive sensing applications [7, 31]. Rather than a planar surface, the high-amplitude photoacoustic signals needed for shock waves or cavitation can be produced by using a photoacoustic transmitter coated on a concave lens to create high-level focusing [5, 32, 33].

Underwater communication and imaging systems also rely on ultrasound waves. Like in biological tissue, sound has relatively low attenuation and long penetration depths in water, compared to electromagnetic radiation, and so SONAR systems provide high-resolution images of the subsurface with long-range capabilities [1]. However, such systems are usually towed on ships and so covering large areas is costly and time-consuming. Mounting the imaging system on an airborne device would improve coverage, however, the acoustic impedance mismatch between water and air is large and most of the acoustic energy would be lost at the water-air interface [2]. In contrast, electromagnetic radiation travels well in air and thus photoacoustic conversion from light to sound at the air-water interface provides a promising solution to cross-medium communication. Various designs have been considered. In work by Ji et al. [2], a low cost relay device was placed on the water surface. The highly-efficient passive relay absorbed light irradiated from an aircraft and generated a pulsed ultrasound signal that was detected by a submarine.

Fitzpatrick et al [1] used the water itself as a photoacoustic source (Fig. 2.2). An unmanned airborne vehicle irradiated the water with an intensity-modulated laser to induce the generation of acoustic signals. The acoustic signals propagated through the water and were reflected by targets. Acoustic waves arriving back at the airborne vehicle were detected using highly-sensitive air-coupled capacitive micromachined ultrasonic transducers (CMUTs), which were capable of detecting sound waves even after the transmission losses at the water-air interface.

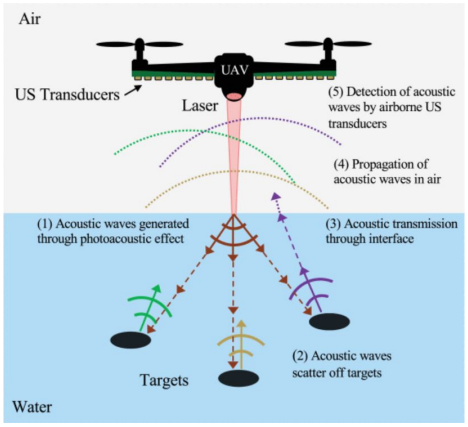


Figure 2.2: Figure from Ref. [1]: an unmanned airborne vehicle (UAV) irradiated the water surface with light. The generated acoustic signals propagated through the water and any reflected components travelled back toward the UAV. Due to the significant energy losses from sound transmission through the water-air interface, air-coupled capacitive micromachined ultrasonic transducers (CMUTs) were needed to detect the incoming acoustic signal.

2.2.2 Gigahertz and beyond

Subwavelength optical structures have been used to create mirrors, filters and cavities, and enhance the performance of the structure [34–36]. Their acoustic equivalent has often lagged behind. However, as telecommunications has progressed into 5G and beyond, so has the need for radio-frequency filters that perform well at giga-hertz (GHz) frequencies [37–39]. Advancements in nanofabrication have enabled progress toward the generation and detection of acoustic waves in the giga- and tera-hertz frequencies range. For example, significant developments in sasers, the acoustic laser, have been achieved using molecular beam epitaxy to produce multilayered structures of GaAs and AlGaAs. Two acoustic Bragg mirrors, comprised of up to 40 periods of alternating layers of GaAs and AlGaAs, reflected acoustic waves back and forth within the acoustic cavity (shown in Fig. 2.3) and were used to increase reflectance at a target frequency of 325GHz [40,41]. The result was coherent acoustic emission in frequency ranges up to tera-hertz (THz), depending on the thickness of the alternating layers.

2.3 Recent research advances

All photoacoustic applications require highly efficient photoacoustic conversion and so high light absorption and a large thermoelastic expansion is desired. Unfortunately,

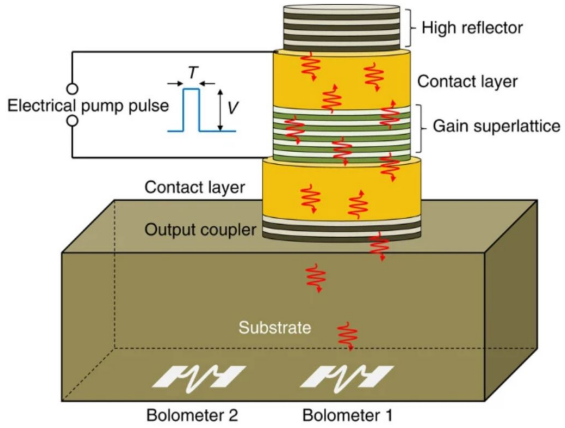


Figure 2.3: Figure from Ref. [41]: the acoustic saser uses two highly-reflecting mirrors to increase the acoustic energy in the cavity, such that emission in the tera-hertz frequency range is possible.

most materials with good optical absorption coefficients have very low thermal expansion coefficients. For example, gold has an optical absorption coefficient of $47 \times 10^6 \mathrm{m}^{-1}$ (at a wavelength of $\lambda = 500\mathrm{nm}$) but a thermal expansion coefficient of $14 \times 10^{-6}\mathrm{K}^{-1}$. In contrast, the commonly-used polymer, polydimethylsiloxane (PDMS), is optically transparent, i.e, has an optical absorption coefficient of almost zero, but has a thermal expansion coefficient of $920 \times 10^{-6}\mathrm{K}^{-1}$ [42]. However, by combining the two materials, a composite can be created with favourable optical absorption and thermal expansion coefficients.

2.3.1 Photoacoustic composite materials

Similar composites have been created using different metal absorbers and polymer substrates. A table of photoacoustic composites can be found in Table 2.1 and excellent review papers can be found in Refs. [5, 32, 43]. In general, the light-absorbing component is either carbon-based or metal-based. Carbon-based materials have broadband optical absorption while metals have resonant characteristics that result in frequency-dependent optical absorption [5]. The optically-transparent, but thermally-responsive material, is usually a polymer and polydimethylsiloxane (PDMS) is most commonly used. It has a ratio of thermal expansion coefficient to specific heat capacity that is four times greater than other widely-available polymers, such as parylene and polyimide [26] and is also easily shaped and patterned at the nanoscale and has good adhesion to glass [43].

	Authors	Composite	Peak pressure/MPa	Laser fluence/mJ cm^{-1}	τ_p/ns	Coating thickness/μm	Bandwidth/MHz	Fabrication	Coating substrate
Carbon-based	Biagi et al. [31]	Graphite epoxy	0.02	2.47	6	10-50	10-50 (-3dB)	-	planar
	Buma et al. [44]	CB	-	10.4	10	25	50	spin-coating	planar
	Huang et al. [45]	CS	4.8	3.57	6	18	21 (-3dB)	spin-coating	planar
	Baac et al. [6, 46]	CNT	-	42.4	6	2.6	120	spin-coating	planar
	Colchester et al. [47]	Solution CNT	4.5	36.3	2	<20	10 (-3dB)	dip-coating	fibre
	Noimark et al. [7]	CNT gel	21.5	33.1	2	20	39.8	dip-coating	fibre
	Hsieh et al. [48]	CNF	12.15	3.71	4	57.9	7.84 (-6dB)	electro-spinning	planar
	Hwan Lee et al. [49]	rGO	9	56	5	20-200	10 (-3dB)	spin-coating	planar
	Silva et al. [8]	functionalised CNT	1.69	50	0.03	38	170 (-6dB)	casting	planar
	Vella et al. [32]	AuNFs	11	228	12	17	14 (-6dB)	rotary evaporator	planar
	Vella et al. [32]	AuNFs	12	5	-	17	21.5 (-6dB)	spin-coating	concave lens
Metal-based	Hou et al. [9]	2D gold	1.5	0.2	5	∼5	>50	nanoimprint lithography + electron beam evaporator	planar
	Hou et al. [10]	3D gold	-	26	5	∼4	57 (-6dB)	nanoimprint lithography + electron beam evaporator	planar
	Wu et al. [11]	AuNP	0.189	13	150	450	3.1 (-3dB)	-	planar
	Kang et al. [26]	Cr	-	20	5	0.1	-	sputtered	planar
	Lee et al. [50]	Cr	1.82	2.35	6	0.1	-	magneton sputter + spin-coating	planar
	Zheng et al. [51]	two Cr sandwiched between PDMS	-	-	1000	0.03, 0.1	-	magneton sputter + spin-coating	planar
	Du et al. [33]	Lead halide perovskite	15	3	-	323	40.8 (-6dB)	spin-coating	planar + concave

Table 2.1: Photoacoustic structures: the properties of the carbon-based and metal-based composites with a PDMS filler. CB = carbon black, CS = candle soot, CNT = carbon nanotubes, rGO = reduced graphene, AuNF = gold nanoflakes, AuNP = gold nanoparticles, Cr = chromium. The table is based on similar compilations by Lee et al [5] and Noimark et al [43] and includes more recent work.

The use of subwavelength structures, or metamaterials, has been shown to improve optical absorption and heat transfer to the polymer layer in such composite materials [52–68]. The term 'subwavelength' here refers to a general class of materials with features that are smaller than the wavelength of the incident light. The material can be a conductor, insulator, or semiconductor. The term 'metamaterial' is also used to describe materials with subwavelength structures. Such structures are known to enhance incident optical fields [69–75], either resonantly or with surface plasmon polaritons, over a minimal spatial distance – an essential requirement for efficient photoacoustic generation.

In Hou et al [10], the amplitudes of optically-generated ultrasound signals produced from different thicknesses of black PDMS films were investigated. The films were a mixture of PDMS and 45nm particles of carbon black. When the film thickness was decreased from 25μm to 11μm, the amplitude of the PA signal increased and the thermoelastic conversion efficiency increased by 11dB. Furthermore, in a second study by Hou et al. [9], the PA signal from the 11μm-film of black PDMS was compared to that from a 2D array of gold nanoparticles. The gold discs, 20nm thick with a diameter of 128nm, were coated in a 4.5μm-thick layer of PDMS. The thinner, gold nanostructure produced a higher peak PA amplitude than the black PDMS film, despite not absorbing all the optical energy from the laser. The improvement in acoustic amplitude was particularly significant at resonant frequency due to the excitation of surface plasmons.

More recent work has focused on the use of carbon nanotubes (CNTs) as a light-absorbing filler. In Lee et al [5], forests of multiwalled (MW) CNTs were submerged in PDMS. A low density forest of CNTs allowed greater PDMS infiltration and enabled more effective heat transfer. However, the CNTs absorbed less optical energy at a lower density. Careful preparation of the CNT films was crucial to prevent agglomeration and required high temperatures for chemical vapour deposition. In another study, Lee and Guo [50] avoided these fabrication challenges while still creating subwavelength structures, by using thin metal layers instead. By keeping the absorbing layers as thin as possible and hence reducing the heat capacity of the metal, heat dissipation to the surrounding PDMS was maximised. However, the thin layers were less optically absorptive. Lee and Guo incorporated an optical cavity into the structure to reduce these losses. The reference structure consisted of three layers: an 100nm-thick Chromium (Cr) layer, between a layer of glass substrate on the irradiated side, and water on the far side and was compared to three other structures, designed to enhance PA conversion (Fig. 2.4).

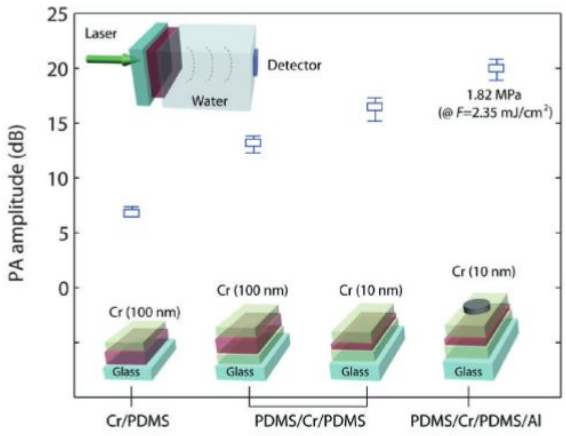


Figure 2.4: Figure from Ref. [50]: the performance of Lee et al's reference structure of 100nm-thick chromium, sandwiched between glass and water, was compared to three other structures: with one additional PDMS layer, with two PDMS layers, and with two PDMS layers and an aluminium film. The optimised structure, with the aluminium film generated the highest photoacoustic amplitude (1.82MPa).

In the first sample structure, a layer of PDMS (200nm-thick) was added to separate the glass substrate from the 100nm-thick Cr layer. The polymer layer had a higher thermal expansion coefficient than the glass substrate and so the heat dissipated from the absorber was more efficiently converted to sound. As a result, the photoacoustic amplitude increased by 6dB relative to the reference structure. In the second sample structure, the thickness of the Cr layer was reduced to 10nm. The optical absorption decreased but the improvement in PA generation due to the insertion of the PDMS layer between the metal and the glass substrate compensated for the loss in energy absorbed. Finally, in the third structure, an optical cavity was created. An aluminium reflector (50nm-thick) was placed on the far side of the structure, separated from the Cr layer by an additional layer of PDMS. The thickness of this 'top' layer of PDMS controlled the cavity length and was carefully chosen to cause constructive interference (250nm-thick). At optical resonance, the optical absorption of the Cr layer increased to 90% but interestingly, doubling the light absorbed by the Cr layer did not cause the photoacoustic signal amplitude to double.

The reflection of light was also used by Zheng et al [51] to enhance the optical absorption in an ultrathin layer of Cr. A 3nm-thick layer of Cr was separated from a second 100-nm thick layer of Cr by a thin PDMS layer (thickness of 73nm). When the 3nm-thick layer of Cr was irradiated by light, any unabsorbed light propagated into the PDMS layer and was then reflected by the 100nm-thick Cr. Compared to a single layer of 100nm-thick Cr, the absorbance of the three-layer sample increased from

about 60% to between 80-90%, depending on the wavelength of light. Furthermore, heat transport across the thin PDMS layer was fast, resulting in a more uniform temperature distribution, and hence a larger photoacoustic amplitude was detected.

In these studies, reflected light was used to improve the optical absorption of the structure and hence, increase the amplitude of the generated acoustic signal. However, the use of acoustic reflections to enhance the detected signal has been less well-documented. Indeed, beyond using a simple backing layer to reflect acoustic components travelling in the opposite direction to a detector [15, 76], little work has been done to improve the photoacoustic signal in one direction, generated from a planar stack of thin-films.

2.3.2 Analytical models

The formulation of photoacoustic models has been used to aid the understanding of photoacoustic generation in a number of applications, e.g., the calibration of hydrophones [15], spectroscopy [17, 18, 77], the design of ultrasonic sensors [22], and the reconstruction of absorber geometry for photoacoustic radar [12]. An analytical model can be used to solve the governing photoacoustic wave equation (Eq. 2.1) for a structure with a single absorbing layer by means of Green's functions, [15, 16, 18, 19], Laplace transform [13, 14], or Fourier transform [12, 17, 20–22]:

$$\left[\nabla^2 - \frac{1}{c^2}\frac{\partial^2}{\partial t^2}\right] p(\mathbf{r}, t) = -\frac{\beta}{C_p}\frac{\partial H(\mathbf{r}, t)}{\partial t} \tag{2.1}$$

where c, β, and C_p are the speed of sound [ms^{-1}], the thermal expansion coefficient [K^{-1}], and the specific heat at constant pressure [J kg^{-1} K^{-1}] of the irradiated material, respectively. The input optical energy density per unit time is represented by H [J m^{-3} s^{-1}].

The solution to Eq. 2.1 takes the form of a general solution, with a left- and right-travelling component, plus a particular solution that depends on a source term, $H(\mathbf{r}, t)$. Most models assume that the source term, or heating function, is separable and thus can be described by the product of a spatial and temporal function. The spatial function defines the geometry of the absorber and if the absorbing layer is optically thin, then the absorption profile is assumed to be uniform and the spatial heating function is a constant [17, 23, 78]. But for optically thick absorbers, the absorption profile is assumed to follow Beer's Law of absorption, and thus the function exponentially decays as light propagates through the layer [12–15, 21, 22].

The temporal function is used to describe the input light pulse. Short-light pulses can be approximated as a delta function and when used in the analytical derivation, the response to other input waveforms can be derived by convolution [14, 16, 18].

Reconstruction of the spatial or temporal heating function from the generated acoustic pulse depends on the relative length scales of the structure. The key length scales are given in Table 2.2. The acoustic relaxation time is a material property of the absorbing layer and is defined as:

$$\tau_{aco} = \min\left(\frac{1}{\alpha c}, \frac{d}{c}\right), \tag{2.2}$$

where α, c, and d, are the optical absorption coefficient, speed of sound, and thickness of the absorbing layer. When $\alpha d << 1$, the absorbing layer is considered optically thin, and the acoustic relaxation time is given by,

$$\tau_{aco} = \frac{d}{c}, \tag{2.3}$$

whereas, an optically thick absorber ($\alpha d >> 1$) has an acoustic relaxation time that is proportional to the optical penetration depth.

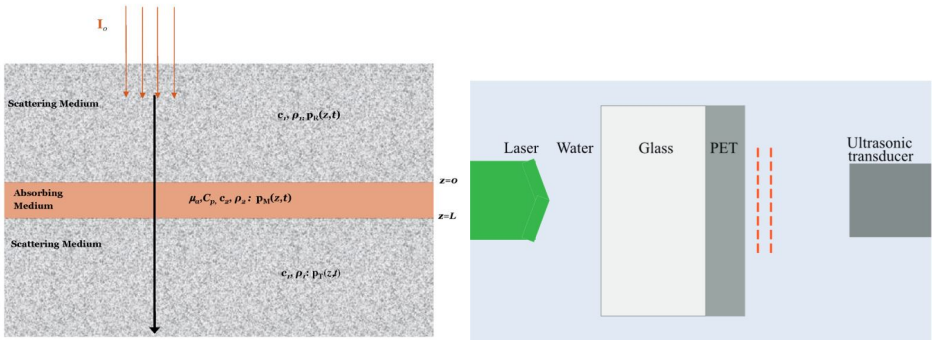
Key parameters	
τ_{aco}	acoustic relaxation time
τ_p	input light pulse width
T_p	generated acoustic pulse width
$\frac{1}{\alpha c}$	optical penetration time
$\frac{d}{c}$	sonic transit time

Table 2.2: Key length scales in photoacoustic generation, where α, c, and d, are the optical absorption coefficient [m^{-1}], speed of sound [ms^{-1}], and thickness [m] of the absorbing layer.

The input light pulse, τ_p, is defined as long or short, relative to the acoustic relaxation time. When the light pulse is short ($\tau_p << \tau_{aco}$), the spatial heating function and thus, the optical absorption profile of the structure, can be recreated from the generated acoustic pulse. Conversely, longer light pulses ($\tau_p >> \tau_{aco}$) generate acoustic signals that have the same width and shape as the light pulse itself. In work by

Cywiak et al. [16], the effect of the optical absorption coefficient and the input light pulse width on the generated acoustic signal was investigated and the authors' results confirmed the well-known short and long pulse regime. However, contrary to previous work, Cywiak et al. also defined a sub-region in the short-pulse regime to distingush between the two potential definitions of the acoustic relaxation time (Eq. 2.2).

Cywiak et al's analytical model did not take into account the acoustic impedance mismatch. If the absorbing layer does not have the same acoustic impedance, Z, as the surrounding media, then the generated acoustic signal will be reflected at the interface. Reflections are crucial in many applications (e.g. pulse-echo detection) and the analytical models formulated in Refs. [12–15] all include acoustic impedance mismatch between the absorbing layer and the surrounding media. In work by Baddour and Mandelis [12], the structure is symmetric, such that the substrates to either side of the absorber have the same acoustic impedance (Fig. 2.5a). However, analytical models by Shan et al [14], Svanstrom et al [13], and Rajagopal and Cox [15] all take into account structures with asymmetric acoustic impedances, such that the acoustic source and surrounding substrates do not have the same acoustic impedance (Fig. 2.5b).



(a) (b)

Figure 2.5: Asymmetry in acoustic impedance: in the analytical model derived by Baddour and Mandelis [12] the substrates had the same acoustic impedance, and thus the three-layer structure (with single acoustic source) was symmetric. However, in Svanstrom et al [13], asymmetry in the acoustic impedance of the substrates was considered.

2.3.3 Numerical models

When a photoacoustic structure contains more than one absorbing layer, an analytical solution to the governing equation becomes too computationally cumbersome. Instead, transfer-matrix methods can be used. Bozoki et al [79] derived a transfer matrix for the thermoelastic response of an N-layered structure irradiated by modulated laser light. Hu et al [24,25] used a transfer-matrix method to solve the coupled thermoelastic equations for a structure in which any layer could be absorbing, but the absorption profile was only treated as exponential, and thus, weakly-absorbing layers or a structure which induced the interference of light, could not be modelled. Heat conduction was neglected in the formulation by Sun et al [23,80] and resulted in a much simpler transfer-matrix, describing the response of structure with alternating absorbing and transparent layers to pulsed or modulated light. The authors limited their formulation to optically thin absorbers only, and thus the pressure generated by each source was always uniform. With constant sonic transit time in every layer, the authors were able to demonstrate interference effects (the superposition of reflected and transmitted acoustic waves) and the simulated results were validated by experimentation.

The k-wave toolbox, formulated by Treeby and Cox [81], is more complex and uses the finite-difference method in the time domain, but pseudo-spectral methods in the spatial domain, to solve the governing photoacoustic equation numerically. Unlike in finite-difference analysis, where a high-order polynomial is fit to each grid point to calculate the gradient of the field, a Fourier series is used and then a perfectly-matched layer is implemented as a boundary condition. This methodology reduces the number of grid points needed and thus, improves the speed and efficiency of the model.

2.4 Measuring sound

Most photoacoustic applications require high-amplitude and high-frequency acoustic signals and thus, the peak pressure and bandwidth (-3dB or -6dB) have been used to characterise the performance of the photoacoustic composites in Table 2.1. However, detecting the generated acoustic signal requires a transducer and thus, it is a voltage, not a pressure signal, that is measured.

2.4.1 Pressure-to-voltage conversion

In experimental set-ups, the generated acoustic signal is detected using a transducer. Home-made transducers, made from a polyvinylidene fluoride (PVDF) film, tens of microns in thickness, and fed to a pre-amplifier, are commonly used [20, 23, 44, 50, 76] but commercially available microphones [51, 82] and hydrophones [6, 8, 26, 33, 45] are also widely used. Thus, the predicted acoustic signal derived from a model must be compared to a measured voltage from experiments. In Shan et al. [14] and Svanstrom et al. [13], the voltage output from a piezoelectric transducer, $v(t)$, in response to a pressure input, $p(t)$, was described using a second order differential equation:

$$\frac{d^2v(t)}{dt^2} + 2\zeta\omega_n\frac{dv(t)}{dt} + \omega_n^2 v(t) = \epsilon\frac{dp(t)}{dt}, \tag{2.4}$$

where ζ, ω_n, and ϵ are constants of the system and characterise the mechanical and piezoelectric behaviour of the transducer. The constants for a fabricated transducer were difficult to determine individually and the authors used system identification methods, i.e., comparing experimental and predicted results, to calculate them. Then, a discrete-time version of the differential equation (Eq. 2.4) was transformed into the z-domain, such that:

$$V(z) = K_0(1 - z^{-1})P(z) + (K_1 z^{-1} + K_2 z^{-2})V(z) \tag{2.5}$$

where:

$$K_0 = \frac{\epsilon\tau}{1 + 2\zeta\omega_n\tau + \omega_n^2\tau^2} \tag{2.6}$$

$$K_1 = \frac{2(1 + \zeta\omega_n\tau)}{1 + 2\zeta\omega_n\tau + \omega_n^2\tau^2} \tag{2.7}$$

$$K_2 = -\frac{1}{1 + 2\zeta\omega_n\tau + \omega_n^2\tau^2} \tag{2.8}$$

and τ is the sampling period, K_0 has units of V/Pa, and K_1 and K_2 are dimensionless. Thus, the transducer could be expressed in a block diagram, shown in Fig. 2.6.

A pressure-to-voltage transfer function was also derived by Gutierrez-Reyes et al [22]. The authors modelled the piezoelectric transducer as two metallic blocks surrounding a piezoelectric film and solved Gauss' equation for the electric field between the two metallic layers (Gaussian surfaces). In this way, the pressure signal derived from a photoacoustic model was compared to experimental results presented on an oscilloscope.

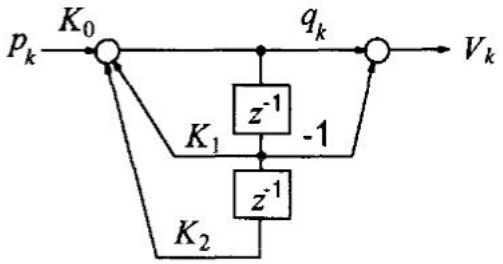


Figure 2.6: Figure from [14]: the block diagram of the piezoelectric transducer, where a pressure input, p_k, is converted into an output voltage, V_k, and the subscript k refers to the current sampling instant.

2.4.2 Acoustic energy and the photoacoustic conversion efficiency

In most applications, high amplitude photoacoustic signals are required and the simplest way to achieve this is by increasing the laser fluence of the input light source. However, when the laser fluence is too high, material ablation occurs. For example, carbon nanotubes composites have a material damage threshold of 300 mJ cm^{-2} [46]. Thus, photoacoustic composites must convert input light energy to acoustic energy as efficiently as possible and the photoacoustic conversion efficiency of a material can be calculated as [5, 31–33, 45, 48, 50]:

$$\eta = \frac{E_{aco}}{E_{opt}}, \tag{2.9}$$

where E_{aco} and E_{opt} are the output acoustic energy and input light energy, respectively. The acoustic energy can be expressed as:

$$E_{aco} = \frac{A_s}{\rho c} \int_{-\infty}^{\infty} p(t)^2 dt, \tag{2.10}$$

where A_s is the area of the laser facula, ρ and c are the material density and speed of sound, respectively, and $p(t)$ is the pressure so that the integral represents the time-averaged acoustic intensity.

The input optical energy is the product of the light fluence, Q_0, and the area of the laser facula, i.e.,

$$E_{opt} = A_s Q_0, \tag{2.11}$$

and so the expression for the conversion efficiency (Eq. 2.9) becomes:

$$\eta = \frac{1}{Q_0 Z} \int_{-\infty}^{\infty} p(t)^2 dt, \tag{2.12}$$

where $Z(=\rho c)$ is the acoustic impedance of the material. In Lee et al [50], the normalised conversion efficiency, η/Q_0, was used to compare the photoacoustic efficiencies of other composites under different laser conditions.

2.5 Summary

The photoacoustic effect provides an excellent solution to many of the problems arising in cross-media applications as it combines the favourable attributes of light with those of sound. Hence, the photoacoustic structures themselves must have both good optical absorption properties and a strong thermal expansion response in order to improve the conversion efficiency from light to sound. Composites are used to achieve this and recent advancements in nanofabrication have led to the use of thin-film optical absorbers sandwiched between layers of optically-transparent but thermally-responsive media. These multilayered structures can be modelled using the transfer-matrix method to solve the governing photoacoustic equation. However, the two previous attempts to do this have limited the absorbing layers to only weakly-absorbing (optically thin) [23] or to absorbing layers that only have an exponentially-decaying absorption profile (optically-thick) [24,25]. The differences in the acoustic signals generated by these two assumptions have not been investigated, nor has an attempt been made to show how the interference of light may be included in the transfer-matrix formulation, or how significant its effect may be.

The aim of this research was to explore how both optical and acoustical subwavelength layers could be used to enhance the photoacoustic signal generated by thin-film, multilayered composite. As defined in Ch. 1, the objectives of the research were (1) to formulate a one-dimensional model capable of simulating the photoacoustic signal generated by a multilayered structure in which the optical absorption profile of the layers was not limited, (2) to investigate the resonant behaviour of such structures, and (3) to use the formulated model to design a photoacoustic composite with subwavelength features which enhanced the emission efficiency of the generated acoustic signal. In the following chapter, the first objective has been addressed and the methodology used to formulate the photoacoustic model designed in this work has been explained.

Chapter 3

The photoacoustic model

In Chapter 2, a significant limitation of photoacoustic conversion was discussed. Materials with strong optical absorption properties, like metals, have poor thermal expansion coefficients. Conversely, materials that have favourable thermal expansion coefficients, like common polymers, are optically transparent. A simple solution to this is to use composites and many exciting designs have been made possible by advances in nanofabrication. Of these, the simplest is the thin-film stack with an optical absorber sandwiched between two polymer substrates [50]. However, the structure used by Lee et al [50] had only one optical absorber. In many applications, both optical [34–36] and acoustic [23, 40, 41, 83], it has been demonstrated that structures comprised of thin film multilayers have enhanced performance characteristics. Driven by the curiosity to realise the same performance enhancements in photoacoustic applications, a model capable of simulating multilayered structures with distributed heat sources has been designed in this work.

In **Section 3.1**, previous attempts to model photoacoustic sources have been examined and their limitations and assumptions have been discussed. In **Section 3.2**, the transfer matrix model designed in this work has been introduced. **Section 3.2.1** describes how the coefficients and thus, the acoustic signal, in every layer of a multilayered structure can be derived. In **Section 3.3** the acoustic energy has been derived and the acoustic counterpart to the Poynting vector has been defined. In **Section 3.4**, the heating function and its effect on the generated acoustic signal is explored and finally, in **Section 3.5**, the numerical inverse Fourier transform is used to produce the temporal pressure profile.

3.1 Previous work

The generation of photoacoustic waves is governed by the following equation [18]

$$\Big[\nabla^2 - \frac{1}{c^2}\frac{\partial^2}{\partial t^2}\Big]p(\mathbf{r},t) = -\frac{\beta}{C_p}\frac{\partial H(\mathbf{r},t)}{\partial t} \tag{2.1}$$

where c, β, and C_p are the speed of sound [ms^{-1}], the thermal expansion coefficient [K^{-1}], and the specific heat at constant pressure [J kg^{-1} K^{-1}] of the irradiated material, respectively. The input optical energy density per unit time is represented by H [J m^{-3} s^{-1}]. It has been assumed that $H(\mathbf{r},t)$ can be separated into a function of space, which describes the optical absorption profile, and a temporal function, which describes the input optical pulse [12,14,15,18,21,22]. Thus, the resulting acoustic signal broadly depends on the characteristics of the input light source and the material properties of the irradiated material.

A solution for Eq. 2.1 has been outlined by several authors. In all these studies, a one-dimensional model was used assuming that the optical penetration depth was much smaller than the laser spot size. Therefore, the generated sound wave is planar [16, 24, 25]. This means that transverse waves (e.g. shear and elastic) can be neglected and materials can be treated as fluids [15, 22]. When heat transport was considered [24, 25], the formulation was significantly more cumbersome as the thermoelastic equations could not be decoupled. A later study [19] showed that heat transport had little effect on the output signal; the photothermal component of the generated signal was slower, arriving at the detector several milliseconds later and with a magnitude seven orders smaller than the photoacoustic component.

Further simplifications have been studied. For example, most studies only considered a single absorber [12–16, 19–22]. For example, in Cywiak et al's work [16], an analytical solution to Eq. 2.1 was derived using Green's function for a single-absorber structure with no mechanical barriers. Without reflections, the effect of optical absorption and laser pulse duration on the output signal was more easily observed. The shape of the input laser pulse must also be defined: a delta function was used in Refs. [13, 14, 20, 21, 23, 80], a rectangular function was used in Refs. [15, 19, 22], a Gaussian function was used in Ref. [16, 84], and a train of delta functions was used in Refs. [12, 23].

If more than one absorbing layer is considered, an analytical solution becomes computationally cumbersome and numerical methods, such as the transfer-matrix method, are preferred. Work by Sun et al. [23] used a transfer-matrix to simulate the

generated signal from a photoacoustic multilayered structure, comprised of alternating optically-absorbing and transparent layers. The authors assumed that the optical thickness of the absorbing layers was very thin ($\alpha d << 1$), such that the spatial heating function was uniform. In work by Hu et al. [24, 25], a transfer-matrix model was also used but this time the absorbing layers were assumed to be optically thick ($\alpha d >> 1$) and the spatial heating function was always exponential. As discussed previously, Hu et al also included the effects of heat transport so that the unknown thermal conductivity and thermal contact resistance of a sample could be calculated from its generated photoacoustic signal. However, outside of gas spectroscopy, such calculations are not essential and neglecting heat transport would simplify the transfer-matrix considerably.

In this work, the transfer-matrix method has been used to simulate multilayered structures with distributed heat sources, where the optical thickness of the absorbing layers has not been constrained and thus, the signal generated by optically-thick or optically-thin absorbers can be compared.

3.2 The transfer-matrix model

In the following work, the transfer-matrix method is used to solve the governing photoacoustic wave equation for a N-layered structure, illustrated in Fig. 3.1. Any qth layer in the structure is a potential source of acoustic waves, depending on its optical absorption coefficient, α_q. The optical absorption coefficient in each layer can take any value and the absorption profile does not have to be constant across the layer (as was the case in Refs. [23, 78]). A local light fluence, Q_q, is defined so that a multilayered structure, irradiated by light from one side and attenuated as it propagates through each absorbing layer, can be modelled. Thus, the model is capable of simulating the acoustic signal generated from a complex structure comprised of multiple layers with acoustic impedance mismatches and irradiated from an incident direction, as may be envisaged in practise.

For propagation in one-dimension, the photoacoustic wave equation governing the pressure in any layer q of a structure, is given in the frequency domain as [12]:

$$\left[\frac{\partial^2}{\partial z^2} + \frac{\omega^2}{c_q^2}\right] p_q(z,\omega) = -\frac{\beta_q}{C_{p,q}} i\omega H(z,\omega), \tag{3.1}$$

where the qth layer has thickness d_q and is defined between z_{q-1} and z_q as illustrated in Fig. 3.1. The notation $e^{+i\omega t}$ has been used to describe the wave's time dependence and thus, $e^{-ik_q z}$ describes propagation in the positive z-direction, i.e., to the right.

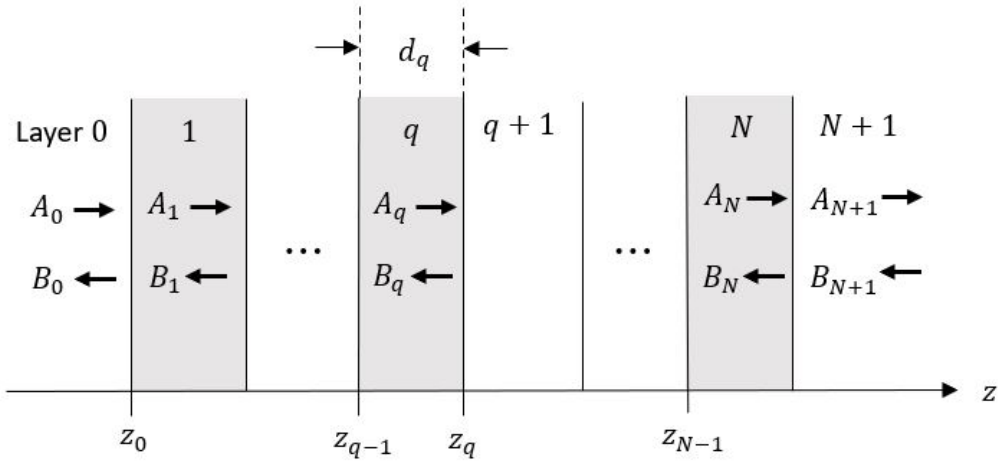


Figure 3.1: For a multi-layered structure with N layers, the photoacoustic signal in the qth layer is comprised of a right- and left-travelling component with corresponding coefficients A_q and B_q. If the two substrates, layers 0 and $N+1$, are semi-infinite and contain no sources and then A_0 and B_{N+1} must be zero.

The solution to Eq. 3.1 can be expressed as the sum of the general solution, which must have right- and left-travelling components, and the particular solution, which depends on the heating function, $H(z,\omega)$. Thus, the pressure, $p_q(z,\omega)$, in any layer q can be expressed as:

$$p_q(z,\omega) = A_q e^{-ik_q z} + B_q e^{+ik_q z} + p_{ps}(z,\omega), \tag{3.2}$$

where A_q and B_q are the coefficients of the right- and left- travelling waves and p_{ps} is the particular solution. The acoustic wavenumber is $k_q = \omega/c_q$ and z is the direction of propagation. The definition of p_{ps} plays a crucial role as it depends wholly on the definition of the heating function, $H(z,\omega)$.

Each of the terms on the right hand side of Eq. 3.2 will be discussed in further detail. The coefficients, A_q and B_q, have been derived using the transfer-matrix method in Section 3.2.1 and expressions for the particular solution, p_{ps}, the heating function, H, and the local light fluence, Q_q, have been found in Section 3.4.

3.2.1 Boundary conditions

To calculate the coefficients of the general solution, A_q and B_q, in Eq. 3.2, two boundary conditions are required. At any given boundary z_{q-1}, the pressure and acceleration of the particles must be continuous. Expressed in matrix form, these

boundary conditions are

$$\left.\begin{pmatrix} p_{q-1} \\ \frac{1}{\rho_{q-1}}\frac{\partial p_{q-1}}{\partial z} \end{pmatrix}\right|_{z_{q-1}} = \left.\begin{pmatrix} p_q \\ \frac{1}{\rho_q}\frac{\partial p_q}{\partial z} \end{pmatrix}\right|_{z_{q-1}} \tag{3.3}$$

where ρ_q is the density of the qth layer. Then, substituting Eq. 3.2 into Eq. 3.3 gives:

$$[M_{q-1}]|_{z_{q-1}} \begin{pmatrix} A_{q-1} \\ B_{q-1} \end{pmatrix} + (N_{q-1})|_{z_{q-1}} = [M_q]|_{z_{q-1}} \begin{pmatrix} A_q \\ B_q \end{pmatrix} + (N_q)|_{z_{q-1}},$$

where, M and N represent matrices and vectors, respectively, and have been defined below. The expression can be rearranged to make the coefficients, A_q and B_q, in the qth layer the subject of the equation,

$$\begin{pmatrix} A_q \\ B_q \end{pmatrix} = [M_q]^{-1}\big|_{z_{q-1}} [M_{q-1}]|_{z_{q-1}} \begin{pmatrix} A_{q-1} \\ B_{q-1} \end{pmatrix} + [M_q]^{-1}\big|_{z_{q-1}} (N_{q-1} - N_q)|_{z_{q-1}}, \tag{3.4}$$

where,

$$\begin{aligned}
[M_q]^{-1}\big|_{z_{q-1}} &= \frac{\rho_q}{2ik_q}\begin{bmatrix} \frac{+ik_q}{\rho_q}\exp\left(+ik_q z_{q-1}\right) & -\exp\left(+ik_q z_{q-1}\right) \\ \frac{+ik_q}{\rho_q}\exp\left(-ik_q z_{q-1}\right) & \exp\left(-ik_q z_{q-1}\right) \end{bmatrix}, \\
[M_{q-1}]|_{z_{q-1}} &= \begin{bmatrix} \exp\left(-ik_{q-1} z_{q-1}\right) & \exp\left(+ik_{q-1} z_{q-1}\right) \\ \frac{-ik_{q-1}}{\rho_{q-1}}\exp\left(-ik_{q-1} z_{q-1}\right) & \frac{+ik_{q-1}}{\rho_{q-1}}\exp\left(+ik_{q-1} z_{q-1}\right) \end{bmatrix}, \\
(N_{q-1})|_{z_{q-1}} &= \begin{pmatrix} p_{ps}(z_{q-1}, k_{q-1}) \\ \frac{1}{\rho_{q-1}}\frac{\partial p_{ps}(z_{q-1}, k_{q-1})}{\partial z} \end{pmatrix}, \\
(N_q)|_{z_{q-1}} &= \begin{pmatrix} p_{ps}(z_{q-1}, k_q) \\ \frac{1}{\rho_q}\frac{\partial p_{ps}(z_{q-1}, k_q)}{\partial z} \end{pmatrix}.
\end{aligned}$$

In other words, at the interface, z_{q-1} (in Fig. 3.2), there are two matrices and two source vectors that fully define the coefficients on one side of the interface, A_q and B_q, in terms of the coefficients on the other side of the interface, A_{q-1} and B_{q-1}.

Similarly, at the following interface at z_q (in Fig. 3.3), the coefficients, A_{q+1} and B_{q+1} can be expressed in terms of the coefficients, A_q and B_q, using two further matrices, $[M_q]|_{z_q}$ and $[M_{q+1}]|_{z_q}$, and two further source vectors, $(N_q)|_{z_q}$ and $(N_{q+1})|_{z_q}$, i.e.,

$$\begin{pmatrix} A_{q+1} \\ B_{q+1} \end{pmatrix} = [M_{q+1}]^{-1}\big|_{z_q} [M_q]|_{z_q} \begin{pmatrix} A_q \\ B_q \end{pmatrix} + [M_{q+1}]^{-1}\big|_{z_q} (N_q - N_{q+1})|_{z_q}. \tag{3.5}$$

An expression for the vector $\begin{pmatrix} A_q \\ B_q \end{pmatrix}$ has already been derived in Eq 3.4 so it is sub-

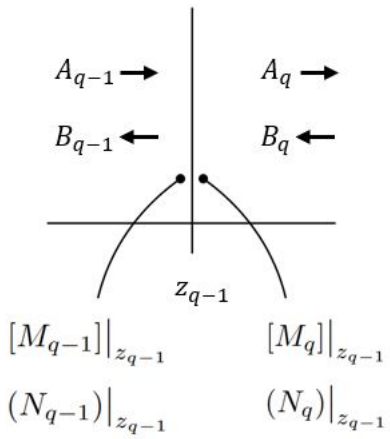


Figure 3.2: Defining the coefficients A_q and B_q

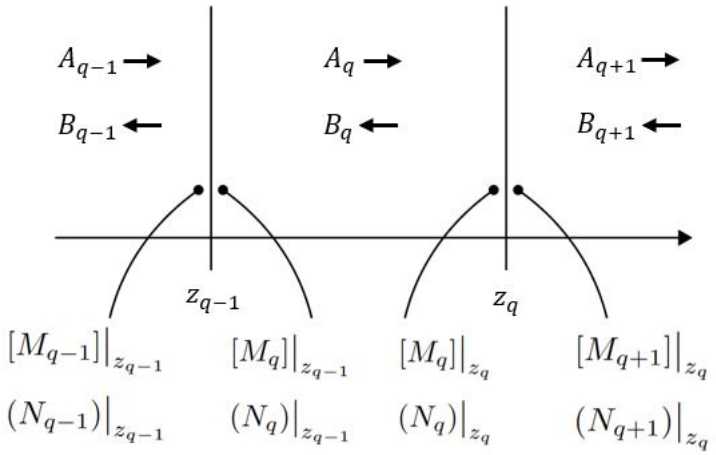


Figure 3.3: Defining the coefficients A_{q+1} and B_{q+1}

stituted into Eq 3.5:

$$\begin{pmatrix} A_{q+1} \\ B_{q+1} \end{pmatrix} = [M_{q+1}]^{-1}\big|_{z_q} [M_q]|_{z_q} \Big\{ [M_q]^{-1}\big|_{z_{q-1}} [M_{q-1}]|_{z_{q-1}} \begin{pmatrix} A_{q-1} \\ B_{q-1} \end{pmatrix} + [M_q]^{-1}\big|_{z_{q-1}} (N_{q-1} - N_q)|_{z_{q-1}} \Big\} + [M_{q+1}]^{-1}\big|_{z_q} (N_q - N_{q+1})|_{z_q} ,$$

which can be simplified to produce the following unwieldy expression,

$$\begin{pmatrix} A_{q+1} \\ B_{q+1} \end{pmatrix} = [M_{q+1}]^{-1}\big|_{z_q} [M_q]|_{z_q} [M_q]^{-1}\big|_{z_{q-1}} [M_{q-1}]|_{z_{q-1}} \begin{pmatrix} A_{q-1} \\ B_{q-1} \end{pmatrix} + [M_{q+1}]^{-1}\big|_{z_q} [M_q]|_{z_q} [M_q]^{-1}\big|_{z_{q-1}} (N_{q-1} - N_q)|_{z_{q-1}} + [M_{q+1}]^{-1}\big|_{z_q} (N_q - N_{q+1})|_{z_q} \quad (3.6)$$

To make sense of this expression, consider the first term on the right hand side of Eq. 3.6:

$$\underbrace{[M_{q+1}]^{-1}\big|_{z_q}}_{\text{second interface matrix}}\underbrace{[M_q]\big|_{z_q}\,[M_q]^{-1}\big|_{z_{q-1}}}_{\text{propagation matrix}}\underbrace{[M_{q-1}]\big|_{z_{q-1}}}_{\text{first interface matrix}}\begin{pmatrix}A_{q-1}\\B_{q-1}\end{pmatrix}$$

The product of the two central matrices, $[M_q]\big|_{z_q}\,[M_q]^{-1}\big|_{z_{q-1}}$, is the propagation matrix through the qth layer:

$$[M_q]\big|_{z_q}\,[M_q]^{-1}\big|_{z_{q-1}} = \begin{bmatrix}\cos\phi_q & \frac{\rho_q}{k_q}\sin\phi_q\\ -\frac{k_q}{\rho_q}\sin\phi_q & \cos\phi_q\end{bmatrix} \tag{3.7}$$

where, $\phi_q = k_q(z_q - z_{q-1})$. The two outer matrices can be considered as the transfer matrices across the first and second interfaces, $[M_{q-1}]\big|_{z_{q-1}}$ and $[M_{q+1}]^{-1}\big|_{z_q}$, respectively. Thus, the product of the four matrices gives the characteristic matrix of the qth layer, $[T_q]$.

The second and third terms on the right side of Eq. 3.6 represent the contribution from the photoacoustic sources within the structure. If there are no sources, these two terms disappear and Eq. 3.6 reduces to the familiar transfer-matrix equation:

$$\begin{pmatrix}A_{q+1}\\B_{q+1}\end{pmatrix} = [T_q]\begin{pmatrix}A_{q-1}\\B_{q-1}\end{pmatrix}$$

In this way, the coefficients in each layer of a multilayered structure (Fig. 3.1) can be expressed in terms of the coefficients in layer 0.

$$\begin{pmatrix}A_{N+1}\\B_{N+1}\end{pmatrix} = \prod_{q=1}^{N}[T_q]\begin{pmatrix}A_0\\B_0\end{pmatrix} \tag{3.8}$$

3.2.2 Reflection and transmission at a single interface

Consider a single interface shown in Fig. 3.4, where there are no photoacoustic sources in layer 0 or layer 1. The coefficients of the right- and left-travelling components in layer 1, A_1 and B_1, can be expressed in terms of those in layer 0, A_0 and B_0, by:

$$\begin{pmatrix}A_1\\B_1\end{pmatrix} = [M_1]^{-1}\big|_{z_0}\,[M_0]\big|_{z_0}\begin{pmatrix}A_0\\B_0\end{pmatrix}. \tag{3.9}$$

The characteristic matrix, $[T_1]$, is not used here because it is defined for a film, not an interface.

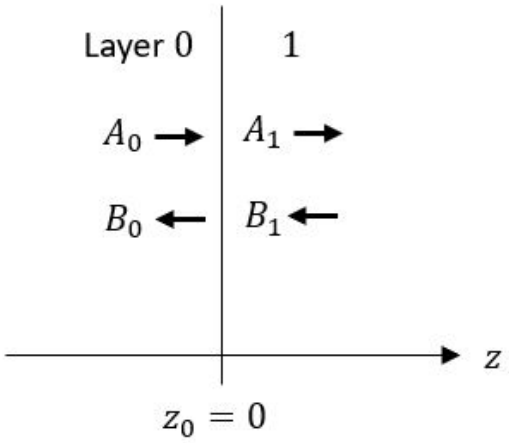


Figure 3.4: A single interface at $z = z_0$

If $z_0 = 0$, Eq. 3.9 becomes:

$$\begin{pmatrix} A_1 \\ B_1 \end{pmatrix} = \frac{\rho_1}{2ik_1} \begin{bmatrix} \frac{ik_1}{\rho_1} + \frac{ik_0}{\rho_0} & \frac{ik_1}{\rho_1} - \frac{ik_0}{\rho_0} \\ \frac{ik_1}{\rho_1} - \frac{ik_0}{\rho_0} & \frac{ik_1}{\rho_1} + \frac{ik_0}{\rho_0} \end{bmatrix} \begin{pmatrix} A_0 \\ B_0 \end{pmatrix}. \tag{3.10}$$

When an external acoustic source ($A_0 \neq 0$) irradiates the single interface from the left (rather than a photoacoustic source within the structure), there are no left-propagating acoustic waves in the semi-infinite layer 1, and so $B_1 = 0$. Therefore, from Eq. 3.10, the following expression can be found:

$$0 = \frac{\rho_1}{2ik_1}\Big(\frac{ik_1}{\rho_1} - \frac{ik_0}{\rho_0}\Big)A_0 + \frac{\rho_1}{2ik_1}\Big(\frac{ik_1}{\rho_1} + \frac{ik_0}{\rho_0}\Big)B_0, \tag{3.11}$$

and thus, for an acoustic wave travelling from medium 0 to medium 1, the reflection coefficient, r_{01}, can be written as:

$$\begin{aligned} r_{01} = \frac{B_0}{A_0} &= -\frac{\left(\frac{ik_1}{\rho_1} - \frac{ik_0}{\rho_0}\right)}{\left(\frac{ik_1}{\rho_1} + \frac{ik_0}{\rho_0}\right)} \\ &= -\frac{\Big(c_0\rho_0 - c_1\rho_1\Big)}{\Big(c_0\rho_0 + c_1\rho_1\Big)}, \end{aligned} \tag{3.12}$$

where the acoustic impedance of a layer, $Z_q = \rho_q c_q$ [85] and so:

$$r_{01} = -\frac{\Big(Z_0 - Z_1\Big)}{\Big(Z_0 + Z_1\Big)}. \tag{3.13}$$

The corresponding transmission coefficient, t_{01}, at the interface between layer 0 to 1 can also be derived from Eq. 3.10. The expression for A_1 is given by:

$$A_1 = \frac{\rho_1}{2ik_1}\Big(\frac{ik_1}{\rho_1} + \frac{ik_0}{\rho_0}\Big)A_0 + \frac{\rho_1}{2ik_1}\Big(\frac{ik_1}{\rho_1} - \frac{ik_0}{\rho_0}\Big)B_0. \tag{3.14}$$

B_0 can be expressed in terms of A_0 by rearranging Eq. 3.11 and then substituting it into Eq. 3.14 to obtain:

$$\begin{aligned} A_1 &= \frac{\rho_1}{2ik_1}\frac{1}{\left(\frac{ik_1}{\rho_1} + \frac{ik_0}{\rho_0}\right)}\left[\left(\frac{ik_1}{\rho_1} + \frac{ik_0}{\rho_0}\right)^2 - \left(\frac{ik_1}{\rho_1} - \frac{ik_0}{\rho_0}\right)^2\right]A_0 \\ &= \frac{Z_1}{2}\Big(\frac{Z_1Z_0}{Z_0+Z_1}\Big)\left[\frac{(Z_0+Z_1)^2}{Z_0^2Z_1^2} - \frac{(Z_0-Z_1)^2}{Z_0^2Z_1^2}\right]A_0, \end{aligned} \tag{3.15}$$

which, after some manipulation, gives the transmission coefficient for the interface as:

$$t_{01} = \frac{A_1}{A_0} = \frac{2Z_1}{Z_0+Z_1} \tag{3.16}$$

If layer 0 is copper and layer 1 is water then, using the material properties given in Table 3.1, Eqs. 3.13 and 3.16 can be used to calculate the reflection and transmission coefficients at the copper-water interface:

$$r_{Cu-w} = \frac{Z_w - Z_{Cu}}{Z_w + Z_{Cu}} = -0.93 \tag{3.17}$$

$$t_{Cu-w} = \frac{2Z_w}{Z_w + Z_{Cu}} = +0.07 \tag{3.18}$$

In Fig. 3.5, the model has been used to simulate an acoustic pulse as it travels towards the interface (top panel) and after collision with the interface (bottom). In the top panel, the incoming acoustic wave, with amplitude p_0, is in layer 0, travelling toward the interface at $z_0 = 0$. The bottom panel shows the acoustic wave some time t_1 later, after reflection from the interface. The reflected component moves back toward the left, in layer 0, with amplitude $-0.93p_0$ and the transmitted component moves to the right in layer 1 with amplitude $+0.07p_0$.

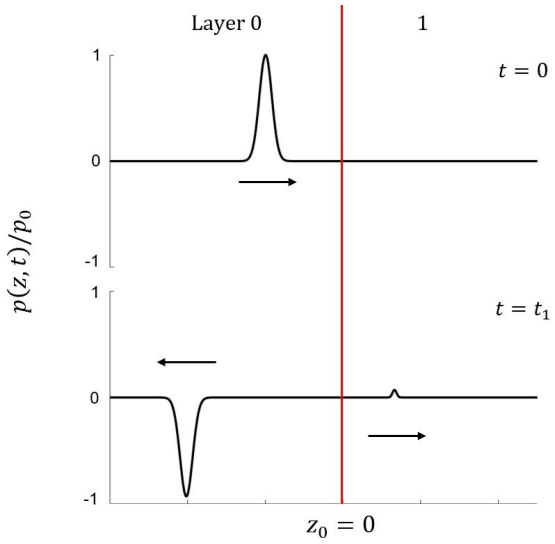


Figure 3.5: Reflections at the copper-water interface: before collision (top panel) the (Gaussian) acoustic pulse propagates to right in layer 0, with amplitude p_0. After collision (bottom panel), the acoustic signal has a reflected component, with amplitude, $-0.93p_0$, and a transmitted component with amplitude $+0.07p_0$, which propagates to the right in layer 1.

Layer No.	Material	Z $\times 10^6$ [kg m^{-2} s^{-1}]
0	Copper	40.7
1	Water	1.5

Table 3.1: Layer materials and acoustic impedance, Z, for the interface in Fig. 3.5

Note that with no acoustic attenuation, $1-r_{Cu-W} = t_{Cu-W}$. Acoustic attenuation could be included in the model by replacing the wavenumber for each layer, k_q, with a complex wavenumber:

$$k_q \rightarrow k'_q + ik''_q, \tag{3.19}$$

where $k'_q = 2\pi f/c_q$ is the real part, and k''_q is the imaginary part and represents acoustic attenuation [83]. However, in this work, the acoustic attenuation (not to be confused with optical absorption) has been assumed to be much smaller than k'_q and so k_q will always be real.

Using the transfer-matrix method, the reflection and transmission coefficients at an interface have been derived and an example has been given to demonstrate the behaviour of the acoustic wave at the interface. The expressions for the reflection and transmission coefficients (Eqns. 3.13 and 3.16) reveal the analogy between the acoustic and their optical equivalents, which can be derived using Fresnel equations. The refractive index of the qth layer is equivalent to the inverse of the acoustic

impedance Z_q, i.e.

$$n_q \to 1/Z_q. \tag{3.20}$$

3.3 Acoustic energy

The acoustic analogy with optics has been drawn for the reflection and transmission coefficients at normal incidence. In the following section, it has been extended to the acoustic energy by deriving the acoustic counterpart to Poynting's theorem, using the three linear acoustic equations: mass conservation, momentum conservation (Euler's linearised equation of motion for a fluid), and a relation derived from the second law of thermodynamics [85, p. 39]. These are, respectively,

$$\frac{\partial \rho'}{\partial t} + \rho_0 \nabla \cdot \boldsymbol{\nu} = 0, \tag{3.21}$$

$$\rho_0 \frac{\partial \boldsymbol{\nu}}{\partial t} = -\nabla p, \tag{3.22}$$

$$p = c^2 \rho', \quad c^2 = \left(\frac{\partial p}{\partial \rho}\right)_0, \tag{3.23}$$

where, following convention, ρ_0 is density of the ambient state and ρ' is a small perturbation of density, $\boldsymbol{\nu}$ is the local particle velocity, and c is speed of sound. The pressure, p, for a plane-travelling wave is given by [85]:

$$p = \mathrm{Re}\{\hat{p} e^{-i\omega t}\}, \tag{3.24}$$

where, $\hat{p} = |p| e^{+i\phi}$ is the complex pressure amplitude.

By taking the dot product of Eq. 3.22 with $\boldsymbol{\nu}$, then:

$$\begin{aligned} \boldsymbol{\nu} \cdot \left(\rho_0 \frac{\partial \boldsymbol{\nu}}{\partial t}\right) &= -\boldsymbol{\nu} \cdot \nabla p \\ &= -\nabla \cdot (\boldsymbol{\nu} p) + p \nabla \cdot \boldsymbol{\nu} \\ &= -\nabla \cdot (p \boldsymbol{\nu}) - \frac{p}{\rho_0} \frac{\partial \rho'}{\partial t} \end{aligned} \tag{3.25}$$

where the left hand side can be expressed as $\frac{\partial}{\partial t}\left(\frac{1}{2}\rho_0 \boldsymbol{\nu}^2\right)$ and using the thermodynamic relation (Eq. 3.23), the second term on the right hand side can be expressed as $\frac{1}{2}\frac{\partial}{\partial t}\left(\frac{p^2}{\rho_0 c^2}\right)$. Thus, Eq. 3.25 can be rewritten as:

$$\begin{aligned} \frac{\partial}{\partial t}\left(\frac{1}{2}\rho_0 \boldsymbol{\nu}^2\right) + \frac{1}{2}\frac{\partial}{\partial t}\left(\frac{p^2}{\rho_0 c^2}\right) + \nabla \cdot (p \boldsymbol{\nu}) &= 0 \\ \frac{\partial}{\partial t} w_a + \nabla \cdot \mathbf{S_{aco}} &= 0, \end{aligned} \tag{3.26}$$

where $w_a = \frac{1}{2}\rho_0 \boldsymbol{\nu}^2 + \frac{1}{2}\frac{p^2}{\rho_0 c^2}$ and $\mathbf{S_{aco}} = p\boldsymbol{\nu}$. Thus, the acoustic stored energy density is comprised of a kinetic and potential energy contribution and $\mathbf{S_{aco}} = p\boldsymbol{\nu}$ is an acoustic energy flux or acoustic intensity.

The time-averaged intensity can be expressed as:

$$S_{aco}^{avg} = \mathrm{Re}\left\{\frac{1}{2}\hat{p}^*\hat{v}\right\}, \tag{3.27}$$

where, $\hat{p}^*$ is the complex conjugate of the complex pressure amplitude. For plane waves travelling in one-dimension (i.e., $p = p(z,t)$), the local particle velocity becomes:

$$\boldsymbol{\nu} = \left(\frac{p}{\rho_0 c}\right)\mathbf{n}, \tag{3.28}$$

where $\mathbf{n}$ is a unit vector in the direction of propagation, z. Therefore, the complex velocity amplitude, $\hat{\nu}$, can be expressed in terms of the complex pressure amplitude, $\hat{p}$:

$$\hat{v} = \frac{|p|e^{+i\phi}}{\rho_0 c} \tag{3.29}$$

and so the time-averaged acoustic intensity (Eq. 3.27) reduces to:

$$S_{aco}^{avg} = \mathrm{Re}\left\{\frac{1}{2}\frac{|p|^2}{\rho_0 c}\right\} \tag{3.30}$$

The acoustic reflectance and transmittance can be defined as the ratio of the reflected and incident power and the transmitted and incident power, i.e.,

$$R = \frac{S_{aco}^r}{S_{aco}^i} = \frac{|p^r|^2}{|p^i|^2} \tag{3.31}$$

$$T = \frac{S_{aco}^t}{S_{aco}^i} = \frac{Z_i}{Z_t}\frac{|p^t|2}{|p^i|^2} \tag{3.32}$$

respectively, where $|p^r|$, $|p^i|$, and $|p^t|$ are the amplitudes of the reflected, incident, and transmitted components, respectively, and Z_i and Z_t are the acoustic impedances in the incident and emergent media. For the single interface in Fig. 3.4, R_{01} and T_{01} can be derived using Eq. 3.30:

$$R_{01} = \frac{S_{aco}^r}{S_{aco}^i} = \frac{|B_0|^2}{|A_0|^2} \tag{3.33}$$

$$T_{01} = \frac{S_{aco}^t}{S_{aco}^i} = \frac{Z_0}{Z_1}\frac{|A_1|^2}{|A_0|^2} \tag{3.34}$$

and hence, $R_{01} = |r_{01}|^2$ and $T_{01} = \frac{Z_0}{Z_1}|t_{01}|^2$.

3.4 The heating function

To demonstrate the reflection of acoustic waves at an interface, the single interface shown in Fig. 3.4 was irradiated by an external acoustic source rather than being generated by light absorption within the structure. To simulate an acoustic source stimulated by light, a heating function must be used [18]. As stated in Section 3.1, the heating function, $H(z,t)$, in Eq. 2.1 is commonly separated into a spatial function $h(z)$ and temporal function $I(t)$ [12, 14, 15, 18, 21, 22]:

$$H(z,t) = h(z)I(t) \tag{3.35}$$

This assumes that the absorbed optical energy is converted directly and instantaneously into heat energy; heat diffusion is assumed to be negligible during the excitation pulse [19]. Heat transport was considered in the model outlined in Ref. [24] but, in Ref. [19], the inclusion of heat transport resulted in a slow thermal response: the photothermal component of the signal arrived three orders of magnitude after the photoacoustic component, and with an amplitude several orders of magnitude smaller. In this work, heat conduction and thermal diffusion will be neglected as the length scales associated with the absorber and input pulse width are significantly smaller than those associated with heat transport.

3.4.1 The absorption profile and local light fluence

The spatial function, $h(z)$, depends on the optical absorption coefficient for the qth layer, α_q [m^{-1}], the light fluence incident on the layer, Q_{q-1} [Jm^{-2}], and the absorption profile of the layer, $A(z)$. For a single absorbing layer, the light fluence incident on the absorber is equal to the input light fluence, Q_0, and so the heating function is simply $h(z) = \alpha Q_0 A(z)$. For a structure with distributed heat sources (Fig. 3.6), light is attenuated as it passes through the structure and so the generalised heating function of the qth layer can be expressed as:

$$h(z) = \alpha_q Q_{q-1} A(z), \tag{3.36}$$

where the function, $A(z)$, describes the absorption profile of the layer and Q_{q-1} is the local light fluence irradiating the qth layer. The local light fluence, Q_{q-1}, is the light energy remaining after any absorption from previous layers and hence, using the notation shown in Fig. 3.6, it can be defined in terms of the absorption profile in the previous layer:

$$Q_{q-1} = Q_{q-2} A(z_{q-1} - z_{q-2}) \tag{3.37}$$

and thus the light transmitted out of the qth layer is:

$$Q_q = Q_{q-1} A(z_q - z_{q-1}) \tag{3.38}$$

When Beer's Law is used to describe optical absorption [12,14,15,21,22], the optical

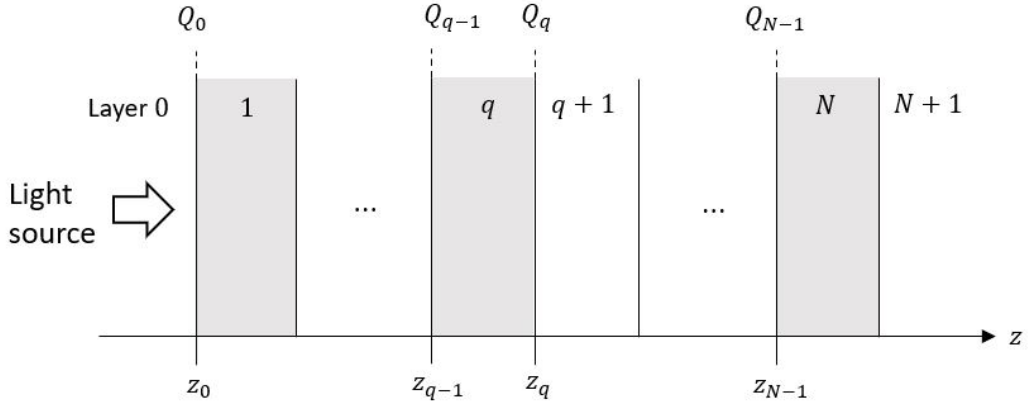


Figure 3.6: The local light fluence Q_q is spatially dependent in a structure with more than one absorber, irradiated by light from the left.

absorption profile becomes: $A(z) = \exp(-\alpha z)$ and hence, the particular solution, p_{ps}, of the governing photoacoustic equation must take the same form. After substituting a trial solution into Eq. 3.2, the following expression is derived

$$p_{ps}(z, k_q) = -i \frac{\kappa_q}{c_q} \frac{k_q}{\alpha_q^2 + k_q^2} e^{-\alpha_q z} \tag{3.39}$$

where, $\kappa_q = \frac{c_q^2 \beta_q}{C_p} \alpha_q Q_q I(\omega)$, $k_q = \omega / c_q$, and $I(\omega)$ is the Fourier transform of the temporal function, $I(t)$, in Eq. 3.35, which is used to describe the input light source and will be discussed later.

Thus, the formulation described in this work is capable of modelling the photoacoustic signal generated from a structure with more than one absorber, such that the light fluence decays through the structure in the direction of propagation, according to absorption profile in the previous layers.

For example, consider the structure shown in Fig. 3.7a with five absorbers (shaded, odd-numbered layers), each separated by a transparent layer (even-numbered layers). Every absorber has the same absorption coefficient, α, and thickness, d, and an absorption profile that follows Beer's Law. Thus, when light, with fluence Q_0, irradiates the structure from the left hand side, it is attenuated as it passes through each absorber. The normalised heating function, $\hat{h}(z) = h(z)/(\alpha Q_0)$ is shown in Fig. 3.7b and 3.7c when the absorbing layers are optically thin ($\alpha d << 1$) and optically thick

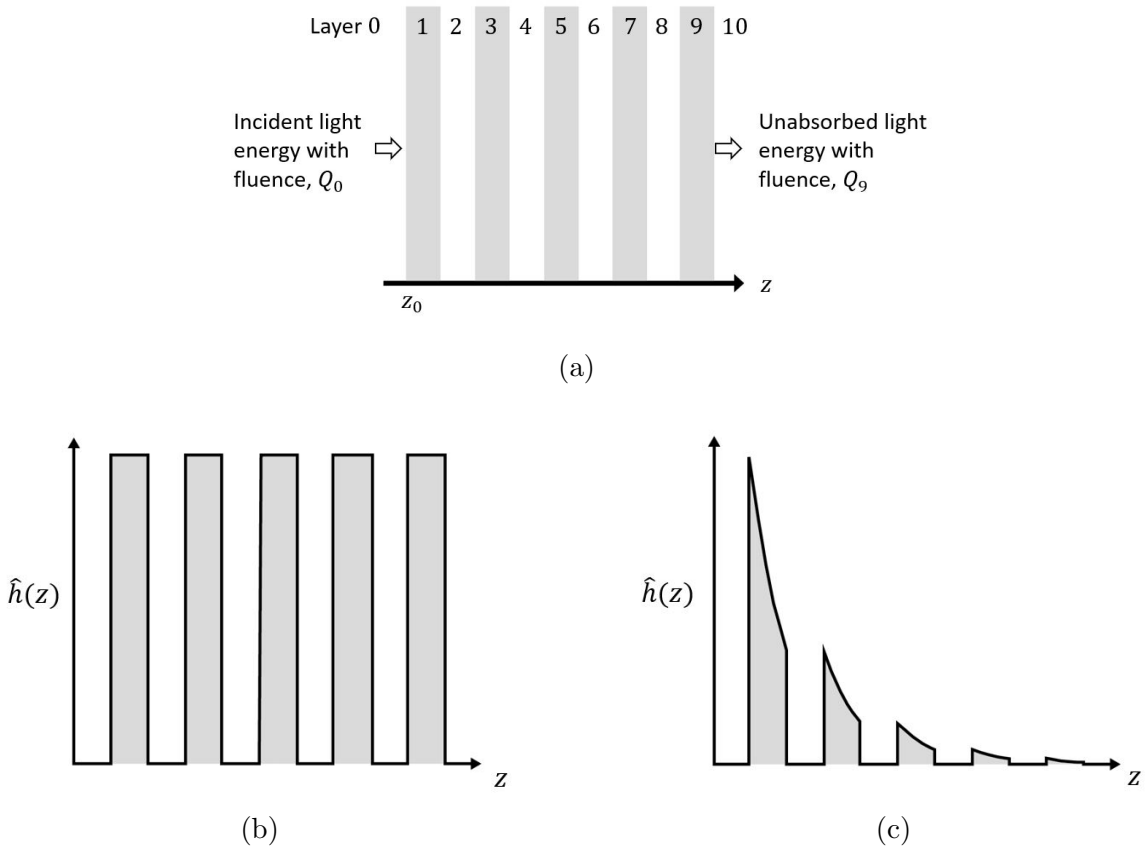


Figure 3.7: When a structure with more than one absorber is irradiated by light from the left, the light is attenuated as it travels through the structure. The amount of attenuation depends on the optical thickness, αd, of the layers. In (a) a structure with five alternating layers of absorbing (shaded) and non-absorbing layers, is irradiated by light with fluence, Q_0, from the left. The absorbing layers all have an optical absorption coefficient of α and all the layers have the same acoustic impedance, Z. In (b) the absorbing layers are optically thin ($\alpha d << 1$) and so the normalised heating function, $\hat{h}(z) = h(z)/(\alpha Q_0)$ is constant across the absorbers. In (c) the absorbers are optically thick ($\alpha d = 1$) and the optical absorption is assumed to follow Beer's Law, so the heating function is given by $h(z) = \alpha_q Q_q e^{-\alpha z}$ (Eq. 3.36), where Q_q is the local light fluence (Eq. 3.37).

($(\alpha d \geq 1)$, respectively. The optically thin structure produces a uniform heating function ($e^{-\alpha d} \rightarrow 1$ when $\alpha d << 1$). In contrast, the optically thick structure generates a heating function that decays exponentially according to Beer's Law. As a result, the local light fluence and optical absorption in layer 9 has been attenuated compared to that of the layer 1, closest to the light source.

In Sun et al [23], the authors formulated a model for structures with distributed heat sources but assumed that the absorbers were always optically thin. The struc-

tures always had uniform heating functions, like the one shown in Fig. 3.7b. Using the model formulated in this work, the effect of optically thin compared to optically thick absorbers on the generated acoustic signal will be explored in Chapter 5.

3.4.2 The input light function

The particular solution given in Eq. 3.39 was also proportional to $I(\omega)$ ($\kappa_q \propto I(\omega)$). The input light function, $I(\omega)$, is usually represented as an delta function in the time domain: $I(t) = \delta(t)$ and thus, in the frequency domain, $I(\omega) = 1$. A light source with a normalised temporal Gaussian profile can also be used,

$$I(t) = \frac{2}{t_p\sqrt{\pi}} \exp\left(- \left(2t/t_p\right)^2 \right) \tag{3.40}$$

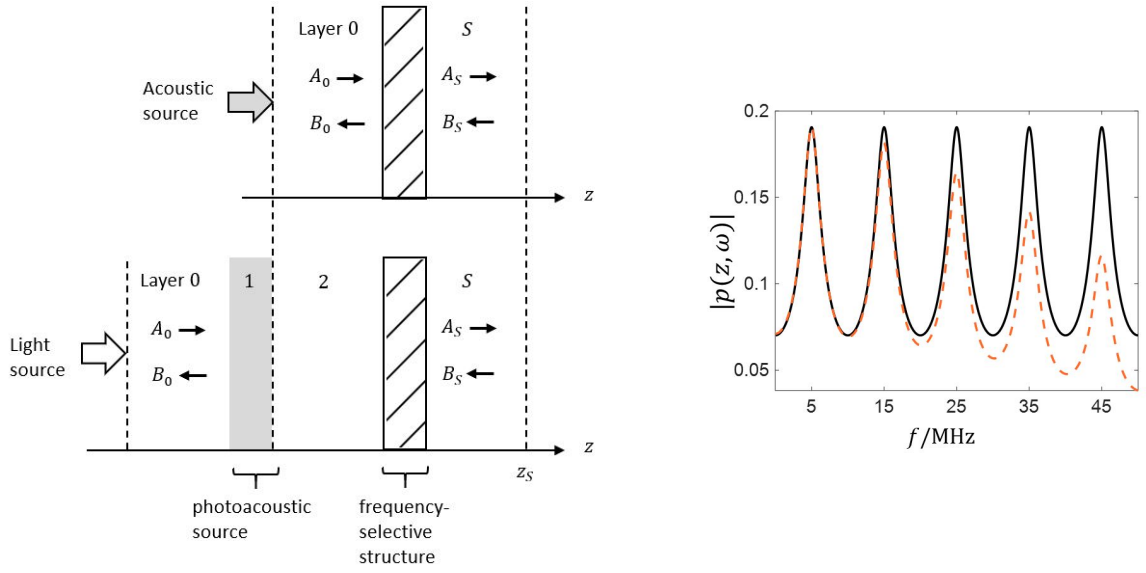
where t_p is the $1/e$-width in seconds and $\int I(t)\, dt = 1$. The Fourier transform of the Gaussian is

$$I(\omega) = \exp\left(- \omega^2 t_p^2/16 \right) \tag{3.41}$$

The effect of the shape and width of the input light function, $I(\omega)$, on the generated acoustic signal will be investigated in Chapter 4.

As stated at the start of Section 3.4, the single interface used in Section 3.2 had no photoacoustic source and the heating function, $h_q(z)$, in each layer was zero. Therefore, in the derivation of the reflection coefficient, r_{01}, the source vector, N_0 (from Eq. 3.4), was neglected. An external acoustic source irradiated the structure (top panel in Fig. 3.8a) and was implemented by making the right-travelling coefficient in the semi-infinite substrate on the left non-zero, i.e., $A_0 \neq 0$. This is in contrast to a photoacoustic structure (bottom panel in Fig. 3.8a), where the acoustic signal is generated in layer 1 when irradiated by light and layer 0 is semi-infinite substrate with no right-travelling components ($A_0 = 0$).

An external acoustic source ($A_0 \neq 0$) will be used again in Chapter 6 where the performance of frequency-selective structures, like quarter-wave plates, can be demonstrated more effectively by using incoming acoustic signals that have a constant amplitude over the selected frequency range. For example, both of the structures shown in Fig. 3.8a have a frequency-selective acoustic component (shown with right hashes) that has been designed to have high transmittance at a target frequency of 5MHz. In the top panel, the frequency-selective component has been irradiated by an external acoustic source with constant amplitude (shaded arrow). The acoustic signal



(a) (b)

Figure 3.8: In (a) a frequency selective structure irradiated by a constant external acoustic source in the top panel, in the bottom panel the same frequency-selective component is irradiated by the photoacoustic signal generated when light is absorbed by layer 1 . In (b) the signal detected at $z = z_s$ is shown for the two structures. The black (solid) line is the signal produced by the external acoustic source and red (dashed) line is from the photoacoustic pulse. The target frequency of the frequency-selective component was 5MHz.

detected at $z = z_S$ has been shown in Fig. 3.8b as a solid black line. As expected, the pressure transmitted through the structure is at a maximum at 5MHz (and at odd multiples of 5MHz).

In the bottom panel of Fig. 3.8a, the structure has been irradiated by an external light source, with a Gaussian profile as given in Eq. 3.40 and 3.41. A photoacoustic pulse is generated in layer 1 (shaded region) and has the same shape as the input light pulse (as will be discussed in Chapter 4). Then, the photoacoustic pulse irradiates the frequency-selective component. The acoustic signal detected at $z = z_S$, shown as a dashed, orange line in Fig. 3.8b, is still periodic, with maximum amplitudes at 5MHz and at odd multiples of 5MHz due to the frequency-selective structure, but the influence of the input Gaussian pulse can also be seen because the photoacoustic signal decays with frequency, according to Eq. 3.41. Thus, by removing the effect of the photoacoustic pulse and instead using an external acoustic source, the behaviour resulting from the frequency-selective structure alone can be investigated. Such behaviour will be discussed in more detail in Chapter 6.

3.5 Resolution and the numeric inverse Fourier transform

In Section 3.2, the coefficients needed to express the acoustic signal in every layer as a function of frequency, $p_q(z,\omega)$, were calculated using the transfer-matrix method. The time-dependent pressure signal can be calculated by performing the inverse Fourier transform on the expression for $p_q(z,\omega)$ in Eq. 3.2, i.e.,

$$p_q(z,t) = \mathcal{F}^{-1}[p_q(z,\omega)] = \frac{1}{2\pi}\int_{-\infty}^{\infty} p_q(z,\omega)e^{+i\omega t}d\omega. \tag{3.42}$$

When calculated numerically in MATLAB, the transform takes the discrete form:

$$p_q(z,n) = \sum_{m=0}^{N-1} p_q(z,m)e^{+inm/N} \tag{3.43}$$

where in the frequency domain, the mth sample in a sequence of N samples transforms into the nth value in the time domain [86]. Thus, the temporal signal is fully determined by sampling at a series of points spaced at $1/(2F_{max})$, where F_{max} is the maximum frequency in the spectrum of $p_q(z,\omega)$ [87]. In other words, the time step δt must satisfy the following inequality: $\delta t \leq 1/(2F_{max})$, referred to as the Nyquist theorem. Hence, the duration of the temporal signal, T, and sampling rate, F_S must be carefully chosen to avoid aliasing.

Layer No.	Material	Z $\times 10^6$/ kg m^{-2} s^{-1}	d/mm	α/m^{-1}
0	Copper	40.7	-	0
1	Copper	40.7	1	1
2	Copper	40.7	1	0
3	QWP	7.8	0.25	0
S	Water	1.5	-	0

Table 3.2: Layer materials and properties of the structure shown in the bottom panel of Fig. 3.8a.

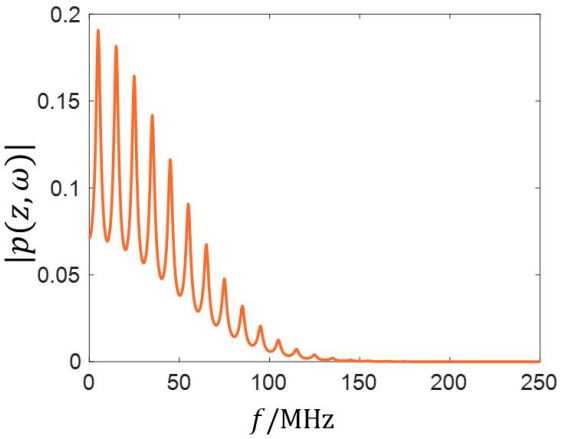


Figure 3.9: The acoustic signal detected at $z = z_s$ in the structure shown in the bottom panel of Fig. 3.8a.

For example, when the structure in the bottom panel of Fig. 3.8a has the material properties given in Table 3.2, the acoustic signal detected at $z = z_S$, shown again in

Fig. 3.9, is negligible at frequencies greater than about 200MHz, i.e., $F_{max} = 200\text{MHz}$. Thus, the Nyquist theorem is satisfied if:

$$\delta t \leq 1/(2 \times 200 \times 10^6) = 2.5 \times 10^{-9} s \tag{3.44}$$

Setting the time step to $\delta t = 10^{-10}$s will more than satisfy the inequality and the duration of the frequency spectrum becomes:

$$F_S = 1/\delta t = 1 \times 10^{10}\text{Hz} \tag{3.45}$$

Then, the number of sampling points is defined as $N_{pts} = F_S T$, where F_S is the duration of the frequency spectrum and T is the duration of the temporal profile. When using MATLAB, the number of sampling points is limited by the maximum array size and the amount of memory being used by MATLAB. With access to 7.6GB of memory, MATLAB becomes unresponsive if $N_{pts} > 30 \times 10^6$, thus by setting $N_{pts} = 5 \times 10^6$, the time duration can be calculated as:

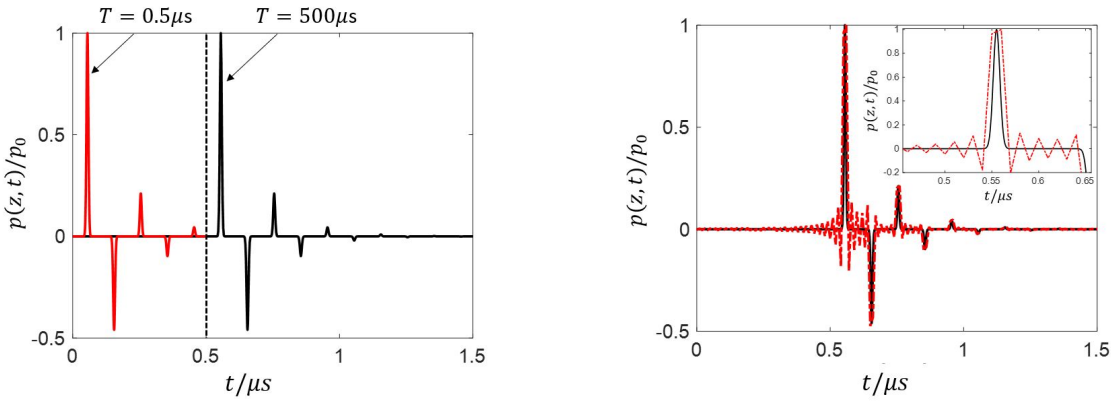
$$T = \frac{N_{pts}}{F_S} = \frac{5 \times 10^6}{1 \times 10^{10}} = 500\mu\text{s} \tag{3.46}$$

With these parameters, the spectrum in Fig. 3.9 has been transformed into the time domain, shown in Fig. 3.10a by a solid black line.

Selecting the appropriate parameters requires an element of compromise between the runtime of the programme and the acceptable resolution. The runtime can be reduced by using fewer sampling points. For example, if the time duration is reduced from $T = 500\mu$s to $T = 0.5\mu$s, the runtime of the programme reduces from 46s to 0.75s. However, the profile, shown in red (dashed) in Fig. 3.10a, suffers from aliasing, such that the signal at $t > T$ has been superimposed over the signal between $0 < t < T$. As a result, the first peak in the acoustic signal appears to arrive at the detector in a tenth of the time than it actually does.

Furthermore, using a larger time step, e.g. $\delta t = 10^{-8}$s, reduces the runtime to just 0.9s but the Nyquist theorem is no longer satisfied and the resultant profile, shown in red (dashed) in Fig. 3.10b, has a significant ringing artifact. The temporal resolution is too low and the shape and amplitudes of the peaks have not been recreated correctly (inset in Fig. 3.10b shows first peak). Therefore, it can be tempting to improve the speed of the programme by increasing the time and frequency step sizes, however, it is crucial to note that this results in a less reliable numeric Fourier transform.

In the spatial domain, the step-size, δz, must be small enough to define the smallest spatial feature. For example, for the structure in the bottom panel of Fig. 3.8a,



(a) (b)

Figure 3.10: Choosing the time duration, T, and time step, δt: in (a) the black (solid) line represents the profile when $T = 500\mu$s and the red (dashed) line represents the profile when $T = 0.5\mu$s. When the time duration is too small, the signal appearing beyond $t = T$ is superimposed over the signal at $0 < t < T$. In (b), the black (solid) line represents the profile when $\delta t = 10^{-10}$s and the red (dashed) line represents the profile when $\delta t = 10^{-8}$s. Because the time steps are too big, the red signal fails to reproduce the shape and height of the correctly sampled signal. (The inset in (b) shows the first peak at 0.55μs in more detail.)

the smallest layer thickness is 0.25mm (Table 3.2) and so a step size of $\delta z = 0.01$mm might appear appropriate. However, there are other characteristic lengths that must be considered: the laser pulse width, the photoacoustic pulse width, and the optical penetration depth. The relationship between the laser pulse width, τ_p, and the photoacoustic pulse width, T_p, is dictated by the short and long pulse regime and will be discussed further in Chapter 4. For now, examples are limited to the long-pulse regime, where the photoacoustic pulse width is always equal to the laser pulse width, i.e.,

$$T_p = \tau_p \tag{3.47}$$

Thus, if the input pulse width is $\tau_p = 10$ns, then the acoustic wavelength of the generated pulse in layer S is:

$$c_S T_p = 0.015\text{mm} \tag{3.48}$$

and so a step size, δz, of 0.001mm is small enough to satisfactorily reproduce the acoustic signal in the spatial domain.

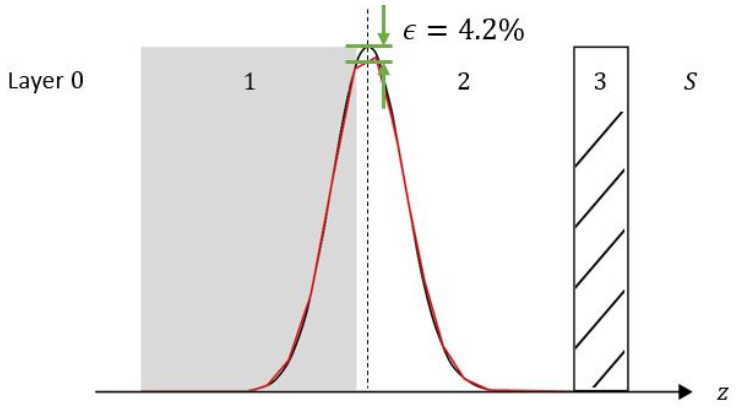


Figure 3.11: Spatial resolution δz: the profile, $p(z,t)$, in black was generated when $\delta z = 0.001$mm. The smallest characteristic length of the structure is the generated pulse width, $T_p = 0.015$mm. Thus, the larger spatial resolution (profile shown in red) does not fully recreate the signal peak: there is an error of about 4% between the peaks produced when $\delta z = 0.01$mm compared to when $\delta z = 0.001$mm.

Fig. 3.11 shows the effects of poor spatial resolution: the normalised pressure has been shown as a function of z when the resolution is only 0.01mm (red, dashed line) and when the resolution is 0.001mm (black, solid line). When the resolution is not fine enough, the peak in the signal has been lost.

To summarise, acoustic signal, $p(z,\omega)$, can be transformed into time domain, using the numeric inverse Fourier transform in MATLAB, but the following steps must be taken to ensure appropriate resolution:

- the acoustic wavelength in the detecting medium must be determined to ensure that the chosen step-size in the spatial domain, δz, is smaller than the characteristic length.

- the step-size in the temporal domain, δt, is determined by the Nyquist theorem ($\delta t \leq 1/(2F_{max})$, where F_{max} is the maximum frequency of the signal and then the sampling rate follows: $F_S = 1/\delta t$

- MATLAB becomes unresponsive if the number of samples, N_{pts}, is too large. Therefore, because N_{pts} is defined as the product of the sampling rate, F_S, and the time duration, T, i.e.,

$$N_{pts} = F_S T \tag{3.49}$$

  then, the time duration, T, can be calculated after determining the limiting value of N_{pts}.

3.6 Summary

To investigate how the acoustic signal generated by a structure with several absorbing layers varies from one with just one absorber, a transfer-matrix model has been derived. Unlike in previous work, the model described in this chapter can simulate structures in which any layer can be absorbing and the degree of absorption is not limited to optically thin layers. In other words, the acoustic signal generated by a multilayered photoacoustic structure with distributed heat source can be simulated. In Section 3.2, the new transfer-matrix model has been described in detail. In Section 3.4, a heating function (Eq. 3.36) has been defined which, contrary to other models, takes into account the attenuation of light in previous layers by defining a local light fluence. The local light fluence depends on the optical absorption profile of the layers, $A(z)$, which is an input function of the model: it can be constant (Fig. 3.7a), decay according to Beer's Law (Fig. 3.7b), or vary as a function of the user's choosing. It will be shown later, in Chapter 5, how a non-uniform heating function effects the acoustic signal generated from a multilayered structure. Finally, in Section 3.5, the pressure in the frequency domain has been transformed into the time domain using the numerical inverse Fourier transform and the resolution and accuracy when using a numeric transform have been discussed. In the next chapter, the formulated model will be used to simulate the acoustic signal generated by a photoacoustic structure with only one optically-absorbing layer and will be verified using analytical results found in previous work.

Chapter 4

Single acoustic source

In Chapter 3, a transfer-matrix method was used to create a one-dimensional model of multilayered photoacoustic structures. By means of a heating function (Eq. 3.36):

$$h(z) = \alpha_q Q_{q-1} A(z), \tag{3.36}$$

any qth layer of the multilayered stack could be an optical absorber, with an optical absorption coefficient, α_q, and thus, be an acoustic source. When irradiated from one side, the light energy was attenuated as it propagated through the absorbing layers according to the optical absorption profile of a layer. When Beer's law was assumed [12, 14, 15, 21, 22], the optical absorption profile of a layer was given by,

$$A(z) = e^{-\alpha_q z}. \tag{4.1}$$

In Fig. 4.1, the heating function from a single absorbing layer, irradiated by light from the left side, is shown for three optical thicknesses. When the absorbing layer (shaded) is optically thin ($\alpha d << 1$), the heating function is constant across the layer (left panel) because $e^{-\alpha d} \to 1$. When the optical thickness is close to 1 (middle panel), the heating function decays exponentially across the whole layer. Finally, when the optical thickness is much greater than 1 (right panel), the heating function decays to zero within the first half of the absorbing layer. Thus, the heating function of an absorber with an optical thickness less than or equal to 1, has a characteristic step feature, resulting from absorption across the whole layer (with thickness, d), as noted in work by Shan et al [14]. However, when the optical thickness is greater than one, the optical penetration depth, $1/\alpha$, becomes the characteristic length scale, because all the input light energy is absorbed within the first half of the layer.

The relationship between the optical absorption coefficient and the width of the generated pulse was explored in work by Cywiak et al [16]. The authors used Green's

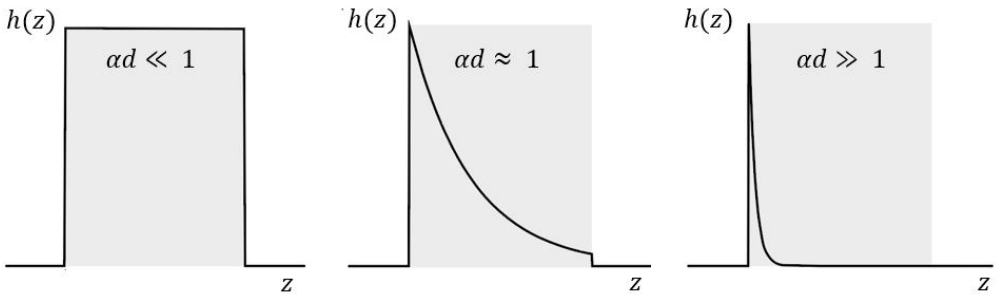


Figure 4.1: Increasing the optical thickness: the heating function, $h(z)$, (Eq. 3.36) is shown for three optical thicknesses, αd, where in all three cases, the optical absorption of the absorber (shaded region) has been assumed to follow Beer's Law.

functions to derive an analytical expression for the impulse and Gaussian response from a single acoustic source, with thickness of 3mm. The authors found that when the absorption was low ($\alpha \leq 10$ cm^{-1}), the temporal width of the photoacoustic pulse was proportional to the absorber thickness. At $\alpha \leq 30$ cm^{-1}, the photoacoustic pulse width was proportional to $1/\alpha$ and when the optical absorption coefficient was increased further, to $\alpha = 100$cm^{-1}, the photoacoustic pulse width was equal to the pulse width of the input light source, τ_p. Thus, the authors concluded that there were three regimes: one where the photoacoustic pulse width was proportional to the layer thickness, d, one where the photoacoustic pulse width was proportional to $1/\alpha$, and one where the photoacoustic pulse width was the same as the input pulse width.

In fact, these three length scales appear repeatedly in studies on the photoacoustic pulse shape [5,12,15,20,21,88] and the identified regimes are commonly referred to as the short- and long-pulse regime. In the short-pulse regime, the photoacoustic pulse has the same shape as the heating function of the layer and in the long-pulse regime, the photoacoustic pulse has the same shape as the input laser pulse.

In this chapter, the effect of the input laser pulse width, optical thickness, and acoustic impedance mismatch on the photoacoustic signal generated from a multilayered stack with only one acoustic source layer will be investigated. In **Section 4.1**, previous work will be reviewed and a structure with no mechanical barriers, i.e., no acoustic impedance mismatches, will be modelled. The generated acoustic signal will be verified with analytical results from Ref. [16]. In **Section 4.2**, mechanical barriers will introduced into the modelled structure. The results will be verified and then, unlike in previous work, the corresponding frequency spectra will be shown. The short and long-pulse regime will be revisited for structures with mechanical barriers and the distinction between the width of the *generated* signal and the width of the *detected* signal will be introduced.

4.1 No mechanical barriers

In Section 3.2, the reflection and transmission coefficients at a single interface were defined in terms of the acoustic impedances on either side of the interface (Eqs. 3.13 and 3.16). If the acoustic impedance is the same on both sides, then there will be no reflections ($r = 0$) and the acoustic signal will be transmitted without attenuation ($t = 1$).

The structure in Fig. 4.2 has no mechanical barriers because all three layers have the same acoustic impedance (Table 4.1). The absorption profile of layer 1 has been assumed to follow Beer's law so that when irradiated by light from the left side, the heating function, $h(z)$, of the absorber (shaded) decays exponentially: when $\alpha d << 1$, the heating function is constant but when $\alpha d \approx 1$, attenuation of light across the layer can be observed. Fig. 4.3 shows the acoustic signal detected in layer 2 for these two

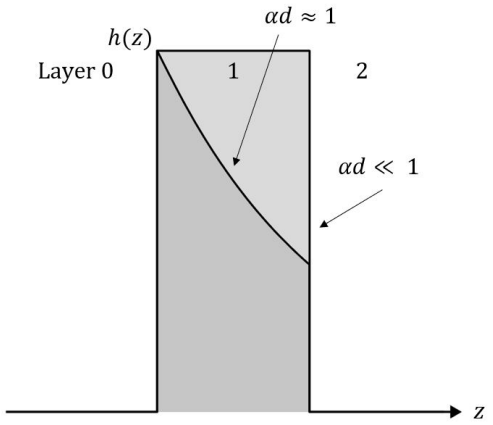


Figure 4.2: The heating function, $h(z)$, in the absorber (layer 1, shaded) depends on the optical thickness, αd.

Layer No.	Material	Z $\times 10^6$/ kg m^{-2} s^{-1}	d/mm
0	Water	1.5	-
1	Water	1.5	3
2	Water	1.5	-

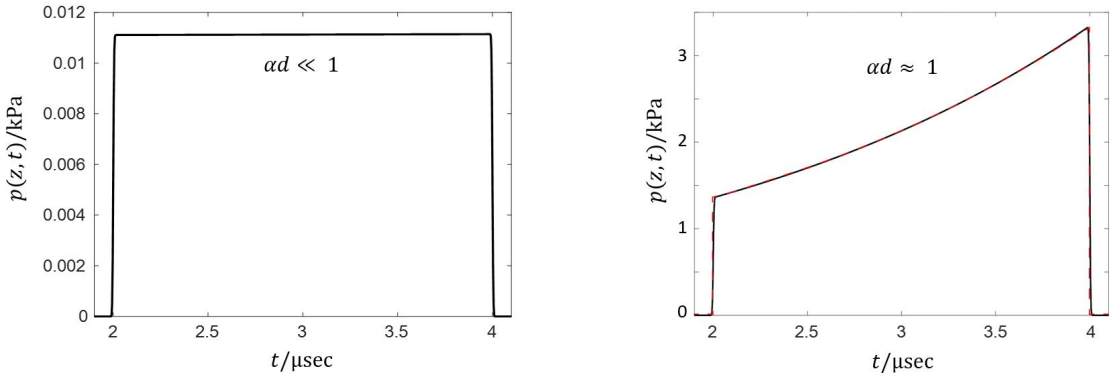
Table 4.1: Layer materials and properties for the structure in Fig. 4.2.

conditions, i.e., in (a) the optical thickness of the absorber is very thin ($\alpha d << 1$) and in (b) the optical thickness is about 1 ($\alpha d \approx 1$). In Fig. 4.3a, the uniform heating function has generated a uniform acoustic signal, with a pulse width, T_p, equal to the sonic transit time across the absorbing layer, i.e.,

$$T_p = d_1/c_1$$

where d_1 and c_1 are the thickness and speed of sound of layer 1. In Fig. 4.3b, the pulse width is still equal to sonic transit time across the absorbing layer ($T_p = d_1/c_1$) but the non-constant heating function has generated a non-constant acoustic signal. Thus, the heating function of the structure can be recreated from the generated acoustic

signal. Fig. 4.3b also shows the analytical results (red-dashed) given by Cywiak et al [16] for the same structure and the model (black) shows good agreement. The model was also verified for several of the different values of the optical absorption coefficient found in Ref. [16] and in each case, the model successfully reproduced the analytical results (not shown) after establishing the appropriate resolution conditions (Chapter 3, Section 3.5).



(a) (b)

Figure 4.3: Optical thickness: the generated acoustic signal from the structure in Fig. 4.2, detected in layer 2, for (a) $\alpha d << 1$ and (b) $\alpha d \approx 1$. The profile in (b), shown in black, has been produced by the model. The red (dashed) line shows the results from Cywiak et al's analytical work [16].

Both of the profiles in the Fig. 4.3 have the same pulse width, T_p. The pulse width of the generated acoustic signal can be predicted using the short- and long-pulse regime. Summarised in the Table 4.2, the regime depends on three key time scales: the input light pulse width, τ_p, the acoustic relaxation time, τ_{aco}, and the generated acoustic pulse width, T_p. The acoustic relaxation time, τ_{aco}, can be considered as the width of the absorbing region and, as shown in Fig. 4.1, is not always equal to d, the thickness of the absorber. Instead, it is defined as

$$\tau_{aco} = \min\left(\frac{1}{\alpha c}, \frac{d}{c}\right), \tag{4.2}$$

so in optically thin absorbers, where $\alpha d << 1$, the acoustic relaxation time is always: $\tau_{aco} = d/c$, where d and c are the thickness and speed of sound, respectively, in the absorber. In optically thick absorbers ($\alpha d >> 1$), the acoustic relaxation time is always equal to $1/(\alpha c)$, where α is the optical absorption coefficient of the layer.

In the short-pulse regime, the width of the input light pulse is always less than the acoustic relaxation time, i.e.,

$$\tau_p << \tau_{aco} \tag{4.3}$$

	optically thin ($\alpha d << 1$, $\tau_{aco} = d/c$)	**optically thick** ($\alpha d >> 1$, $\tau_{aco} = 1/(\alpha c)$)
short-pulse regime $\tau_p << \tau_{aco}$	$\boldsymbol{T_p = d/c}$, Refs. [12–16, 18, 23, 78]	$\boldsymbol{T_p = 1/(\alpha c)}$, Refs. [13–16, 21]
long-pulse regime $\tau_p >> \tau_{aco}$	$\boldsymbol{T_p = \tau_p}$, Refs. [12, 15, 16, 18, 50, 76]	$\boldsymbol{T_p = \tau_p}$, Refs. [15, 16, 22, 50, 76]

Table 4.2: Defining the acoustic pulse width, T_p, using the short and long-pulse regime: the shaded regions of the table represents the regions in which the acoustic wavelength is equal to or smaller than the thickness of the absorber, d. For optically-thin absorbers, where the optical thickness, αd, is much less than 1, the acoustic relaxation time is given by $\tau_{aco} = d/c$, where c is the speed of sound of the absorber. For optically-thick absorbers, where $\alpha d >> 1$, the acoustic relaxation time is $\tau_{aco} = 1/(\alpha c)$, where α is the optical absorption coefficient of the absorbing layer. References are given to previous work done in each region.

and thus, the generated acoustic signal has a pulse width, T_p, equal to the acoustic relaxation time:

$$T_p = \tau_{aco}. \tag{4.4}$$

As will become clear in Chapter 6, it also useful to note that, in the short pulse regime, the generated acoustic pulse has a wavelength, cT_p, given by:

$$cT_p = c\tau_{aco} \leq d, \tag{4.5}$$

in other words, the acoustic wavelength is always smaller than or equal to the dimensions of the absorber.

In the long pulse-regime, the width of the input light pulse is greater than the acoustic relaxation time of the structure:

$$\tau_p >> \tau_{aco} \tag{4.6}$$

and the generated acoustic pulse width, T_p, is defined as:

$$T_p = \tau_p \tag{4.7}$$

Like in the short-pulse regime, the acoustic relaxation time can take two values (Eq. 4.2), and so the long-pulse regime can be divided into two sub-regions:

1. When $\tau_{aco} = d/c$: by definition, in the long-pulse regime, $\tau_p >> \tau_{aco}$ and $T_p = \tau_p$, hence $T_p >> \tau_{aco}$. Thus, if $\tau_{aco} = d/c$, then the generated acoustic signal will always have a wavelength, cT_p, that is greater than the dimensions of the absorber.

2. When $\tau_{aco} = 1/(\alpha c)$: in the long-pulse regime, the input light pulse width and generated acoustic pulse width are greater than the acoustic relaxation time; however, this does not mean that T_p is always greater than d/c. Two scenarios exist, either:

   - $d/c > T_p >> \tau_{aco}$ or,
   - $T_p > d/c >> \tau_{aco}$.

   In the former case, the generated acoustic signal has a wavelength, cT_p, smaller than the thickness of the absorber, d, whereas in the latter case, the acoustic wavelength is greater than the dimensions of the absorber.

Identifying which regions of the short- and long-pulse regime are subwavelength will be of great use in future chapters, where subwavelength structures have been designed to enhance the generated photoacoustic signal.

Returning to the profiles in Fig. 4.3, the absorbing layer has been irradiated by light in the short-pulse regime and so, when the absorber is optically thin, the acoustic pulse width in (a) is: $T_p = d/c$. When the absorbing layer has an optical thickness equal to one, the layer is neither optically thick or thin, but is at the transition between the two. Hence, in the short-pulse regime, the generated acoustic signal in (b) has an acoustic pulse width, T_p, equal to the acoustic relaxation time, where:

$$\tau_{aco} = 1/(\alpha c) = d/c \tag{4.8}$$

and so both signals in Fig. 4.3 have the same acoustic pulse width.

The generated acoustic signal has also been simulated in the frequency domain in Fig. 4.4. The optically-thin absorber generated a (shifted) rectangular acoustic signal in the time domain (Fig. 4.3a) and thus, the Fourier transform pair of the acoustic signal in the time and frequency domain can be expressed mathematically as:

$$p_{max}\Pi\left(\frac{t - 3T_p/2}{T_p}\right) \Leftrightarrow p_{max}T_p e^{-i3\omega/2}\frac{\sin(\omega T_p/2)}{\omega T_p/2} \tag{4.9}$$

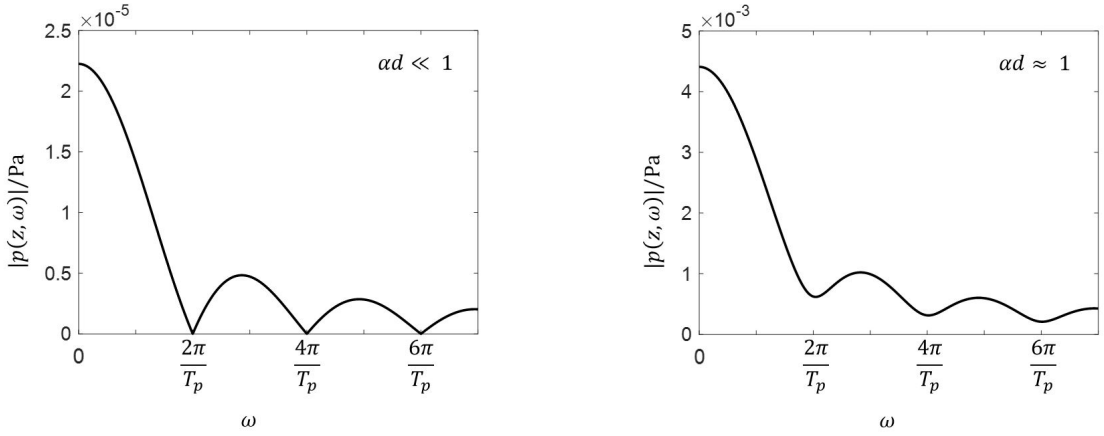


Figure 4.4: Optical thickness in the frequency domain: the generated acoustic signal is shown in the frequency domain when (a) $\alpha d << 1$ and (b) $\alpha d \approx 1$. The loss of the rectangular shape in the temporal profile of the optically thick structure (Fig. 4.3b) removes the zeros in the frequency spectrum in (b).

where, the rectangular function, $\Pi(t)$, is defined as [89],

$$\Pi(t) = \begin{cases} 0, & \text{for } |t| > 1/2 \\ 1/2, & \text{for } |t| = 1/2 \\ 0, & \text{for } |t| < 1/2 \end{cases} \tag{4.10}$$

and p_{max} is the maximum amplitude of the $p(z,t)$ in Fig. 4.3a. Thus, when $\alpha d << 1$, the frequency spectrum has zero values when $|\sin(\omega T_p/2)| = 0$, i.e., when $\omega T_p/2 = 0, \pi, 2\pi$, etc.

When the optical thickness is equal to one, the frequency spectrum is no longer a sinc function, with zeroes at even multiples of π/T_p, because the temporal profile is not a rectangular function. Instead, the shape of the temporal profile in Fig. 4.3b mirrors that of the absorption profile, which follows Beer's law ($A(z) = e^{-\alpha z}$). Thus, the Fourier pair can be expressed analytically (see Appendix A for full derivation) as:

$$p_{max} e^{+\alpha c(t-T_p)} \Pi\left(\frac{t - 3T_p/2}{T_p}\right) \Leftrightarrow p_{max} T_p e^{-i3\omega/2} e^{+\alpha c \frac{T_p}{2}} \frac{\sin\left[(\omega + i\alpha c)T_p/2\right]}{\left[(\omega + i\alpha c)T_p/2\right]}, \tag{4.11}$$

where T_p is the width of the pulse in Fig. 4.3b and p_{max} is the magnitude of the acoustic signal at $t = 2\mu$s.

Thus, the presence of the $\alpha c T_p$ term in Eq. 4.11 removes the zeroes in the frequency spectrum at $\omega = \frac{2\pi}{T_p}, \frac{4\pi}{T_p}$, etc. because at these frequencies:

$$\sin\left[(\omega + i\alpha c)T_p/2\right] = \cos\frac{\omega T_p}{2} \sin i\frac{\alpha c T_p}{2} \neq 0, \tag{4.12}$$

where α and c are the absorption coefficient and the speed of sound in the absorbing layer, respectively, and T_p is the width of the generated acoustic signal.

In this example, the width of the acoustic pulse is $T_p = d/c$, because the layer is irradiated by light in the short-pulse regime and the acoustic relaxation time is $\tau_{aco} = d/c$. Thus, $\alpha c T_p = \alpha d$, and hence, when $\alpha d << 1$, the expressions in Eq. 4.11 simplify to those for the shifted rectangular function in Eq. 4.10.

In summary, the model has been verified using analytical results from Ref. [16] for a structure with a single absorber with no mechanical barriers. The effect of the optical thickness of the absorber on the generated signal has been investigated in the time domain, and also, unlike in previous work, in frequency domain. The latter will be particularly useful in later chapters when frequency-selective structures have been modelled. It has been shown that the profiles in the time and frequency domain vary with the optical thickness and, thus, it is key strength of the formulation in Chapter 3 that these effects can be modelled. The short- and long-pulse regime, which defines the width of the generated acoustic signal, T_p, in terms of the input light pulse width, τ_p, and the acoustic relaxation time, τ_{aco}, has been discussed and the sub-regions which produce signals with an acoustic wavelength, cT_p, smaller than the dimensions of the absorbing layer have been identified.

4.2 Mechanical barriers

In the previous section, the photoacoustic signal generated from a single optical absorber with no mechanical barriers was investigated. Without reflections, it was straightforward to observe how the generated pulse width, T_p, depended on the optical thickness, αd and the input light pulse width, τ_p, according to the short- and long-pulse regime.

However, in most applications, structures contain mechanical barriers. Indeed, most applications make use of the interaction of the photoacoustic signal with a mechanical barrier. For example, in work by Lee et al [50, 76], the emission efficiency of an acoustic source in one direction was improved by placing a backing layer, with a different acoustic impedance to the acoustic source, on the irradiated side of the acoustic source, as shown in Fig. 4.5.

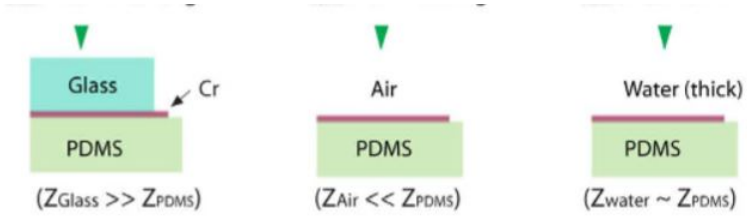


Figure 4.5: Different backing layers: the three structures investigated by Lee et al (from Fig. 1(b) in Ref. [76]) with glass, air, and water acting as three different backing layers.

Components of the acoustic signal that were travelling towards the irradiated side of the source, were reflected at the interface with the backing layer and travelled back towards a detector, positioned on the opposite side of the source. In this way, half of the acoustic signal was not lost, travelling in the opposite direction to the detector. The authors also investigated the temporal overlap of the reflected pulses to produce negative quasi-monopolar waveforms [76]. Detected photoacoustic pulses are usually made up of a positive and negative peak, described by Gutierrez-Reyes et al [22] as resembling 'two consecutive triangles, one positive and the other negative'. A monopolar photoacoustic pulse is difficult to produce using conventional techniques. However, by positioning a backing layer at a specific distance away from the acoustic source, Lee et al [76] reflected the acoustic signal and created a time delay between the unreflected and reflected components, thus separating in time the 'two consecutive triangles'. Using the same acoustic source, observable differences in the generated waveform could be produced by using different backing materials. Furthermore, the overlap of the unreflected and reflected pulses was dependent on the width of the input light pulse. An input light source in the short-pulse regime ($\tau_p << \tau_{aco}$) minimised any overlap, while an input light source in the long-pulse regime generated a long photoacoustic pulse and the time delay created by the backing layer was no longer sufficient to completely separate the unreflected and reflected components.

The addition or cancellation of overlapping photoacoustic pulses, created by the reflection of acoustic waves at an interface, was also explored by Rajagopal and Cox [15]. The authors found that by operating in the long-pulse regime, larger photoacoustic amplitudes could be achieved from weakly absorbing materials compared to strongly absorbing materials, due to the elongation of the photoacoustic pulse. Some of their analytical results (red, dashed line) have been recreated in Fig. 4.7 to verify the model (black, solid line). For the structure shown in Fig. 4.6 with properties given in Table 4.3, when the epoxy layer is weakly-absorbing, the normalised pressure, $\hat{p}$,

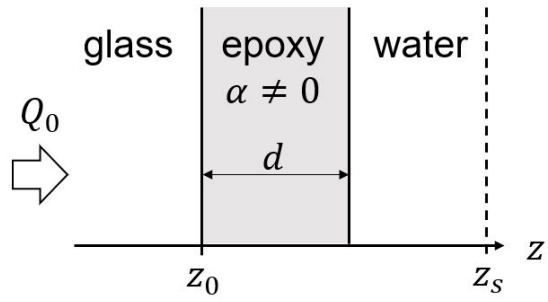
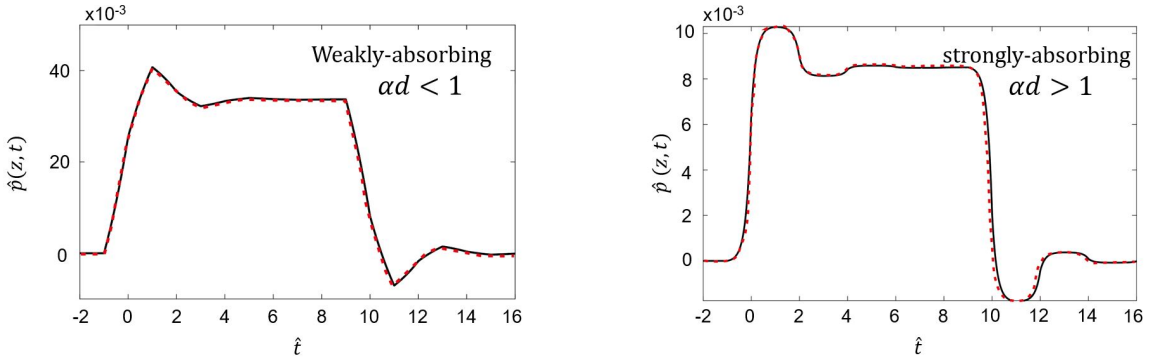


Figure 4.6: Two mechanical barriers surround the epoxy absorber (shaded) which is irradiated by light, with fluence, Q_0, from the left. A detector is positioned at $z = z_s$ to record the generated acoustic signal.

Layer No.	Material	Z $\times 10^6$/ kg m^{-2} s^{-1}	d/μm
0	Glass	12.4	-
1	Epoxy	3.1	50
2	Water	1.5	-

Table 4.3: Layer materials and properties for the structure in Fig. 4.6



(a) (b)

Figure 4.7: Superposition in the long-pulse regime: when the acoustic wavelength is greater than the dimensions of the structure (Fig. 4.6), reflections of the generated acoustic signal overlap to create signals with greater amplitude. The normalised acoustic signal, $\hat{p}$, at z_s has been simulated when the optical absorption coefficient of the epoxy layer was (a) $\alpha = 10^4 \text{m}^{-1}$ ($\tau_{aco} = 20$ns) and (b) $\alpha = 10^5 \text{m}^{-1}$ ($\tau_{aco} = 4$ns). The width of the input light pulse was $\tau_p = 200$ns (long-pulse regime). The model (black line) formulated in Chapter 3 shows good agreements with the analytical work (red, dashed line) by Rajagopal and Cox [15], where the same normalisation factors have been used as in Ref. [15].

reaches a greater maximum amplitude compared to the strongly-absorbing case because the epoxy layer is optically thin ($\alpha d < 1$) and so all of the absorber acts as an acoustic source. In contrast, recall from Fig. 4.1 that in optically thick absorbers ($\alpha d > 1$), most of the light energy was absorbed within the first half of the layer, and thus the acoustic signal originating from the second half was negligible. This means that in the weakly-absorbing structure, there are more reflections, and hence more

opportunity for overlap, and the result is an increase in the magnitude of $\hat{p}$.

The model performs well and recreates the analytical results derived by Rajagopal and Cox [15], which differ from Cywiak's derivation [16] because the absorber and surrounding substrate can have different acoustic impedances.

The reflection and transmission of generated acoustic signals at a mechanical barrier will be explored in the following section. First, the effect of a single mechanical barrier (e.g., a backing layer) on the shape of the detected acoustic signal is investigated and the validity of the short and long pulse regime is discussed. Then, two mechanical barriers are considered, resulting in infinite reflections. Unlike in work by Lee et al [76] and Rajagopal and Cox [15], the effect of multiple mechanical barriers on the frequency spectrum of detected signals will also be analysed.

4.2.1 One mechanical barrier

Consider the photoacoustic structure in Fig. 4.8 (with material properties shown in Table 4.4). When irradiated by light in layer 0, the photoacoustic source (shaded,

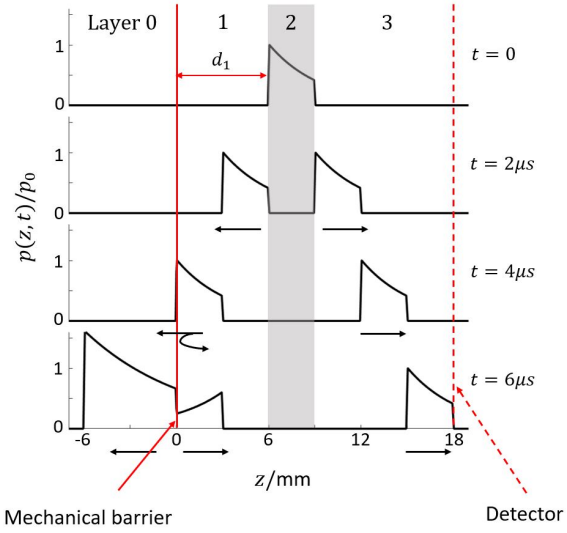
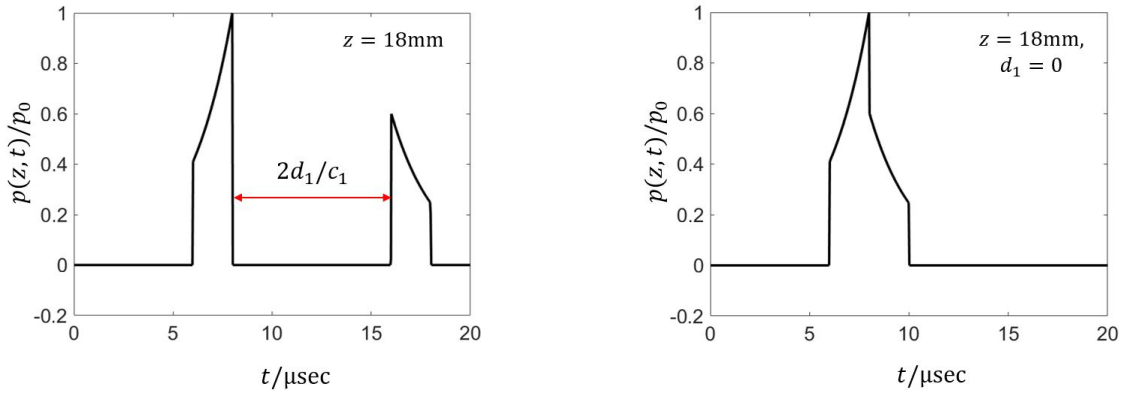


Figure 4.8: Reflections at a mechanical barrier: the acoustic signal generated in layer 2 (top) has a left and right-travelling component that travel away from the absorber (second panel). At $t = 4\mu$s (third panel), the left-travelling component reaches a mechanical barrier and reflections occur (bottom).

Layer No.	Material	Z $\times 10^6$/ kg m^{-2} s^{-1}	d/mm	α/m^{-1}
0	-	6	-	0
1	Water	1.5	6	0
2	Water	1.5	3	300
3	Water	1.5	-	0

Table 4.4: Layer materials and properties for the structure in Fig. 4.8

layer 2) generates an acoustic signal at $t = 0$ (top panel). In the second panel,



(a) (b)

Figure 4.9: Detected pulse width: for the structure in Fig. 4.8, the acoustic signal detected at a fixed z-position ($z = 18$mm) has been shown as a function of time. In (a) layer 1 has a thickness of d_1. In (b), $d_1 = 0$ and the time delay between unreflected and reflected signals disappears, resulting in a *detected* signal with double the pulse width of the *generated* signal.

the right- and left-travelling components of the acoustic signal propagate out of the source in opposite directions but with an equal maximum amplitude of p_0. Then, at $t = 4\mu$s (third panel), the left-travelling component reaches a mechanical barrier and reflections occur (bottom panel). As derived in Chapter 3, for an acoustic wave passing from medium 1 to medium 0, the reflection and transmission coefficients are:

$$r_{10} = \frac{Z_0 - Z_1}{Z_1 + Z_0} \tag{4.13}$$

$$t_{10} = \frac{2Z_0}{Z_1 + Z_0}. \tag{4.14}$$

In Fig. 4.8, the acoustic impedance in layer 0 is $4Z_w$ and the acoustic impedance in layers 1, 2, and 3 is Z_w, where the subscript w is used to represent water. Thus, $r_{10} = +0.6$ and the reflected component in the bottom panel of Fig. 4.8 is now right-travelling and has a maximum amplitude equal to $0.6p_0$. In contrast, the component transmitted into layer 0 has been amplified because $t_{10} = 1.6$ and continues to propagate to the left. In Fig. 4.9a, the acoustic signal recorded at the detector at $z = 18$mm has been simulated as a function of time. As expected, the unreflected right-travelling components arrives first, at $t = 6\mu$s, and then the attenuated reflected component arrives $2d_1/c_1$ seconds later. Hence, the time delay between the unreflected and reflected components depends on the thickness of layer 1, d_1 [50]. If $d_1 = 0$, the reflected component will arrive immediately after the unreflected component and, as shown in

Fig. 4.9b, the pulse recorded at the detector will have a pulse width of $2T_p$, where T_p is width of the unreflected acoustic signal.

Thus, when structures have mechanical barriers, the *generated* acoustic signal has a pulse width, T_p, that follows the short- and long-pulse regime, but the *detected* signal may not, depending on the proximity of a mechanical barrier to the absorber.

4.2.2 Multiple mechanical barriers

In the previous section, a single mechanical barrier between layer 0 and 1 caused the reflection of the left-travelling component of the generated acoustic signal. If a second mechanical barrier is added, this time between layers 1 and 2, then both the left- and right-travelling components will be reflected - and not just once. Acoustic waves bounce back and forth between the two mechanical barriers so that rather than just one echo, the acoustic signal detected to the right of the source, is composed of a train of echoes.

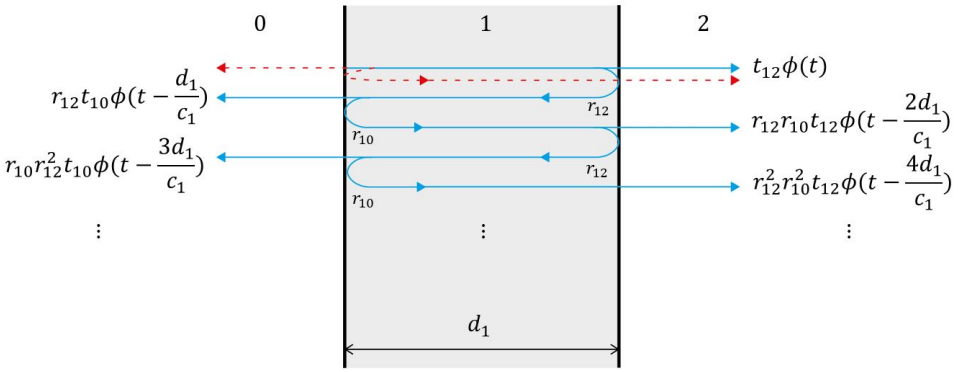


Figure 4.10: An illustration of repeated reflections: when the acoustic source (layer 1) has a different acoustic impedance to the surrounding substrate (layers 0 and 2), the generated acoustic signal bounces back and forth between the two interfaces and reflection and transmission occurs at every bounce. The signal detected in layer 2 is the sum of the transmitted left- (red, dashed) and right-travelling components (blue).

In Fig. 4.10, the path of an acoustic signal generated in the absorbing layer (layer 1) has been illustrated. The right-travelling components are shown in blue (solid): they bounce back and forth between the two interfaces and reflected components are diminished by r_{12} at the right interface and by r_{10} at the left interface. Components transmitted into layer 2 are diminished by t_{12}. Thus, a detector placed in layer 2, will

record the sum of these transmitted components:

$$p_R(z,t) = t_{12}\phi(t) + r_{12}r_{10}t_{12}\phi(t - \frac{2d_1}{c_1}) + r_{12}^2 r_{10}^2 t_{12}\phi(t - \frac{4d_1}{c_1}) + ...$$
$$= t_{12}\sum_{n=0}^{\infty}(r_{12}r_{10})^n\phi(t - n\frac{2d_1}{c_1}), \tag{4.15}$$

where $\phi(t)$ represents the phase shift associated with waves propagating across the distance d_1. However, Eq. 4.15 only takes into account the right-travelling components and their reflections. If they are reflected at the left interface an odd number of times, then left-travelling components (shown in red in Fig. 4.10) also reach layer 2 and can be expressed as:

$$p_L(z,t) = r_{10}t_{12}\sum_{n=0}^{\infty}(r_{12}r_{10})^n\phi(t - n\frac{2d_1}{c_1}), \tag{4.16}$$

and hence, the total signal detected in layer 2 is given by the sum of the transmitted left and right components, i.e.,

$$p(z,t) = p_R + p_L = t_{12}(1 + r_{10})\sum_{n=0}^{\infty}(r_{12}r_{10})^n\phi(t - n\frac{2d_1}{c_1}). \tag{4.17}$$

If the substrates (layers 0 and 2) have the same material properties then $r_{10} = r_{12}$ and $t_{10} = t_{12}$, and Eq. 4.17 can be simplified to:

$$p(z,t) = t_{12}(1 + r_{12})\sum_{n=0}^{\infty}(r_{12})^{2n}\phi(t - n\frac{2d_1}{c_1}) \tag{4.18}$$

In Fig. 4.11, the acoustic signal generated from a single absorber sandwiched between two mechanical barriers has been modelled. In the structure in Fig. 4.11a the acoustic impedance in the absorber, Z_1, is greater than in the substrates, $Z_0 = Z_2$, and the acoustic impedance mismatch, $\hat{Z} = Z_1/Z_0 > 1$. In the structure in Fig. 4.11b, the acoustic impedance mismatch between the absorber and the substrate is less than 1, i.e., $\hat{Z} < 1$. Also shown in Figs. 4.11a and 4.11b are the heating functions of the absorbing layer. In both cases, the absorber is optically thin and so, when irradiated by light in the short-pulse regime, the heating function is uniform.

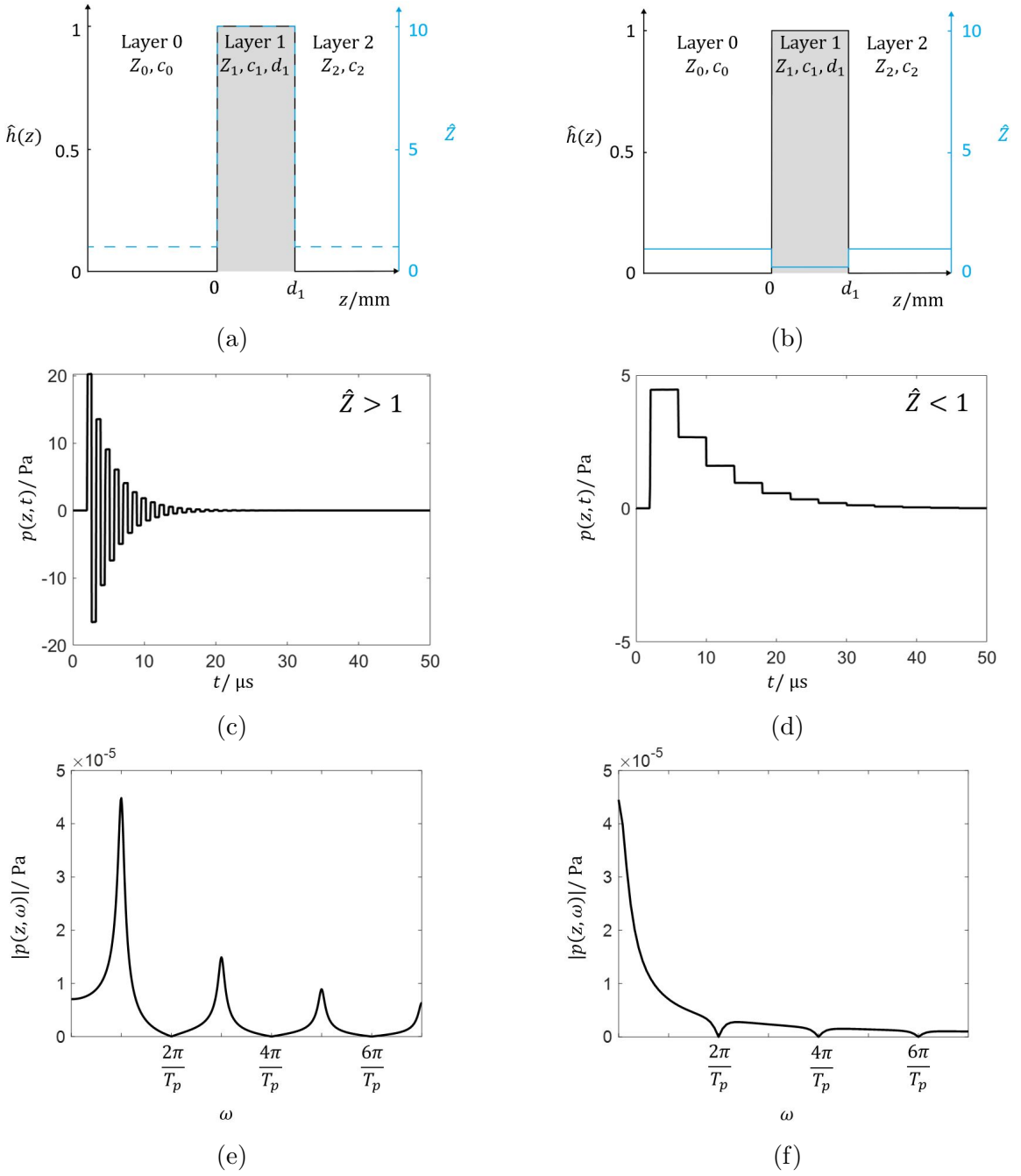


Figure 4.11: Acoustic impedance mismatch: in the left panel the acoustic impedance mismatch is greater than 1 ($\hat{Z} = 10$) and so reflections of the generated signal are inverted and attenuated. The temporal profile in (c) oscillates between negative and positive pressure, with a period of $2T_p$. In the corresponding frequency spectrum (e), there are resonant peaks at odd integer values of π/T_p, due to the oscillation in the time domain. In the right panel, $\hat{Z} = 0.25$, and the reflected components in the profile in (d) are all positive and as a result the *detected* signal does not drop to zero until about $t = 30\mu$s. There are no distinct resonant peaks in the corresponding frequency spectrum in (f).

Figs. 4.11c and 4.11d show the acoustic signal detected in layer 2 as a function of time. In Fig. 4.11c, the acoustic impedance mismatch, $\hat{Z} = 10$ and so the reflected left-travelling component and its echoes are all negative and account for the signal where $p(z,t) < 0$. The echoes of the right and left travelling components both decay in magnitude by r_{10}^2 and all have a pulse width, T_p, equal to the sonic transit time across layer 1, i.e.,

$$T_p = d_1/c_1 \tag{4.19}$$

where d_1 and c_1 are the thickness and speed of sound in layer 1. In this example, $T_p = 0.6\mu$s.

In contrast, in Fig. 4.11d, where the acoustic impedance mismatch is less than 1 ($\hat{Z} = 0.25$), the reflected left-travelling component and its echoes are positive and thus, like in Fig. 4.9b, they arrive at the detector in layer 2 immediately after the unreflected right-travelling component and its echoes. Hence, although the *generated* acoustic signal has a pulse width of $T_p = d_1/c_1 (= 4\mu$s), the *detected* acoustic signal falls back to zero for about 30μs.

The acoustic impedance of the absorbers in Fig. 4.11a and Fig. 4.11b are different and hence, the reflection and transmission coefficients are not the same. Thus, the magnitude of the detected signals in Figs. 4.11c and 4.11d are different. Furthermore, the higher acoustic impedance in the absorber in Fig. 4.11a also means that the speed of sound, c_1, is greater than in Fig. 4.11b. Thus, generated acoustic pulse width, defined in Eq. 4.19, is smaller.

In the corresponding frequency spectra, shown in Fig. 4.11e and 4.11f, both signals produce zeroes when the frequency is equal to an even integer value of π/T_p, because of the rectangular shape of temporal profile (Section 3.1). In Fig. 4.11e, where $\hat{Z} > 1$, the spectrum has distinct resonant peaks when the frequency is equal to odd integer values of π/T_p. This is because the temporal profile oscillates, with a period of $2T_p$, between positive and negative pressure, due to the negative reflection coefficient, r_{10}. When $\hat{Z} < 1$, the reflection coefficient, r_{10}, is positive and so the corresponding frequency spectrum in Fig. 4.11f does not display strong resonance and instead, the maximum amplitude occurs at zero frequency.

Therefore, along with the optical thickness (Section 3.1), the acoustic impedance mismatch of the absorber with the surrounding media, $\hat{Z}$, also changes the behaviour of the acoustic signal. The magnitude of the temporal signal is either diminished or increased, depending on the sign of the reflection and transmission coefficients.

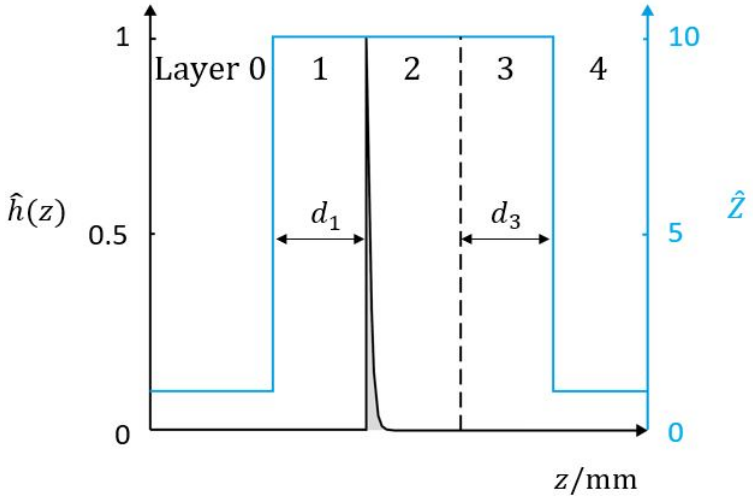


Figure 4.12: Sliding the absorber: the position of the acoustic source (layer 2) between the two interfaces is controlled by varying d_1 and d_3. The optical thickness of layer 2 is now so large ($\alpha d_2 >> 1$) that the acoustic signal is only generated in the first half of the layer. The acoustic impedance mismatch, $\hat{Z}$, is shown in blue. Relative to the substrates (layers 0 and S), the acoustic impedance in layers 1-3 is 10 times greater.

Furthermore, the shape of the detected signal depends not only on the reflection and transmission coefficients, but also on the distance from the acoustic source to the mechanical barrier. In Fig. 4.12, the acoustic source is now positioned a distance of d_1 and d_3 away from the left and right interfaces, respectively. Moving the absorber between these two interfaces by controlling d_1 and d_3, will change the time delay between components of the echo train.

For example, for the structure shown in Fig. 4.12, the acoustic signal detected in layer 4 has been modelled when the acoustic impedance mismatch is greater than 1 ($\hat{Z} = 10$) in Fig. 4.13. All the layers inside the mechanical barriers have the same acoustic impedance ($Z_1 = Z_2 = Z_3$). Thus, reflections only occur at the interface between layers 1 and 0 and between layers 3 and 4.

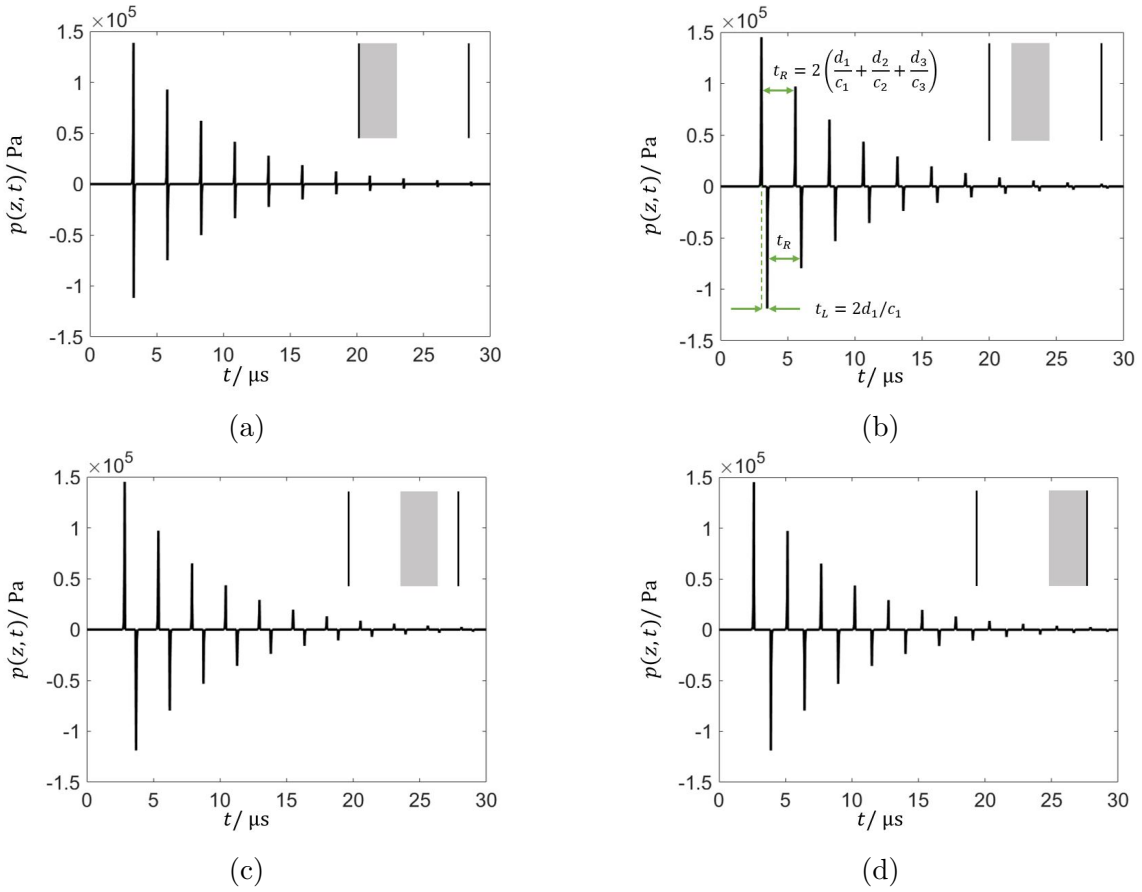


Figure 4.13: Controlling time delay: the detected acoustic signal in layer 4 when (a) $d_1 = 0, d_3 = 3$mm, (b) $d_1 = 1, d_3 = 2$mm, (c) $d_1 = 2, d_3 = 1$mm, and (d) $d_1 = 3, d_3 = 0$mm. The insets in each figure show the position of layer 2 (shaded) relative to the two interfaces.

When $d_1 = 0$, the absorber is adjacent to the interface at layer 0 and so left-travelling components are reflected and inverted and immediately follow the unreflected right-travelling waves. Hence, in Fig. 4.13a, there is no time delay between the first positive peak and the first negative peak (inset). Their subsequent reflections arrive after:

$$t_R = 2\left(\frac{d_1}{c_1} + \frac{d_2}{c_2} + \frac{d_3}{c_3}\right). \tag{4.20}$$

When $d_1 = 1$ in Fig. 4.13b, a time delay, t_L, is introduced between the unreflected right-travelling components and the reflected left-travelling components, where;

$$t_L = \frac{2d_1}{c_1} \tag{4.21}$$

The time delay, t_L, doubles when $d_1 = 2$ in Fig. 4.13c and when $d_1 = 3$, the train of positive and negative peaks are equally spaced, i.e., $t_L = t_R/2$.

In this example, the absorber was irradiated by light from layer 0 in the short-pulse regime. The absorber was optically thick ($\alpha d_2 >> 1$) and so the generated acoustic pulse width was equal to $T_p = 1/(\alpha c_2)$. As a result, echoes cannot overlap and so the magnitude cannot be increased by superposition as was done in Rajagopal and Cox's work [15]. However, the ability to control the time delay between pulses, particularly between pulses of opposite polarity, may be of use in imaging and cavitation applications, where waveform shaping is necessary [76, 90].

4.3 Summary

Understanding the behaviour of the generated acoustic signal, including its shape, width, and amplitude, is vital for most applications. In this chapter, photoacoustic structures with a single optical absorber have been modelled. In Section 4.1, the model derived in Chapter 3 was used to simulate the acoustic signal generated by a single absorbing layer in a structure with no mechanical barriers and:

- the model was verified using the analytical results derived by Cywiak et al [16] and, providing the appropriate resolution conditions were satisfied, the model successfully recreated the temporal profiles.

- the short- and long-pulse regime, which defines the width of the generated acoustic pulse, T_p, was reviewed and then the sub-regions which produce pulses with widths smaller than the dimensions of the absorber were identified. This is necessary information for later chapters, where subwavelength structures will be designed to enhance the performance of a photoacoustic structure.

- The frequency spectrum from an optically thin absorber was compared to the spectrum from an optically thick absorber and the analytical expressions for $p(z, \omega)$ were defined in order to explain any differences. This will be useful for later analysis when more absorbers are considered.

However, most applications require structures made up of several materials, and thus, in Section 4.2, mechanical barriers were introduced. It was found that:

- With just one mechanical barrier, acting as a backing layer, the generated left-travelling components could be reflected back toward a detector on the right instead of being lost to the semi-infinite substrate. If the mechanical barrier was adjacent to the absorbing layer, then the reflected component arrived at

the detector immediately after the unreflected component, and hence the pulse at the detector had a width of $2T_p$.

- If irradiated by light in the long-pulse regime, reflected components overlap and the superposition of the signals results in an increased signal amplitude at the detector. Analytical results derived by Rajagopal and Cox [15] were used to verify the model for a structure with mechanical barriers.

- It was established that, although the short and long-pulse regime can be used to calculate the *generated* acoustic pulse width, T_p, the *detected* pulse width depends on the position of mechanical barriers relative to the acoustic source.

- An absorber sandwiched between two mechanical barriers will produce infinite reflections of the generated signal. The summation of the transmitted components at a detector has been expressed mathematically and was used to explain the pulse train of echoes found in the temporal profile of the signal. Unlike in work by Cywiak et al [16] and Rajagopal and Cox [15], the corresponding frequency spectrum was also analysed and it was found that when the acoustic impedance mismatch, $\hat{Z}$, was greater than 1, the spectrum had distinct resonant peaks when the frequency was an odd integer of π/T_p, due to the oscillation between positive and negative pressure (period $2T_P$). When the acoustic impedance mismatch was less than 1, the reflection coefficient was positive and so the $2T_p$-period oscillations were less pronounced and hence, the resonant peaks at odd integer values of π/T_p were less distinct.

- Finally, the time delay between the echoes in the infinite pulse train was controlled by sliding the absorbing layer to the left and right between two mechanical barriers. In the short-pulse regime, these echoes cannot overlap but the ability to separate the positive peaks from the negative peaks is useful in biomedical applications [76].

In the next chapter, not only will structures have mechanical barriers, but they will also have several acoustic sources.

Chapter 5

Distributed heat sources

In most previous work, including the work by Cywiak et al [16] and by Rajagopal and Cox [15] discussed in Chapter 4, the photoacoustic structures modelled contained only one optical absorber. Analytical expressions could be derived to calculate the acoustic signal generated from an optically thin or thick absorber, irradiated by light in the short- or long-pulse regime (Table 4.2). As discussed in Chapter 4, the use of mechanical barriers, and the subsequent reflection of the acoustic signal, can be used to:

- direct more of the signal (comprised of a left- and right-travelling component) toward a detector on one side of the acoustic source [76],
- combine or separate unreflected and reflected components to create wider or monopolar peaks [50, 76],
- and, when operating in the long-pulse regime, increase the amplitude of detected signals by overlapping reflections [15].

Thus, a range of enhancements can be induced by careful design of the material properties and geometry of the structure with just a single absorber.

However, multilayered photoacoustic structures with several source layers can also produce signals with the desired enhancement too. Consider the simple single-absorber structure shown in Fig. 5.1a. A mechanical barrier exists between layer 0 and 1, shown with a dashed, black line, and the acoustic impedance mismatch, $\hat{Z}$, between each layer relative to layer 3 has been given on the right-hand axis (in blue). When left-travelling components generated in absorbing layer (shaded, layer 2) arrive at the mechanical barrier, reflection and transmission occurs and the reflection and

transmission coefficients (Eqs. 3.13 and 3.16) are given by:

$$r_{10} = \frac{Z_0 - Z_1}{Z_0 + Z_1} = \frac{1 - \hat{Z}}{1 + \hat{Z}} \tag{5.1}$$

$$t_{10} = \frac{2Z_0}{Z_0 + Z_1} = \frac{2}{1 + \hat{Z}} \tag{5.2}$$

The heating function, $h(z)$, of the structure is also shown in black in Fig. 5.1a, and is constant across layer 2 because the absorber has been assumed to be optically thin ($\alpha d << 1$).

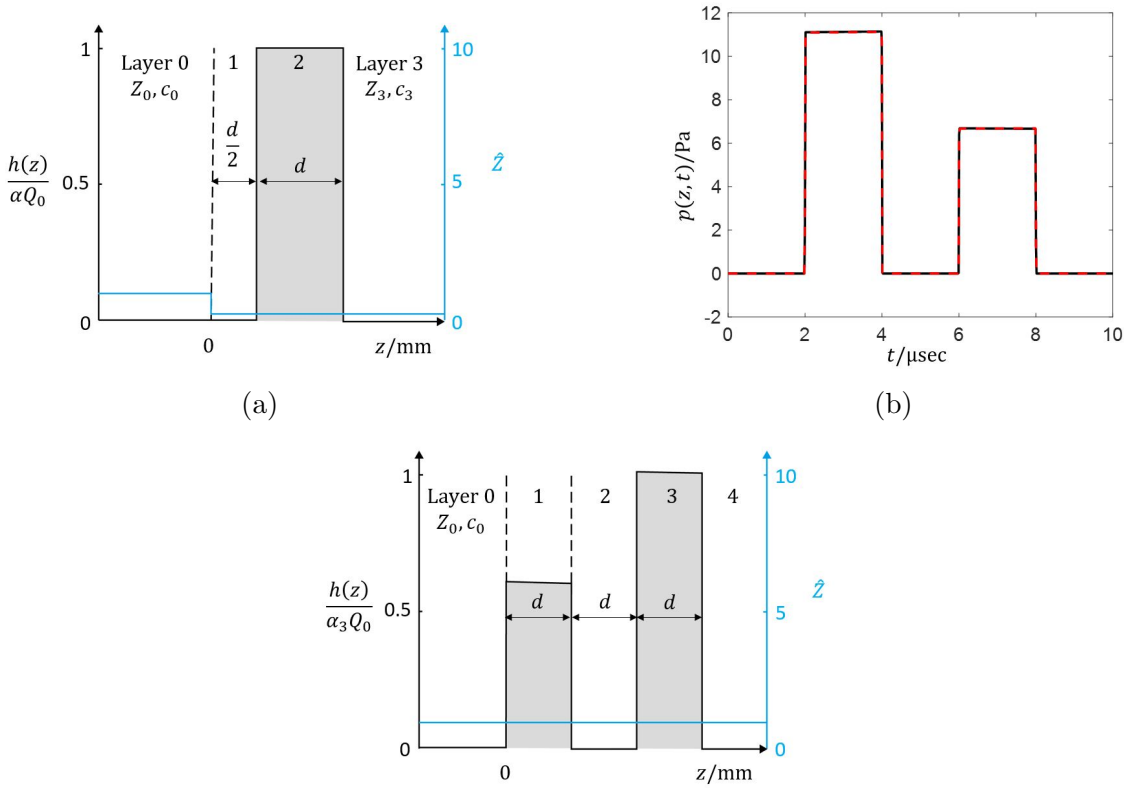


Figure 5.1: Mechanical barriers vs. distributed heat sources: the same acoustic signal (b) can be detected from a structure with only one absorber and one mechanical barrier (a) and a structure with two absorbers and no mechanical barriers (c). Both structures have been irradiated by light in layer 0, with fluence, Q_0 and in the short-pulse regime. In (a) and (c), the acoustic impedance mismatch, $\hat{Z}$, between the layers is shown in blue and the heating function, $h(z)$, across the structure is shown in black. In (b), the acoustic signal detected from the single-absorber structure is shown in black (solid) and the signal from the two-absorber structure is shown in red (dashed).

Therefore, the acoustic signal detected in layer 3, shown in Fig. 5.1b in black

(solid), has one pulse due to the unreflected right-travelling component and a second pulse, which arrives a time d/c_1 later, with an amplitude attenuated by $r_{10}(= 0.6)$. The two pulses have the same width, T_p, dictated by the acoustic relaxation time. Because the light irradiating the absorber from left is in the short-pulse regime (see Chapter 4, Section 4.1) and the absorber has been assumed to be optically thin ($\alpha d << 1$), the acoustic relaxation time is given by:

$$\tau_{aco} = d/c_2,$$

and hence, the pulse width, $T_p = d/c_2$, where c_2 is the speed of sound in the absorbing layer. (Layers 1, 2, and 3 all have the same acoustic impedance, and thus the same speed of sound, $c_1 = c_2 = c_3$.)

The structure shown in Fig. 5.1c is also irradiated by light from the left but has two acoustic sources (shaded, layers 1 and 3) and no mechanical barriers. Both of the absorbing layers are optically thin but layer 1 has an optical absorption coefficient of $\alpha_1 = 0.6\text{m}^{-1}$ and layer 3 has an optical absorption coefficient of $\alpha_3 = 1\text{m}^{-1}$. The generated acoustic signal has been shown in red (dashed) in Fig. 5.1b, when detected in layer 4. Despite the significant geometric and material differences between the two structures shown in Fig. 5.1a and 5.1c, they produce remarkably similar acoustic signals. The signal generated by the two absorbers (Fig. 5.1c) also consists of two pulses; in this case the first pulse is due to the absorber in layer 3 and the second pulse is due to the absorber in layer 1. The amplitude and width of the first pulse in both profiles are the same because the second source (layer 3) in Fig. 5.1c has the same optical absorption coefficient and thickness as the single source (layer 2) in Fig. 5.1a. The amplitude and width of the second pulse is also the same because the ratio between the optical absorption coefficients, α_1 and α_3, in Fig. 5.1c is the same as the reflection coefficient, r_{10}, in Fig. 5.1a, i.e.

$$\frac{\alpha_1}{\alpha_3} = r_{10}.$$

Finally, the time delay between the first and second pulses are the same in both profiles because in Fig. 5.1a, the thickness of layer 1 is half of the thickness of layer 2 in Fig. 5.1c.

This simple example is a useful design consideration; most previous work has only considered a single absorber and thus, mechanical barriers were used to shape the generated acoustic signal. However, the same signal can be produced using distributed heat sources. Thus, the ability to model structures with many absorbing layers, each

with different optical thickness αd, can increase the number of potential designs for a given photoacoustic application.

Very few attempts to model photoacoustic structures with multiple absorbing layers exist [23, 24]. In the work by Sun et al. [23], a transfer matrix method was used to model a structure with multiple absorbers and mechanical barriers. However, the authors assumed that the absorbing layers were optically thin and thus, when irradiated by light in the short-pulse regime, the heating function, $h(z)$, across the absorbers was always constant. The model derived in Chapter 3 of this work does not assume a uniform heating function. By means of a local light fluence, Q_{q-1}, the attenuation of light has been included in the model and thus, absorbers that are not optically thin can be modelled.

In the following chapter, the effects of the optical thickness, αd, and the local light fluence, Q_{q-1}, on the acoustic signals generated from structures with distributed heat sources have been investigated. The results given by Sun et al [23] have been recreated in order to verify the model derived in this work when multiple absorbers are considered. These results, generated by optically thin absorbers, have then been compared to the signal generated by optically thick absorbing layers ($\alpha d \geq 1$). In **Section 5.1**, the multilayered structures have been modelled without mechanical barriers and in **Section 5.2**, mechanical barriers have been introduced.

5.1 No mechanical barriers

The multilayered structure modelled by Sun et al [23] had five alternating layers of absorbing and transparent material. The absorbing layers all had the same optical absorption coefficient, α, the same thickness, d_a, and the same acoustic impedance, Z_a. The transparent layers between them each had a thickness of d_t and an acoustic impedance of Z_t. When there was no acoustic impedance mismatch between the absorbing and transparent layers ($\hat{Z} = 1$), the speed of sound in every layer was the same. The structure is shown in Fig. 5.2 along with the acoustic impedance mismatch, $\hat{Z} = Z_a/Z_t$, shown in blue.

The effect of the optical thickness of the absorbers on the heating function of the structure has been shown before in Chapter 3, Section 3.4 but has been demonstrated again in Fig. 5.2 in black (and shaded). When irradiated by light (with fluence of Q_0) from the left, the light energy is attenuated as it propagates through the absorbing layers. If the attenuation is assumed to follow Beer's Law of absorption,

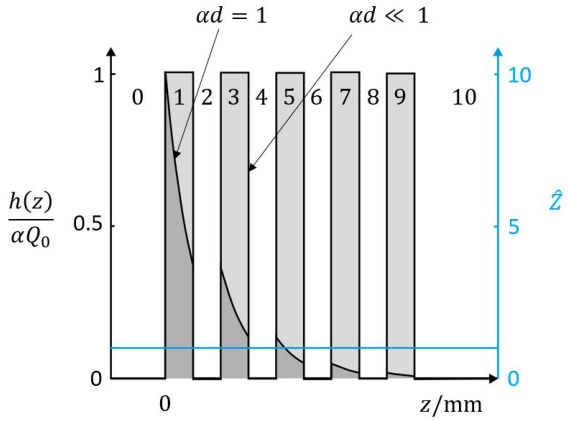


Figure 5.2: Distributed heat sources and no mechanical barriers: a structure with five alternating layers of absorbing (even numbered layers) and transparent material, irradiated by light from the left (with fluence, Q_0, in the short-pulse regime). The acoustic impedance in every layer is the same and so the acoustic impedance mismatch (blue) is always 1. The heating function, $h(z)$, is the shown when the absorbers are optically thin ($\alpha d_a << 1$) and optically thick ($\alpha d_a = 1$), where α and d_a are the optical absorption coefficient and thickness of the absorbing layers.

then absorption profile of the structure is given by

$$A(z) = e^{-\alpha_q z}. \tag{4.1}$$

For optically thin absorbers ($\alpha d << 1$), the heating function is uniform because $e^{-\alpha d} \to 1$ but when the absorbers are optically thick ($\alpha d \geq 1$), observable attenuation occurs. As a result, the generated acoustic signal from optically thin absorbers is different to the signal generated from optically thick absorbers.

In Fig. 5.3, the acoustic signal detected in layer 10 has been shown when the absorbers are optically thin. In order to verify the simulated results from the model with those from Ref. [23], the same normalisation has been used. The normalised time is given by:

$$\hat{t} = \frac{1}{T_p}(t - \frac{d_{ob}}{c_t}), \tag{5.3}$$

where d_{ob} is the distance from the final acoustic source (layer 9) to the detector in layer 10, c_t is the speed of sound in layer 10, and T_p is the generated acoustic pulse width, as defined by the short- and long-pulse regime. In the following work, $d_{ob} = d_t$.

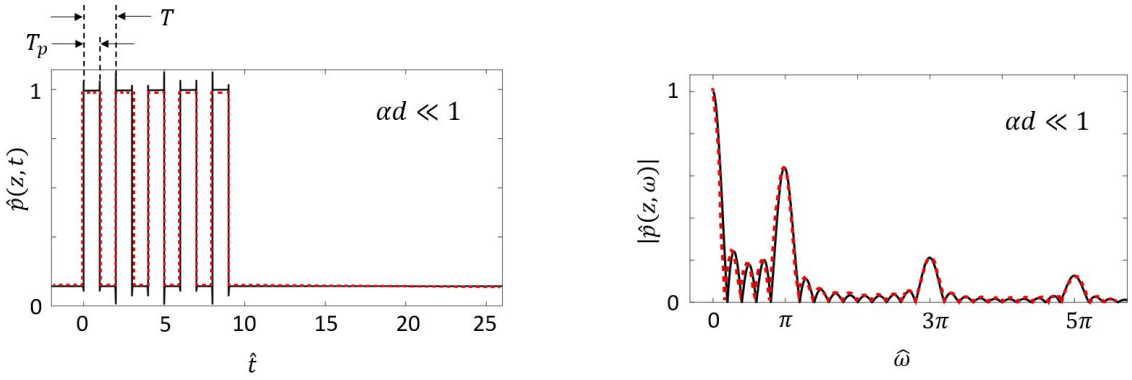
The normalised frequency is given by:

$$\hat{\omega} = \omega T_p, \tag{5.4}$$

and the acoustic signal in the time and frequency domain has been normalised by the maximum amplitude in each profile, i.e,

$$\hat{p}(z,t) = \frac{p(z,t)}{\max(p(z,t))} \tag{5.5}$$

$$\hat{p}(z,\omega) = \frac{p(z,\omega)}{\max(p(z,\omega))} \tag{5.6}$$



(a) (b)

Figure 5.3: Optically thin absorbers: the normalised acoustic signal is shown as a function of normalised (a) time and (b) frequency when the structure in Fig. 5.2 has optically thin absorbers. The black (solid) lines show the results simulated by the model from Chapter 3 and the red (dashed) lines show Sun et al's work [23].

After normalisation, the results from the model (shown in black) show good agreement with the results from Ref. [23], shown in red (dashed). However, note that in the time domain, the profile produced by the model (black-solid) contains some small oscillations, or ringing, due to the numeric inverse Fourier transform used (Sec. 3.5).

The temporal profile in Fig. 5.3a is comprised of five identical and equally-spaced rectangular pulses, corresponding to each of the five sources. In the short-pulse regime, each source generates a pulse with width, T_p equal to the acoustic relaxation time, τ_{aco} and because the absorbers are optically thin, $\tau_{aco} = d_a/c_a$, and hence,

$$T_p = d_a/c_a$$

Each pulse is separated from the next pulse by a time delay of d_t/c_t, corresponding to the sonic transit time across the transparent layers. Thus, the period of the signal in Fig. 5.3a is $T = T_p + d_t/c_t$. When the sonic transit time across each layer is the same, i.e.,

$$\frac{d_a}{c_a} = \frac{d_t}{c_t},$$

then the period becomes $T = 2T_p$.

In the corresponding frequency spectrum in Fig. 5.3b, resonant peaks appear when the normalised frequency, $\hat{\omega}$, is an odd integer value of π. In Chapter 4, Section 4.1, the Fourier transform of a single rectangular pulse was given (Eq. 4.10) and the acoustic signal in the frequency domain was a sinc function which decayed with ωT_p. For the train of five rectangular pulses shown in Fig. 5.3a, the Fourier transform pair has been derived (Appendix A.2). In normalised time, the sum of five shifted rectangular pulses can be expressed as:

$$\Pi_5(\hat{t}) = \Pi(\hat{t} - 1/2) + \Pi(\hat{t} - 5/2) + \Pi(\hat{t} - 9/2) + \Pi(\hat{t} - 13/2) + \Pi(\hat{t} - 17/2), \quad (5.7)$$

and in the normalised frequency domain, the transform of Eq. 5.7 is given by:

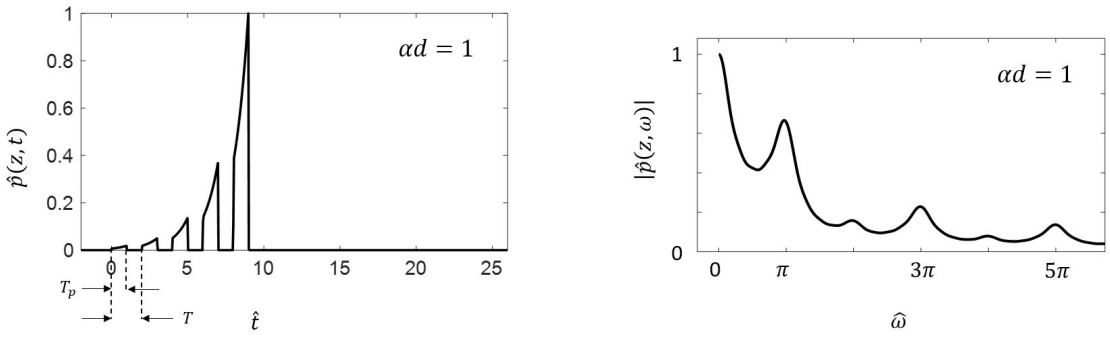
$$\hat{\Pi}_5(\omega) = p_{max} T_p e^{-i\frac{3}{2}\hat{\omega}} \left(e^{-i4\hat{\omega}} \frac{\sin(5\hat{\omega})}{\sin(\hat{\omega})} \right) \frac{\sin(\hat{\omega}/2)}{\hat{\omega}/2}. \quad (5.8)$$

Thus, as with the single acoustic source, there are large peaks in the frequency spectrum at odd integer values of π (where $|\sin\frac{\hat{\omega}}{2}| = 1$) and zeros at even integer values of π (where $|\sin\frac{\hat{\omega}}{2}| = 0$). However, the effect of five pulses, rather than just one, in the time domain is to introduce smaller peaks in the frequency domain, at odd integer values of $\pi/10$, and zeros at integer values of $\pi/5$, excluding those divisible by five. The magnitude of all these peaks decays with $\hat{\omega}$.

The model derived in Chapter 3 also has the capability of simulating structures with optically thick absorbers, that attenuate light as it propagates through the layers. In Chapter 3 (Eq. 3.36), the spatial heating function of the qth layer was defined as:

$$h(z) = \alpha_q Q_{q-1} A(z), \quad (3.36)$$

where α_q was the optical absorption coefficient of the qth layer, Q_{q-1} was the local light fluence irradiating the layer (see Fig. 3.6), and $A(z)$ was the optical absorption profile. The effect of the optically thick absorbers on the heating function, $h(z)$, has been shown in Fig. 5.2 when the absorption profile of the structure (and thus, local light fluence, Q_{q-1}) follows Beer's law. In Fig. 5.4, the effect of optically thick absorbers on the generated acoustic signal has been demonstrated and can be compared to the acoustic signal generated from optically thin absorbers.



(a) (b)

Figure 5.4: Optically thick absorbers: the normalised acoustic signal is shown as a function of normalised (a) time and (b) frequency when the five absorbing layers in the structure in Fig. 5.2 have an optical thickness of 1 and an absorption profile that decays according to Beer's Law.

The five acoustic sources each generate a pulse, which when detected in layer 10, arrive at equally-spaced intervals of time and with equal pulse width, T_p, shown in Fig. 5.4a. However, unlike the optically thin absorbers, the optically thick absorbers generate pulses with non-constant amplitude. As discussed in Chapter 4 for a single, optically-thick acoustic source, the generated pulse shape mirrors the absorption profile, and for a structure with five absorbers, less light irradiates the absorber in layer 9 than the absorber in layer 1, closest to the light source. The pulse originating from layer 9 has a smaller amplitude compared to that originating from layer 1. Hence, the shape of the temporal profile increases exponentially as signals from acoustic sources closer to the light source (in layer 0) arrive at the detector in layer 10.

The corresponding frequency spectrum, shown in Fig. 5.4b, shares some similarities with frequency spectrum from the optically thin absorbers in Fig. 5.3b. There are resonant peaks at odd integer values of π, which decrease in magnitude. However, the side lobes observed in Fig. 5.3b at odd integer values of $\pi/5$ have disappeared and there are now additional peaks at even integer values of π. Thus, once again, an analytical expression for the Fourier transform of the five exponential pulses found in Fig. 5.4a has been derived (Appendix A.3) in order to understand the spectrum in Fig. 5.4b.

In normalised time, the train of five exponential pulses can be expressed as:

$$f_5(\hat{t}) = e^{+\alpha d_a(\hat{t}+\hat{t_0})}\Bigg(\Pi(\hat{t}-1/2) + e^{+\alpha d_a}\Pi(\hat{t}-5/2) + e^{+2\alpha d_a}\Pi(\hat{t}-9/2) + e^{+3\alpha d_a}\Pi(\hat{t}-13/2) + e^{+4\alpha d_a}\Pi(\hat{t}-17/2)\Bigg), \quad (5.9)$$

where, $\hat{t_0} = t_0/T_p$, and the corresponding Fourier transform, in normalised frequency, is given by:

$$F(\hat{\omega}) = e^{-i(4\hat{\omega}-i\frac{5\alpha d_a}{2})}e^{-i\hat{\omega}(\frac{3}{2}-\hat{t}_0)}\frac{\sin\left(\frac{1}{2}(\hat{\omega}+i\alpha d_a)\right)}{\frac{1}{2}(\hat{\omega}+i\alpha d_a)}\frac{\sin(5(\hat{\omega}+i\frac{\alpha d_a}{2}))}{\sin(\hat{\omega}+i\frac{\alpha d_a}{2})}. \quad (5.10)$$

Thus, like for the single exponential pulse (Eq. 4.11), the effect of optically thick absorbers, is to introduce additional imaginary component in the sine terms, which remove any zeros in the frequency spectrum at even integer values of π and having several exponential pulses, rather than just one, removes any side lobes.

When αd_a is very small, then Eqs. 5.9 and 5.10 simplify back into the Fourier transform pair for $\hat{\Pi}_5$ (Eqs. 5.7 and 5.8).

In this way, structures that attenuate the irradiating light as it propagates through any absorbing layers generate acoustic signals that are different from the uniform acoustic signals generated from optically thin absorbers. In this section, the model formulated in Chapter 3 has been used to simulate the generated acoustic signal from structures with more than one absorbing layer but with no mechanical barriers and it can be concluded that:

- a (finite) pulse train was generated in the time domain of the acoustic signal by irradiating a structure with several absorbing layers and no mechanical barriers. If a photoacoustic structure had only one absorbing layer, a pulse train could only be detected if there were mechanical barriers, and hence, reflections.

- the inclusion of distributed heat sources in the model was verified by comparing the model's results with results derived by Sun et al [23] and good agreement was shown.

- unlike the work by Sun et al [23], the model formulated in this work does not limit the optical thickness of the absorbing layers. The heating function can be non-constant and an example was given when the heating function decayed with Beer's Law. The effect of optically thick absorbers on the generated acoustic

signal was compared to the optically thin absorbers used by Sun et al [23] and any differences were explained by deriving the analytical expressions for the pulse trains, in the time and frequency domains.

5.2 Mechanical barriers

In the previous section, the multilayered structures modelled had distributed heat sources but no mechanical barriers; all of the layers had the same acoustic impedance ($\hat{Z} = 1$). In the following section, impedance mismatches have been introduced between the absorbing and transparent layers.

In Chapter 4, the addition of mechanical barriers to a structure with just a single acoustic source resulted in infinite reflections (Fig. 4.11) and the attenuation of the reflected and transmitted components was given by the reflection and transmission coefficients, where, for a wave travelling from medium 1 to 0,

$$r_{10} = \frac{1 - \hat{Z}}{1 + \hat{Z}}, \tag{5.1}$$

and

$$t_{10} = \frac{2}{1 + \hat{Z}}, \tag{5.2}$$

respectively, where $\hat{Z} = Z_1/Z_0$.

When the acoustic impedance mismatch was greater than 1 ($\hat{Z} > 1$), the temporal profile (Fig 4.11c) detected in the right substrate oscillated between positive and negative pressure with a period of $2T_p$, where T_p was the pulse width of the generated acoustic signal. As a result, there were resonant peaks in the corresponding frequency spectrum (Fig 4.11e) when ω was an odd integer of π/T_p.

However, in Section 5.1, it was shown that a structure with more than one acoustic source produced resonant peaks in the frequency spectrum at odd integer values of π/T_p ($\hat{\omega} = \pi$) even when there were no mechanical barriers present. In this section, all the acoustic sources have the same acoustic impedance, Z_a, but the transparent layers between the absorbing layers have an acoustic impedance, Z_t. Thus, the acoustic impedance mismatch between the layers is:

$$\hat{Z} = \frac{Z_a}{Z_t} \neq 1. \tag{5.11}$$

Mechanical barriers were considered in Sun et al's work [23] on optically thin distributed heat sources and so, once again, the results from the model formulated in Chapter 3 can be verified. For example, consider the structure in Fig. 5.5a, which has two optically thin absorbing layers (the heating function, shown in black, is uniform across layers 1 and 3) and the acoustic impedance mismatch between the absorbers and the surrounding layers is $\hat{Z} = 10$ (shown in blue). The acoustic signal detected in layer 4 has been shown in the time and frequency domain in Fig. 5.5b and 5.5c, respectively, where, once again, for the purpose of verification, the normalisation from Ref. [23] has been used (see Eqs. 5.3 and 5.4). There is good agreement between the profiles simulated by the model shown in black (solid) and the results from Sun et al. [23] shown in red (dashed) in both domains. In the temporal domain, ringing in the simulated profile (black) has been produced as a result of taking the numeric inverse Fourier transform (Chapter 3).

In Fig. 5.5c, the frequency spectrum is dominated by a resonant peak at $\hat{\omega} = \pi$. Like in Section 5.1, the structure has been irradiated by light in the short-pulse regime ($\tau_p << \tau_{aco}$) and so the acoustic pulse width, T_p, is equal to the acoustic relaxation time. For optically thin absorbers ($\alpha d << 1$), this means that:

$$T_p = \tau_{aco} = \frac{d_a}{c_a}, \tag{5.12}$$

where d_a and c_a are the thickness and speed of sound in the absorbing layer. Thus, the acoustic pulse width is equal to the sonic transit time across the absorbing layer (in this example, $T_p = d_a/c_a = 0.2\mu$s). If the sonic transit time across the absorbing layers is equal to the sonic transit time across the transparent layers, i.e.,

$$\frac{d_a}{c_a} = \frac{d_t}{c_t}, \tag{5.13}$$

then the time delay between the two generated pulses and their subsequent echoes is equal to the acoustic pulse width, T_p, and the temporal profile generated by the two absorbers (Fig. 5.5b) oscillates between positive and negative pressure with a period of $2T_p$. Hence, just like the single absorber with mechanical barriers in Chapter 4, in Fig. 5.5c the resonant peaks at odd integer values of π ($\omega = \pi/T_p = 150$MPa) are as a result of this oscillation.

However, unlike the spectra in Chapter 4 (and Section 5.1), the spectrum in Fig. 5.5c has a small peak at $\hat{\omega} = 0.13\pi$, before the first resonant peak, and a low frequency oscillation in the temporal profile (Fig. 5.5b) can be seen. In the work by Sun et al [23], this phenomenon was explained by comparing the two absorbers, separated

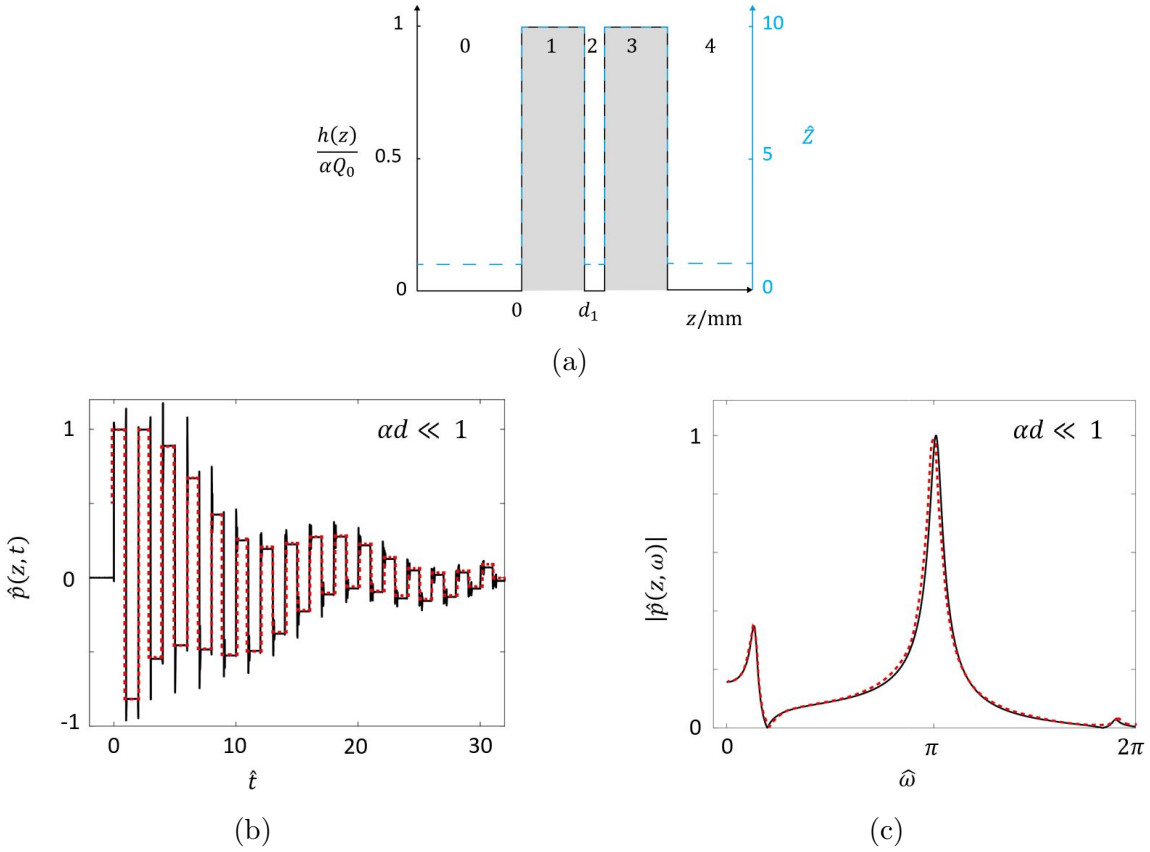


Figure 5.5: Distributed heat sources with mechanical barriers: in (a) two optically thin absorbing layers ($\alpha d_a << 1$) have been separated by a transparent layer, where the acoustic impedance mismatch, $\hat{Z}$, between absorbing (layers 1 and 3) and transparent layers (layers 0, 2, and 4) is 10. In both the normalised (b) time and (c) frequency domain, agreement between the results from the model, shown in black (solid), and the results from Sun et al. [23], shown in red (dashed), is good - ringing in the temporal profile from the model is as a result of using the numeric inverse Fourier Transform. In the temporal domain, the oscillation between positive and negative pressure, due to reflections, results in a resonant peak at odd integer values of π in the frequency spectrum. The temporal profile also oscillates at a lower frequency, $\delta\hat{\omega}$, whose value can be found from the spectrum in (c). (For normalisation procedure, see Eqs. 5.3 and 5.4.)

by a transparent layer, to masses on a spring, with the transparent layer providing the restoring force. Hooke's law was used to approximate the oscillation frequency of the absorbers and the authors showed that, as the acoustic impedance mismatch increased, the approximated oscillation frequency decreased.

The same low frequency oscillation generated by two optically thin absorbers can also be seen in the simulated profiles of a structure with optically thick absorbing layers. In Fig. 5.6a, the two absorbing layers (layers 1 and 3) have an optical thickness

equal to 1 ($\alpha d_a = 1$) and an absorption profile that follows Beer's Law. Therefore, the heating function (shown in black and shaded) decays exponentially as light, propagating from the left, is attenuated. The acoustic impedance mismatch is still 10 (shown in blue) and the sonic transit time in the absorbing layers is the same as in the transparent layers. The acoustic signal detected in layer 4 has been shown as a function of normalised time and frequency in Figs. 5.6b and 5.6c, respectively.

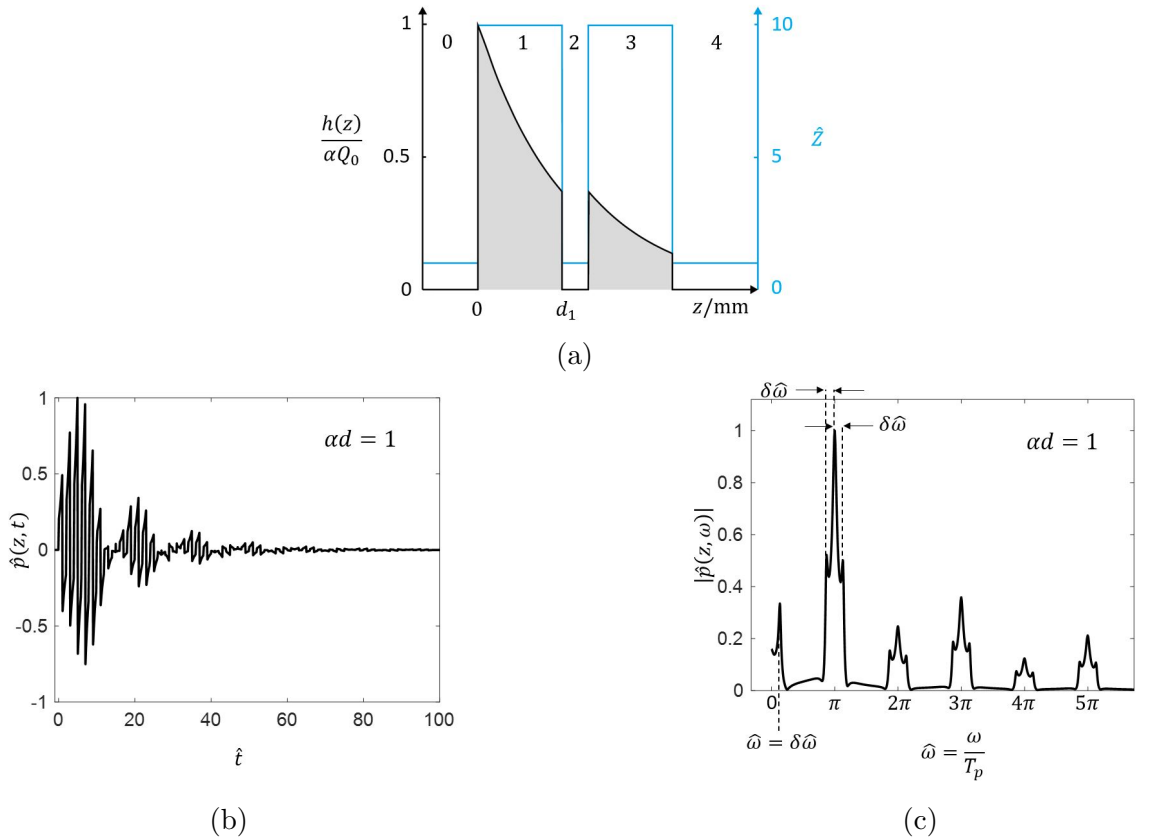


Figure 5.6: Optically thick absorbers with mechanical barriers: when $\alpha d_a = 1$, the attenuation of light propagating from the left has been assumed to follow Beer's Law, and thus the heating function decays exponentially (Eq. 3.36 and 4.1). The shape of the pulses in the temporal domain (b) mirrors that of the heating function and so are no longer rectangular. As a result, the frequency spectrum in (c) has resonant peaks at odd and even integer values of π. A low-frequency peak appears $\delta\hat{\omega} = 0.13\pi$ and also at $n\pi \pm \delta\hat{\omega}$, where n is an integer.

When $\alpha d_a = 1$, the acoustic pulse width is still equal to:

$$T_p = \frac{d_a}{c_a}\left(= \frac{d_t}{c_t}\right),$$

and so the temporal profile in Fig. 5.6b oscillates between positive and negative pressure (with period of $2T_p$) and resonant peaks appear at odd integer values of π

in the frequency spectrum (Fig. 5.6c). However, like in Section 5.1 (Eqs. 5.9 and 5.10), the rectangular shape of the pulses in the temporal profile has been lost and so, the optically thick absorbers also produce resonant peaks at even integer values of π. However, with mechanical barriers, the resonant peaks are wider and have distinct 'shoulders', located at $n\pi \pm \delta\hat{\omega}$, where n is any integer and $\delta\hat{\omega}$ is the same as in low-frequency oscillation found in Fig. 5.5, i.e. $\delta\hat{\omega} = 0.13\pi$. Thus, $\delta\hat{\omega}$ does not depend on the optical thickness of the acoustic sources.

Finally, the number of absorbing layers has been increased from two to five. In Section 5.1, even without mechanical barriers, five absorbing layers, separated by five transparent layers, produced resonant peaks at odd integer values of π, when the absorbing layers were optically thin, and at odd and even integer values of π, when the absorbing layers were optically thick.

The effect of the acoustic impedance mismatch, $\hat{Z}$, between the absorbing and transparent layers has been explored in Fig. 5.7 for both optically thin and thick absorbers when $\hat{Z} < 1$ (so reflections are always positive) and when $\hat{Z} > 1$ (reflections result in inversion).

In Figs. 5.7a and 5.7c, the acoustic impedance mismatch is $\hat{Z} = 0.2$. In (a), the multilayer structure is shown along with the heating function (shaded) and acoustic impedance mismatch (blue). When the absorbing layers (odd-numbered layers) are optically thin, the heating function is constant. When optically thick absorbers ($\alpha d = 1$) are irradiated by light from the left, the attenuation of light has been assumed to follow Beer's law and so the heating function decays exponentially. In Fig. 5.7c, the acoustic signal detected in layer 10 is shown in red (dashed) when $\alpha d << 1$ and in black (solid) when $\alpha d = 1$. When the acoustic impedance mismatch is increased to $\hat{Z} = 2$, the irradiated structure and corresponding signal detected in layer 10 is shown in Figs. 5.7b and 5.7d, respectively.

As expected, in both spectra in Figs. 5.7c and 5.7d, the optically thin absorbers produce resonant peaks at odd integer values of π, with side lobes between the peaks and zeros at even integer values of π. However, unlike the spectrum produced with no mechanical barriers (Fig. 5.3b), when $\hat{Z} < 1$, the shape of the resonant peaks in Fig. 5.7c is less rounded and, as the frequency increases, the amplitude of the peaks decay much faster. The amplitude of the side lobes between them has also decreased. When $\hat{Z} > 1$, in Fig. 5.7d, the resonant peaks are even sharper and, rather than decaying with frequency, the amplitude of the first resonant peak is about 25% greater than the zero-frequency peak. Such differences can be observed in work by Sun et al. in Ref. [23].

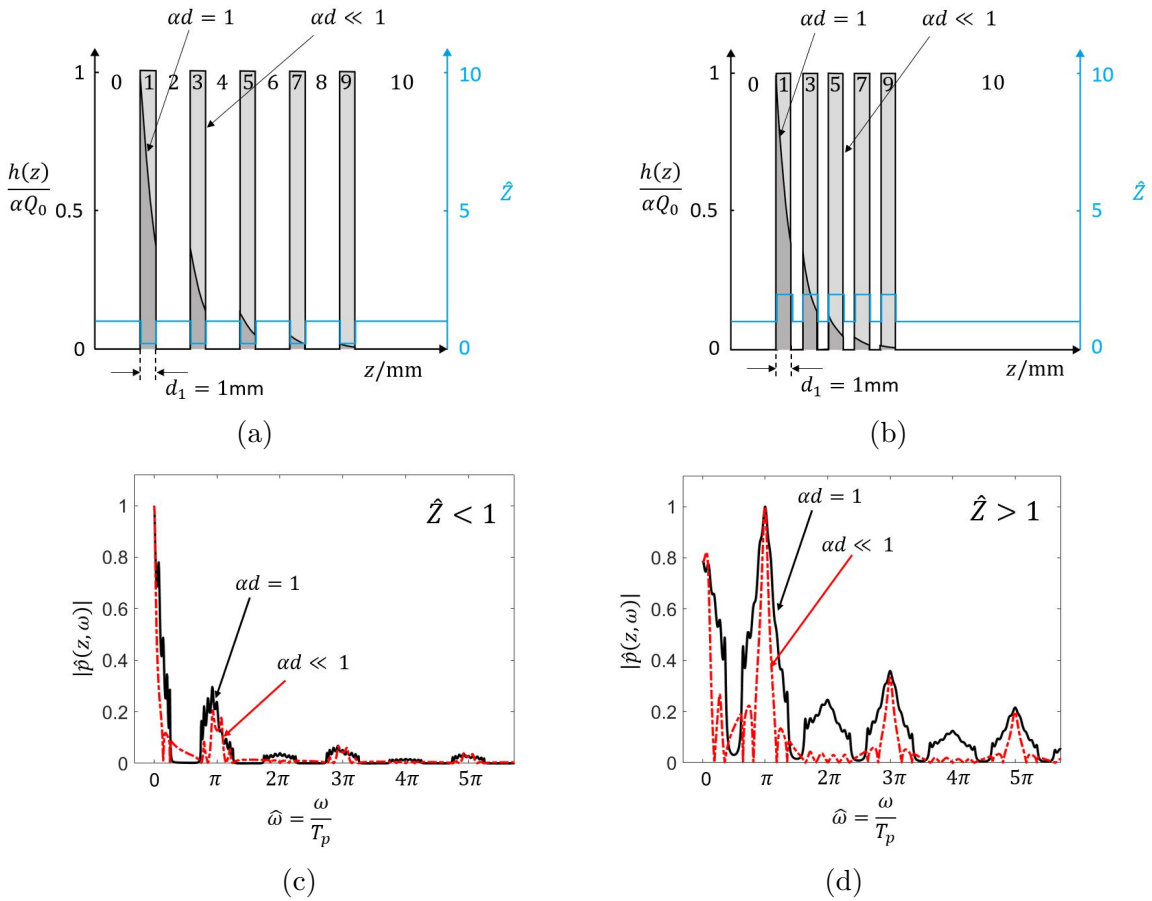


Figure 5.7: Low (left panel) vs. high (right panel) acoustic impedance mismatch: in the structure in (a) the acoustic impedance mismatch is $\hat{Z} = 0.2$ and the resultant frequency spectrum, detected in layer 10, has been simulated in (c) when $\alpha d << 1$ in red, dashed and when $\alpha d = 1$ in black, solid. When $\hat{Z} = 2$, the structure and corresponding frequency spectrum, detected in layer 10, have been shown in (b) and (d), respectively. In both structures, the sonic transit time is the same in every layer ($= 0.2\mu$s) and equal to the acoustic pulse width, T_p.

Now, however, using the model formulated in Chapter 3, the effect of $\hat{Z}$ on optically thick absorbers can be observed. In Figs. 5.7c and 5.7d, the signal generated by optically-thick absorbers (shown in black) has much wider resonant peaks, at both odd and even integer values of π, and as a result, there are no side lobes in either spectra. Instead, there are distinct regions, referred to as stop-bands, where the magnitude of the signal in the frequency spectrum is zero or very low. The width of these stop-bands is greater and the roll-off, or gradient, of the stop-band is sharper in Fig. 5.7c where $\hat{Z} < 1$. Furthermore, compared to the spectrum from just two absorbers, the single low frequency peak seen at 0.13π in Fig. 5.6c has now been replaced with several low frequency peaks and the resonant peaks, have not just one 'shoulder', but

several subsidiary peaks on either side.

In the next chapter, rather than approximate the position of the low frequency peak (seen in Figs. 5.5c and 5.6c) using Hooke's law as was done by Sun et al [23], the relationship between the acoustic impedance mismatch and position and amplitude of these low frequency and subsidiary peaks will be derived.

However, before concluding, recall that the structures used in this chapter have had an equal sonic transit time in every layer, i.e., $d_a/c_a = d_t/c_t$ and have been irradiated from the left by light in the short-pulse regime ($\tau_p << \tau_{aco}$). When $\alpha d << 1$ and when $\alpha d = 1$, the acoustic relaxation time (Eq. 4.2) is equal to the sonic transit time across the absorber and thus,

$$T_p = \tau_{aco} = \frac{d_a}{c_a} = \frac{d_t}{c_t}. \tag{5.14}$$

In other words, the acoustic wavelength, cT_p, is equal to the thickness of the layers and the structure can be considered as subwavelength.

Furthermore, if the acoustic impedance mismatch does not equal 1, e.g.,

$$\hat{Z} = \frac{Z_a}{Z_t} = 10 \tag{5.15}$$

then, it has been assumed that both the density and speed of sound in the absorbing layers increase by the same amount, i.e., from Eq. 5.15, $Z_a = 10Z_t$ and so:

$$\rho_a c_a = (\sqrt{10}\rho_t)(\sqrt{10}c_t). \tag{5.16}$$

Hence, in order to maintain constant sonic transit time, i.e.,

$$\frac{d_a}{c_a} = \frac{d_t}{c_t}, \tag{5.17}$$

the thickness of the transparent layers must decrease:

$$\frac{d_a}{\sqrt{10}} = d_t. \tag{5.18}$$

Therefore, even when the acoustic impedance mismatch is not 1, the sonic transit time in every layer is the same and equal to the acoustic pulse width, T_p.

5.3 Summary

In this chapter, photoacoustic structures with more than one absorbing layer have been modelled. The generated acoustic signal, detected in the right-hand substrate,

has been simulated when irradiated from the left-hand side by light in the short pulse regime. Previous attempts to model structures with distributed heat sources were limited to either optically thin absorbing layers ($\alpha d << 1$) [23] or included the effects of heat transport [24].

The model formulated in Chapter 3 is capable of modelling both optically-thin and optically-thick absorbers and so the effect of optical thickness on the generated acoustic signal could be investigated. When the optical absorption profile was assumed to follow Beer's Law, it was found that:

- contrary to optically-thin absorbers, five optically-thick absorbers with no mechanical barriers produce resonant peaks at *all* integer values of π/T_p ($\hat{\omega} = \pi$), not just odd integer values. This is because the temporal profile of the generated pulses is exponential, not rectangular, and thus there are additional cosine terms in the Fourier transform in Eq. 5.10.

- With the addition of mechanical barriers ($\hat{Z} \neq 1$), a low-frequency peak appears before the first resonant peak at the same frequency, $\delta\hat{\omega}$, as with optically thin absorbers. Small 'shoulders' also appear on either side of every resonant peaks, at $n\pi \pm \delta\hat{\omega}$, where $n = 0, 1, 2..$

- Increasing the number of layers results in more subsidiary peaks to either side of the resonant peaks and the suppression of the side lobes produces distinct stop-bands, or regions of low or no signal, in the frequency spectra,

- and the width of these stop-bands increases and the roll-off, or gradient, decreases when the acoustic impedance mismatch is less than one.

The model formulated in Chapter 3 has been verified with the work by Sun et al [23] and showed good agreement. The use of a local light fluence to include the effect of light attenuation in this model has enabled the simulation of the signal generated from a structure with several optically thick absorbers, which, to the author's knowledge, has not been demonstrated before.

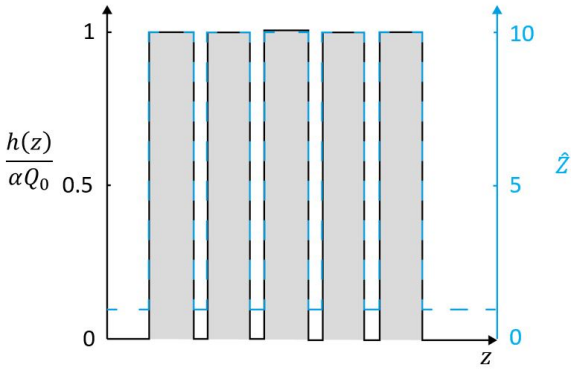


Figure 5.8: The multilayered acoustic structure with five alternating layers of absorber (shaded) and transparent material, which also have high and low acoustic impedance, respectively. The sonic transit time is the same in every layer and so in the short-pulse regime, the generated acoustic pulse has a wavelength, cT_p, equal to the dimensions of the layers.

To conclude, it has been noted that a multilayer structure, comprised of five alternating absorbing and transparent layers with alternating high and low acoustic impedance (Fig. 5.8), will generate an acoustic pulse with a wavelength equal to the dimensions of the layer if all the layers have the same sonic transit time and are irradiated by light in the short-pulse regime. Hence, the low-frequency peak and the distinct stop-bands in the frequency spectra of structures with optically thick absorbers must be interference effects. In Chapter 6, subwavelength photoacoustic structures such as these will be investigated.

Chapter 6

Sub-wavelength photoacoustic structures

In Chapter 5, rather than just one optical absorber, several absorbing layers were included in the photoacoustic structure. It was found that:

- even without mechanical barriers, structures with distributed heat sources produced resonant peaks when the normalised frequency was an odd integer value of $\hat{\omega} = \pi$ ($\omega = \pi/T_p$, where T_p was the pulse width of the generated acoustic signal) if the sonic transit time was the same in every layer, i.e. $d_a/c_a = d_t/c_t$, where the subscripts a and t denote the absorbing and transparent layers, and d and c are the thickness and speed of sound of a layer.

- With the addition of mechanical barriers, low frequency peaks appeared in the detected frequency spectrum. In work by Sun et al. [23], these small peaks were likened to the oscillatory motion of two masses on a spring and Hooke's law was used to approximate the oscillatory frequency.

- When the absorbing layers were no longer optically thin (e.g. when $\alpha d_a = 1$), the low-frequency peak, at $\hat{\omega} = \delta\hat{\omega}$, was present in the detected spectrum but also appeared at $n\pi \pm \delta\hat{\omega}$, as 'shoulders' to either side of the resonant peaks at odd integer values of $\hat{\omega} = \pi$.

The spectra exhibited interference effects due to the subwavelength properties of the structure. When irradiated by light in the short-pulse regime, the generated acoustic signal had a wavelength, cT_p, equal to the dimensions of the absorbing layers,

$$c_a T_p = d_a.$$

When both the absorbing and transparent layers had the same sonic transit time, the generated acoustic signals (and the reflections when mechanical barriers were present) interfered with each other.

In this chapter, the frequency-selective characteristics of acoustic subwavelength structures will be explored. Because the governing photoacoustic equation was solved in the frequency domain in the formulations in Chapter 3, the model is particularly well-suited for the following investigations. First,

- analogous to optics, the theory of interference effects in subwavelength acoustic structures will be discussed and examples of anti-reflection coatings, and in particular symmetric multilayers, will be given.
- Then, high-reflectance coatings will be introduced and their behaviour, along with that of symmetric multilayers, will be used to derive the low-frequency peak at $\delta\hat{\omega}$ in the frequency spectrum from the two-absorber structure from Chapter 5 (Fig. 5.5).
- Finally, high-reflectance coatings will be used to improve the emission efficiency of photoacoustic structures, i.e., rather than generating left- and right-travelling signals of equal amplitude, the amplitude of the signal to one side will be maximised.

6.1 Anti-reflection coatings

In Chapter 3, the reflection and transmission coefficients for an acoustic signal travelling from layer 0 to layer 1 were derived as:

$$r_{01} = -\frac{\left(Z_0 - Z_1\right)}{\left(Z_0 + Z_1\right)}, \tag{3.13}$$

$$t_{01} = \frac{2Z_1}{Z_0 + Z_1} \tag{3.16}$$

respectively, and the acoustic signal before and after collision at the copper-water interface was shown (Fig. 3.5). The reflectance and transmittance, which are ratios of intensity, were also derived and it was found that: $R_{01} = |r_{01}|^2$ and $T_{01} = \frac{Z_0}{Z_1}|t_{01}|^2$. For a single interface, the reflectance was constant for all frequencies.

However, in Chapter 4, it was shown that when two mechanical barriers surrounded an acoustic source, the generated acoustic signal bounced back and forth

between the two interfaces (Fig. 4.10). With every bounce, reflection and transmission occurred and the amplitude and phase of each component was altered, such that transmitted components arrived at a detector in the substrate with an attenuated amplitude and phase shifted by an amount associated with the thickness of the layer (Eq. 4.17). In other words, contrary to a single interface, the reflection and transmission coefficients, and reflectance and transmittance, were frequency-dependent.

An anti-reflection coating is designed such that these phase-shifted transmitted components all arrive at the detector in phase and so constructively interfere. Conversely, reflected components arrive out of phase and cancel each other out. Anti-reflection coatings have been deployed to great effect in optical applications, where a reduction in surface reflections is required [35]. However, the acoustic analogy and its application in the control of photoacoustic signals has been less widely researched [23, 83]. In a study by Lee et al. [76], a matching layer, with the same acoustic properties as the photoacoustic source, was used to control the cancellation effect between the unreflected and reflected acoustic signals. Similarly, in Rajagopal and Cox's study [15], different backing materials were used to reverse the polarity of the reflected signal and hence induce cancellation of the unreflected acoustic signal. Such control of the reflected acoustic signal is essential in applications that require high-amplitude photoacoustic signals, such as photoacoustic imaging [91–94] and cavitation therapies [5, 90].

In this section, several coating designs will be considered and the reflectance as a function of frequency will be modelled. To begin with, the anti-reflection coatings will be irradiated by an external acoustic source in layer 0. As described in Chapter 3, in order to model this the source terms in the transfer-matrix model will all be zero and the right-travelling coefficient in layer 0 will be non-zero ($A_0 \neq 0$). Then, photoacoustic sources will added to the structure.

6.1.1 Quarter-wave plates

The simplest anti-reflection coating is a quarter-wave plate. Consider the structure in Fig. 6.1. When an external acoustic source irradiates the structure from the left, the path of reflected and transmitted components are shown in grey. Reflected components in layer 0 will destructively interfere if they are out of phase with each other. The phase of each reflected component depends on (1) the phase shift at each interface due to reflection and (2) the phase shift associated with the thickness of layer 1. The phase change due to reflection depends on the sign of each reflection coefficient, i.e., r_{01} and r_{12}:

- a negative reflection coefficient results in a π phase change,
- a positive reflection coefficient results in no phase change.

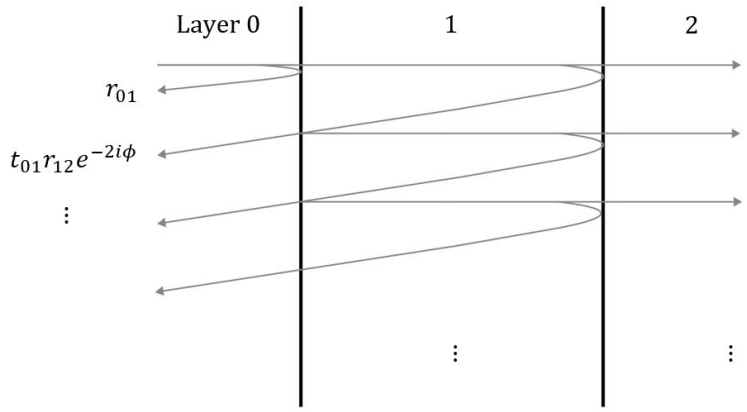


Figure 6.1: Out of phase reflections: when the structure is irradiated by sound from the left, reflected components (grey) arriving in layer 0 will destructively interfere if they are out of phase with each other. The phase of these components depends on the phase thickness of layer 1, ϕ, and the polarity of the reflection coefficients, r_{01} and r_{12}.

The phase shift across the thickness of layer 1 is defined as:

$$\phi = k_1 d_1 \tag{6.1}$$

where $k_1 = \frac{\omega}{c_1}$ and d_1 is the layer thickness. At $\omega = \frac{2\pi}{\lambda_0}$, if layer 1 has a thickness equal to one-quarter of the target wavelength, λ_0, then the phase thickness of the layer is

$$\phi = k_1 d_1 = \frac{2\pi}{\lambda}\frac{\lambda_0}{4} = \frac{\pi}{2}, \tag{6.2}$$

and thus, the phase difference between reflected components in layer 0 is π and they are out of phase. However, total cancellation will only occur if the magnitude of the reflected components sum to zero, i.e., when the reflectance is zero. In Section 3.2, the reflection coefficient, r_{01}, for a single interface at $z = 0$ was derived using the transfer matrix method. An expression for B_0/A_0 was found from:

$$\begin{pmatrix} A_1 \\ B_1 \end{pmatrix} = \frac{\rho_1}{2ik_1}\begin{bmatrix} \frac{ik_1}{\rho_1} + \frac{ik_0}{\rho_0} & \frac{ik_1}{\rho_1} - \frac{ik_0}{\rho_0} \\ \frac{ik_1}{\rho_1} - \frac{ik_0}{\rho_0} & \frac{ik_1}{\rho_1} + \frac{ik_0}{\rho_0} \end{bmatrix}\begin{pmatrix} A_0 \\ B_0 \end{pmatrix}. \tag{3.10}$$

and then the reflectance was given as $R = |r_{01}|^2$. For a single layer (1), sandwiched between two substrates (layers 0 and 2), an expression for B_0/A_0 can be similarly derived from Eq. 3.8 when irradiated by an external acoustic source:

$$\begin{pmatrix} A_2 \\ B_2 \end{pmatrix} = [T_1]\begin{pmatrix} A_0 \\ B_0 \end{pmatrix}, \tag{6.3}$$

where ,

$$[T_1] = [M_2]^{-1}|_{z_1}[M_1]|_{z_1}[M_1]^{-1}|_{z_0}[M_0]|_{z_0} = \begin{bmatrix} m_{11} & m_{12} \\ m_{21} & m_{22} \end{bmatrix}, \tag{6.4}$$

and

$$[M_2]^{-1}|_{z_1} = \frac{\rho_2}{2ik_2}\begin{bmatrix} \frac{ik_2}{\rho_2}e^{+ik_2z_1} & -e^{+ik_2z_1} \\ \frac{ik_2}{\rho_2}e^{-ik_2z_1} & e^{-ik_2z_1} \end{bmatrix}, \tag{6.5}$$

$$[M_1]|_{z_1}[M_1]^{-1}|_{z_0} = \begin{bmatrix} \cos\phi & \frac{Z_1}{\omega}\sin\phi \\ -\frac{\omega}{Z_1}\sin\phi & \cos\phi \end{bmatrix}, \tag{6.6}$$

$$[M_0]|_{z_0} = \begin{bmatrix} e^{-ik_0z_0} & e^{+ik_0z_0} \\ -\frac{ik_0}{\rho_0}e^{-ik_0z_0} & \frac{ik_0}{\rho_0}e^{+ik_0z_0} \end{bmatrix}, \tag{6.7}$$

and $\phi = k_1(z_1 - z_0)$ and $Z_1 = \rho_1 c_1$ are the phase thickness and acoustic impedance of layer 1, respectively. Recall that when sound is incident from the left, there are no acoustic waves entering the structure from the semi-infinite substrate on the right-hand side, i.e., $B_2 = 0$ and hence, from Eq. 6.3,

$$0 = m_{21}A_0 + m_{22}B_0,$$

which, after rearranging, can be written as,

$$r = \frac{B_0}{A_0} = -\frac{m_{21}}{m_{22}} = -\frac{\left(1 + \frac{Z_2}{Z_0}\right)\cos\phi - i\left(\frac{Z_1}{Z_0} + \frac{Z_2}{Z_1}\right)\sin\phi}{\left(1 - \frac{Z_2}{Z_0}\right)\cos\phi + i\left(\frac{Z_1}{Z_0} - \frac{Z_2}{Z_1}\right)\sin\phi}, \tag{6.8}$$

where $z_0 = 0$. In this example, layer 1 is a quarter-wave plate and so the phase thickness is $\phi = \pi/2$ and the cosine terms in Eq. 6.8 disappear. Then, by setting Eq. 6.8 equal to zero, i.e. $B_0/A_0 = 0$, the condition for zero reflectance can be found:

$$Z_1^2 = Z_2 Z_0. \tag{6.9}$$

For example, for the copper-water interface from Chapter 3, an anti-reflection coating will have zero reflectance at a target frequency, f_0, when the acoustic impedance, Z_1, and thickness, d_1, are given by:

$$Z_1 = \sqrt{Z_{Cu}Z_w} \quad \text{and} \quad d_1 = \frac{\lambda_0}{4} = \frac{1}{4}\frac{c_1}{f_0},$$

respectively.

Layer No.	Material	Z $\times 10^6$/ kg m^{-2} s^{-1}	d/λ_0
0	Copper	40.7	-
1	AR	7.8	0.25
S	Water	1.5	-

Table 6.1: Layer materials and properties of an anti-reflection (AR) coating at a copper-water interface

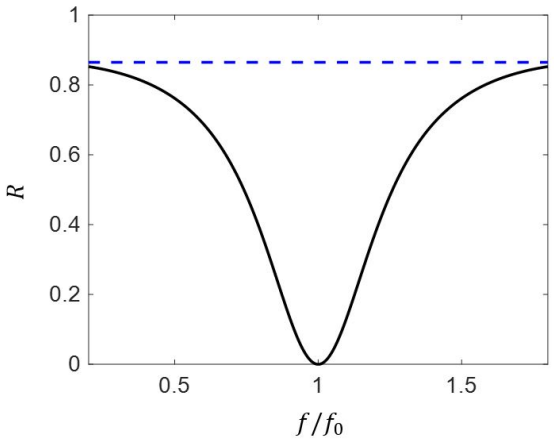
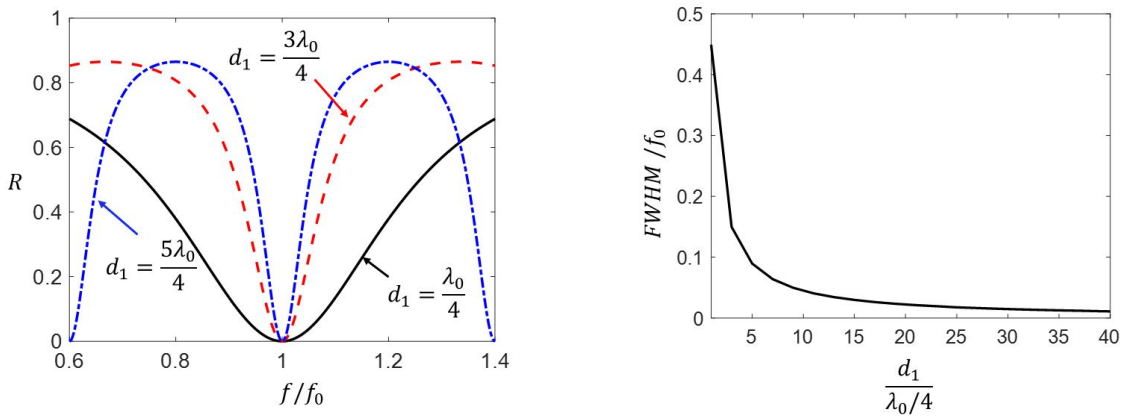


Figure 6.2: Zero reflectance: an anti-reflection coating has zero reflectance (black) at a target frequency, f_0, compared to the copper-water interface, which has constant reflectance at all frequencies (blue). In this example, $f_0 = 5$ MHz.

The predicted reflectance (solid, black line) has been shown as a function of frequency in Fig. 6.2 for an anti-reflection coating with the properties shown in Table 6.1 at a target frequency of 5MHz. As designed, the reflectance of the coating drops to zero at the target frequency, compared to the copper-water interface which has a constant reflectance at all frequencies (dashed, blue line). However, the reflectance of the anti-reflection coating is also zero at every odd integer value of f_0 because, at these frequencies, the phase thickness of layer 1 is an odd integer value of $\pi/2$ and so destructive interference still occurs. In contrast, at even integer values of f_0, the reflectance is at a maximum because the thickness of layer 1 is a half-wavelength and acts as an absentee layer.

Furthermore, if the thickness of layer 1, d_1, is no longer a quarter-wavelength but is some odd integer value of quarter-wavelengths, then zero reflectance still occurs at the target frequency, f_0. In Fig. 6.3a, the predicted reflectance has been shown as a function of frequency when the thickness of layer 1 is $\lambda_0/4$ (black, solid), $3\lambda_0/4$ (red, dashed), and $5\lambda_0/4$ (blue, dot-dashed line). All three thicknesses produce zero reflectance at the target frequency, but as the thickness of the layers increases, the width of the low-reflectance band decreases. The relationship between the width of the low reflectance band and the (odd-integer) number of quarter-wave plates is

shown in Fig. 6.3b: the full-width, half-maximum (FWHM) rapidly decreases as the number of quarter-wavelengths increases from 1 to 21, and then remains constant.



(a) (b)

Figure 6.3: Varying the quarter-wave plate thickness: in (a) the predicted reflectance has been shown when layer 1 has a thickness of one (black, solid), three (red, dashed), and five (blue, dot-dashed) quarter-wavelengths at the target frequency. In (b), the full-width half-maximum has been shown as a function of the thickness of layer 1, d_1, normalised by a quarter-wavelength. The target frequency, f_0, is equal to 5MHz.

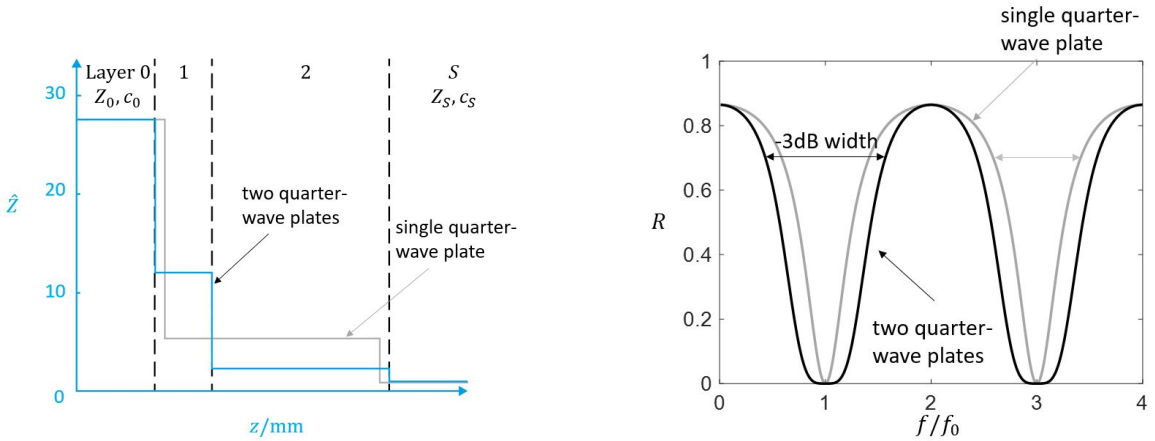
Beyond altering the thickness of layer 1 by odd numbers of the quarter-wavelength, there is limited ability to improve the performance of a quarter-wave anti-reflection coating without adding more layers. For example, the width of the zero-reflectance band can be widened by using a series of quarter-wave plates that gradually increase in acoustic impedance from layer 0 to the final layer, S [95]. In optics, two quarter-wave plates were shown to achieve maximal flat anti-reflectance bands when the optical admittance was $y_0^{3/4} y_S^{1/4}$ in the first layer and $y_0^{1/4} y_S^{3/4}$ in the second layer, where y_0 and y_S were the optical admittance of the left and right substrates, respectively [96]. Thus, using the acoustic analogy derived in Ch. 3 (Eq. 3.35), the optical admittance can be replaced by the acoustic impedance and the two acoustic quarter-wave plates must have acoustic impedances of:

$$Z_1 = Z_0^{3/4} Z_S^{1/4} \tag{6.10}$$

$$Z_2 = Z_0^{1/4} Z_S^{3/4} \tag{6.11}$$

to achieve maximal flat anti-reflectance bands. When layer 0 and S are copper and water, respectively, the acoustic impedance mismatch, $\hat{Z}$, across the structure, relative to the water layer, is shown in Fig. 6.4a. As desired, the acoustic impedances of the two quarter-wave plates (blue) step down more gradually from the acoustic

impedance in layer 0 to S, compared to the single quarter-wave plate (grey). The resultant reflectance from the two-layer structure with these theoretical values of acoustic impedance is shown in Fig. 6.4b in black. The -3dB bandwidth of the zero reflectance band has increased by about 1.4 times compared to the single quarter-wave plate (grey).



(a) (b)

Figure 6.4: Two quarter-wave plates vs. a single quarter-wave plate: the performance of a quarter-wave plate can only be improved by adding more layers. The acoustic impedance is bridged from layer 0 to S by setting the acoustic impedances in layer 1 and 2 equal to the expressions in Eqs. 6.10 and 6.11.

However, for both the single quarter-wave plate and the two quarter-wave plate structure, materials which satisfy the necessary acoustic impedance conditions may not exist in reality.

6.1.2 Symmetric multilayers

In the previous section it was shown that, in order to achieve zero reflectance, a quarter-wave plate positioned between two materials must satisfy the condition:

$$Z_1^2 = Z_0 Z_S, \tag{6.9}$$

where the subscripts 0 and S refer to the left and right substrate, respectively. In some cases, a material with the necessary acoustic impedance will not exist. However, this problem can be overcome by using a symmetric three-layered anti-reflection coating, which has an equivalent acoustic impedance, Z_E, and phase thickness, ϕ_E, that

satisfy the conditions of zero-reflectance. Symmetric multilayered structures for anti-reflection have been outlined extensively for optical applications [34, 35]. However, there are only a few papers detailing the acoustic counterpart [83, 95, 97–99].

Consider the single layer structure shown in Fig. 6.5, which has been irradiated from the left by an external acoustic source. A propagation matrix (Eq. 3.2) describes the coefficients of the acoustic signal at one point in layer 1 compared to another:

$$\begin{pmatrix} A_1' \\ B_1' \end{pmatrix} = \begin{bmatrix} \cos\phi_1 & \frac{Z_1}{\omega}\sin\phi_1 \\ -\frac{\omega}{Z_1}\sin\phi_1 & \cos\phi_1 \end{bmatrix} \begin{pmatrix} A_1 \\ B_1 \end{pmatrix}, \tag{6.12}$$

where $\phi_1 = k_1 d_1'$ and, as in Chapter 3, A_q and B_q are the coefficients of the right and left travelling components in the qth layer.

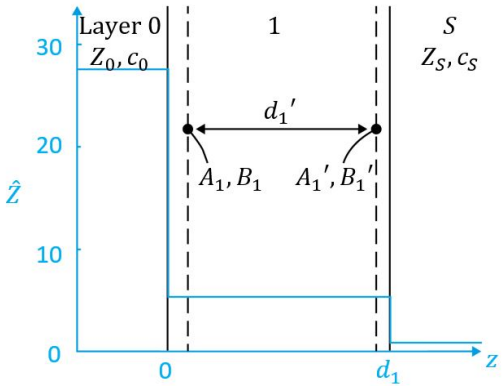


Figure 6.5: A single layer: the coefficients at one point in layer 1, A_1' and B_1', can be described in terms of the coefficients at another point, A_1 and B_1, using one propagation matrix. Layer 0 and S are semi-infinite substrates, the acoustic impedance mismatch, relative to the acoustic impedance of layer S, is shown in blue and the structure has been irradiated from the left by an external acoustic signal.

If, however, three layers are positioned between the two semi-infinite substrates, as shown in Fig. 6.6, then the product of three propagation matrices describes the coefficients, A_3' and B_3', at one point in layer 3 in terms of the coefficients, A_1' and B_1', at a point in layer 1, i.e,

$$\begin{pmatrix} A_3' \\ B_3' \end{pmatrix} = \begin{bmatrix} \cos\phi_3 & \frac{Z_3}{\omega}\sin\phi_3 \\ -\frac{\omega}{Z_3}\sin\phi_3 & \cos\phi_3 \end{bmatrix} \begin{bmatrix} \cos\phi_2 & \frac{Z_2}{\omega}\sin\phi_2 \\ -\frac{\omega}{Z_2}\sin\phi_2 & \cos\phi_2 \end{bmatrix} \begin{bmatrix} \cos\phi_1 & \frac{Z_1}{\omega}\sin\phi_1 \\ -\frac{\omega}{Z_1}\sin\phi_1 & \cos\phi_1 \end{bmatrix} \begin{pmatrix} A_1' \\ B_1' \end{pmatrix}, \tag{6.13}$$

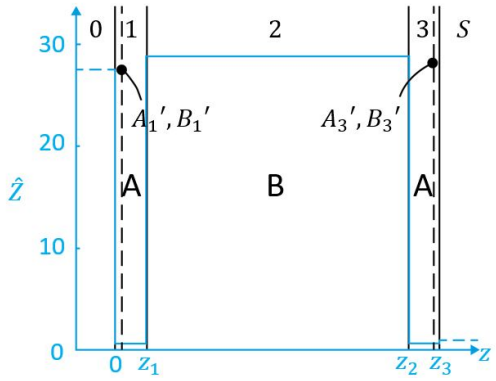


Figure 6.6: Symmetric multilayer: layers 1 and 3 have the same acoustic impedance mismatch (shown in blue) and the same thickness and so the coefficients in layer 3 can be written in terms of the coefficients in layer 1, using just one propagation matrix. An equivalent acoustic impedance, Z_E, and phase, ϕ_E, for the three layers can be defined, such that the three layers can be treated as one. Material properties can be found in Table 6.2 and the corresponding reflectance is shown in black in Fig. 6.7.

The three-layer structure is symmetric because layers 1 and 3 have the same acoustic impedance (shown in blue) and the same thickness. As a result, Eq. 6.13 can be written in the same form as the single layer case (Eq. 6.12), such that,

$$\begin{pmatrix} A_3' \\ B_3' \end{pmatrix} = \begin{bmatrix} \cos\phi_E & \frac{Z_E}{\omega}\sin\phi_E \\ -\frac{\omega}{Z_E}\sin\phi_E & \cos\phi_E \end{bmatrix} \begin{pmatrix} A_1' \\ B_1' \end{pmatrix}. \tag{6.14}$$

and the definitions of ϕ_E and Z_E can be found by matrix multiplication of the three propagation matrices in Eq. 6.13. The equivalent phase thickness, ϕ_E, and the equivalent acoustic impedance, Z_E, are given by:

$$\phi_E = \cos^{-1}\left(\cos 2\phi_A \cos\phi_B - \frac{1}{2}\left(\frac{Z_A}{Z_B} + \frac{Z_B}{Z_A}\right)\sin 2\phi_A \sin\phi_B\right) \tag{6.15}$$

$$Z_E = \frac{Z_A}{\sin\phi_E}\left(\sin 2\phi_A \cos\phi_B + \frac{1}{2}\left(\frac{Z_B}{Z_A} + \frac{Z_A}{Z_B}\right)\cos 2\phi_A \sin\phi_B + \frac{1}{2}\left(\frac{Z_B}{Z_A} - \frac{Z_A}{Z_B}\right)\sin\phi_B\right) \tag{6.16}$$

respectively, where the subscript A has been used to denote layers 1 and 3 ($Z_1 = Z_3 = Z_A$, $\phi_1 = \phi_3 = \phi_A$) and the subscript B denotes layer 2.

For an anti-reflection coating, the three layers must have an equivalent phase thickness of $\phi_E = \pi/2$, and so Eq. 6.15 becomes:

$$0 = \left(\cos 2\phi_A \cos\phi_B - \frac{1}{2}\left(\frac{Z_A}{Z_B} + \frac{Z_B}{Z_A}\right)\sin 2\phi_A \sin\phi_B\right), \tag{6.17}$$

which can be rearranged to find an expression for ϕ_B in terms of ϕ_A:

$$\tan\phi_B = \frac{1}{\tan 2\phi_A}\frac{2Z_A Z_B}{(Z_A^2 + Z_B^2)}. \tag{6.18}$$

Then, Eq. 6.18 can be substituted into Eq. 6.16 to find an expression for ϕ_A, in terms of the acoustic impedances in the layers [83]:

$$\cos 2\phi_A = \frac{(Z_B^2 + Z_A^2)(Z_E^2 - Z_A^2)}{(Z_B^2 - Z_A^2)(Z_E^2 + Z_A^2)} \tag{6.19}$$

where, for zero reflectance, $Z_E^2 = Z_0 Z_S$.

For example, the single quarter-wave plate used in Fig. 6.2 can be replaced by three layers of, say, the commonly-used polymer, polydimethylsiloxane (PDMS), and chromium (see Table 6.2 for material properties). Using Eq. 6.19, the phase thickness of layer A can be derived:

$$\phi_A = 0.127, \tag{6.20}$$

and then, the phase thickness of layer B, ϕ_B, is found from Eq. 6.18:

$$\phi_B = 0.180. \tag{6.21}$$

When the target frequency is $f_0 = 5$MHz, the thickness of layers A and B is calculated to be:

$$d_A = \frac{\phi_A}{k_A} = \phi_A \left(\frac{c_A}{2\pi f_0}\right) = 3.99\mu\text{m}, \tag{6.22}$$

$$d_B = \frac{\phi_B}{k_B} = \phi_B \left(\frac{c_B}{2\pi f_0}\right) = 33.9\mu\text{m}, \tag{6.23}$$

respectively.

Layer No.	Material	Z $\times 10^6$/ kg m^{-2} s^{-1}	d/ μm
0	Copper	40.7	-
1(A)	PDMS	1	3.99
2(B)	Cr	42.8	33.9
3(A)	PDMS	1	3.99
S	Water	1.5	-

Table 6.2: Layer materials and properties of the structure shown in Fig. 6.6 at the target frequency of $f_0 = 5$MHz.

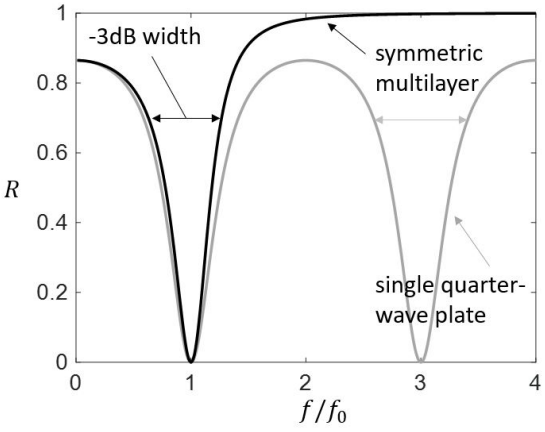


Figure 6.7: Reflectance of symmetric multilayer: the three symmetric layers successfully produce zero reflectance (black) at the target frequency, $f_0 = 5$MHz. Compared to a single quarter-wave plate (grey), the reflectance is now dispersive and has a smaller -3db bandwidth.

The reflectance of the structure has been shown in black in Fig. 6.7. As designed, the structure produces zero reflectance at the target frequency, f_0, just like the single quarter-wave plate (shown in grey), but the -3dB bandwidth is now 0.77 times smaller. Furthermore, the reflectance is asymmetric because Z_E, unlike Z_A and Z_B, is frequency-dependent: Eq. 6.16 depends on the phase of layers A and B and so the reflectance is dispersive. This dispersion, which results from the structure rather than the materials, can become a significant issue if the anti-reflectance band needs to be wider [83].

Thus, by defining an equivalent acoustic impedance, Z_E, and phase thickness, ϕ_E, three symmetric layers can be used to replace a single quarter-wave plate and achieve zero-reflectance at the target frequency using any two materials (summarised in Fig. 6.8). Such structures could be crucial to providing anti-reflection properties in applications where the design may be constrained to a limited selection of materials.

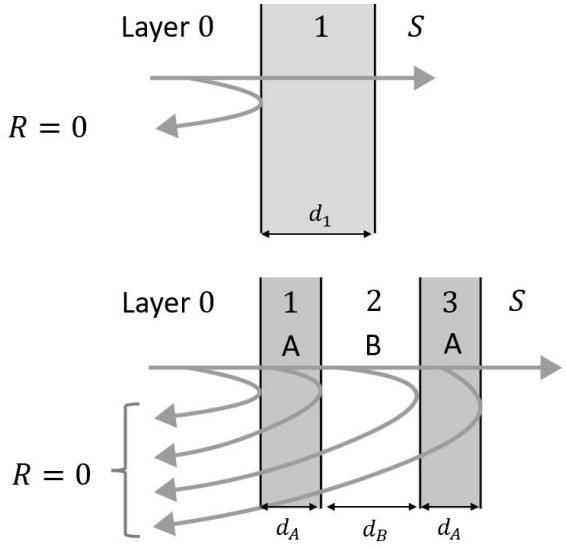


Figure 6.8: Using existing materials: In a single-layer anti-reflection coating (top), as well as being a quarter-wave plate, layer 1 must satisfy the condition given by Eq. 6.9 and thus the number of materials that can be used to acheive zero reflectance is limited. However, a symmetric multilayered structure (bottom) can achieve zero reflectance at the same target frequency using *any* material. Instead, the layer thicknesses, d_A and d_B, are used to ensure that the equivalent phase thickness, ϕ_E, and equivalent acoustic impedance, Z_E, (Eqs. 6.16 and 6.15, respectively) satisfy the zero-reflectance condition at the target frequency.

6.2 High-reflectance coatings

Quarter-wave plates can also be used to produce high-reflectance coatings. Recall that an acoustic signal travelling from a high impedance material to a low impedance material experiences a π-phase shift, and no phase shift when travelling from low to high. Thus, when irradiated by an external acoustic source, a stack of quarter-wave plates, with alternating high and low acoustic impedance, produces reflected components that arrive in phase with each other and constructively interfere, as illustrated in Fig. 6.9.

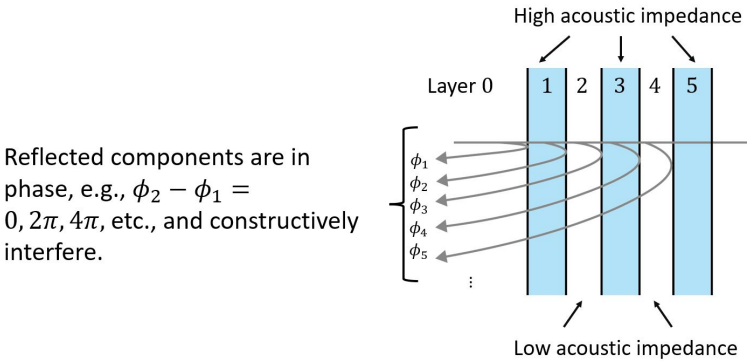


Figure 6.9: In phase reflections: acoustic reflections from successive layers of high and low acoustic impedance materials, with quarter-wavelength thicknesses, arrive in phase and constructively interfere.

Similar to anti-reflection coatings, high-reflection coatings have been widely used in optical systems to enhance performance. For example, the Fabry-Perot interferometer uses interference to enhance the optical reflection from thin metal layers and reduce potentially damaging levels of absorption [35]. By controlling the distance between the thin metal layers, light of certain wavelength constructively interferes, resulting in high detector outputs at these wavelengths. Because of this, the resonant cavities are often used as optical filters and for high-resolution spectroscopy [100–102]. Indeed, optical resonant cavities have even been used in photoacoustic generation. In work by Lee et al [50], an optical cavity was set-up between the photoacoustic source and a thin layer of aluminium. Light absorption in the photoacoustic source was increased due to the constructive interference of light between the two thin metal films and as a result, the photoacoustic conversion efficiency was improved.

However, in comparison, the acoustic equivalent appears to be underused. A multilayered structure of alternating high and low acoustic impedance was used by Gutierrrez-Reyes et al [22] to design an ultrasonic sensor for photoacoustic signals.

However, just one period of copper (high acoustic impedance) and polyvinylidene fluoride (low acoustic impedance) was modelled. In the following section, the formulated model from Chapter 4 has been used to investigate the effect of the number of periods and the acoustic impedance mismatch between layers on the spectral response of multilayered photoacoustic structure.

In Fig. 6.10, structures with N periods of alternating high and low impedance are irradiated by an external acoustic source. The source terms in the formulation from Chapter 3 (Eq. 3.6) have been set to zero and the coefficient of the right-travelling component in layer 0 has been set to 1, i.e.,

$$A_0 = 1.$$

The reflectance, R, detected in layer 0 has been shown when the acoustic impedance mismatch is $\hat{Z} = 2$ (left panel) and when $\hat{Z} = 10$ (right panel). For both values of $\hat{Z}$, the number of periods has been varied from 2 to 5. Because all the layers act as quarter-wave plates at the same frequencies, the sonic transit time is the same in every layer:

$$\frac{d_1}{c_1} = \frac{d_2}{c_2} = \frac{d_3}{c_3}, \quad \text{etc.}$$

and so the subscripts have been dropped in the following sections. When $\hat{Z} = 2$, $\frac{d}{c} = 480$ns and when $\hat{Z} = 10$, $\frac{d}{c} = 210$ns.

In both Figs. 6.10c and 6.10d, the reflectance has bands of high-reflectance, centred at odd integer values of $\hat{\omega} = \pi/2$, where each layer acts as a quarter-wave plate. At all integer values of $\hat{\omega} = \pi$, the reflectance is at a minimum because each layer acts as a half-wave plate, or an absentee layer.

In Fig. 6.10c, when the acoustic impedance mismatch is $\hat{Z} = 2$, increasing the number of periods from 2 (red) to 5 (blue), increases the reflectance at the $\hat{\omega} = \pi/2$ from about 0.7 to 0.9. The ripple between the high-reflectance bands also increases, both in the number of oscillations and in magnitude, but the reflectance remains zero at $\hat{\omega} = \pi$.

In Fig. 6.10d, the acoustic impedance mismatch has increased to $\hat{Z} = 10$. The high-reflectance bands are wider, with the -3dB bandwidth now about three times greater, and $R \approx 1$ at odd integer values of $\pi/2$.

Thus, the design of a high-reflectance coating requires the careful control of:

- the number of periods of alternating high and low impedance layers
- and the acoustic impedance mismatch between the alternating layers of high and low acoustic impedance materials.

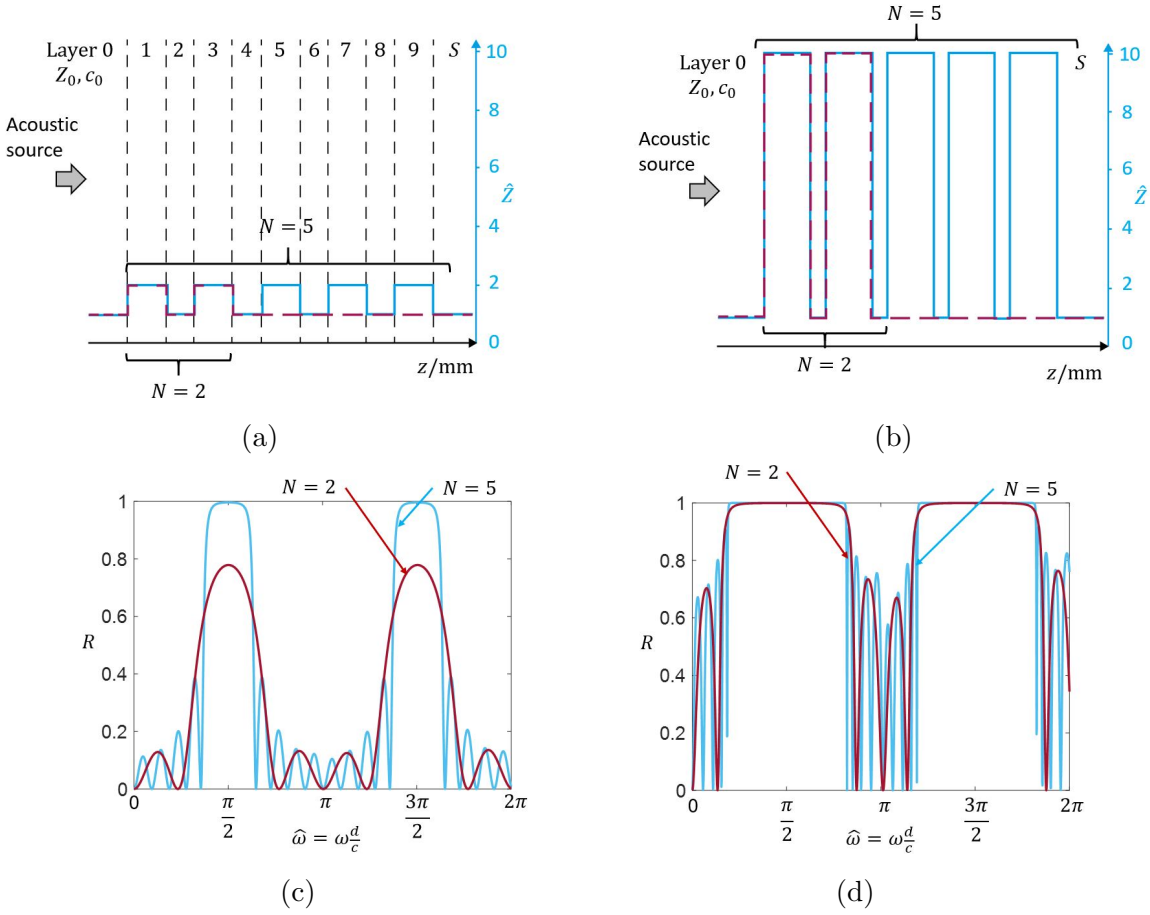
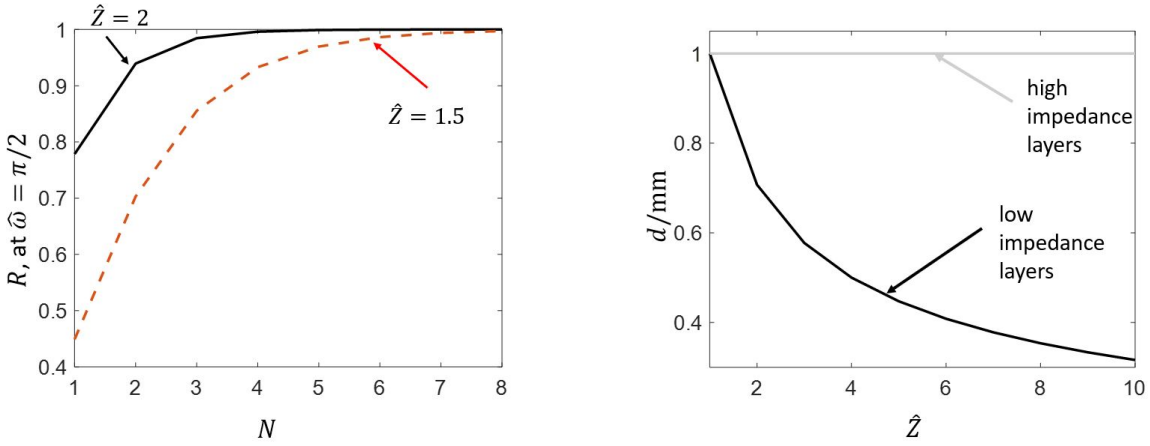


Figure 6.10: High-reflectance coatings: N periods of alternating high and low acoustic impedance layers, all with quarter-wave thickness, increases the reflectance at the target frequency. In the left panel, the acoustic impedance mismatch is $\hat{Z} = 2$ and in the right panel, $\hat{Z} = 10$. The structures have 2 or 5 periods, shown in red and blue, respectively. In (c) and (d) the reflectance, R, detected in layer 0 is shown when the structures are irradiated by an external acoustic source. Increasing the number of periods increases the reflectance at $\hat{\omega} = \pi/2$ and increasing the impedance mismatch increases the -3dB bandwidth. (The odd layers all have a thickness of 1mm and a speed of sound equal to $c_w\sqrt{\hat{Z}}$, where the subscript w denotes water. The even layers all have a thickness equal to $1/\sqrt{\hat{Z}}$mm and a speed of sound equal to c_w.)

The number of periods, N, can be used to control the value of the maximum reflectance, measured at odd integers of $\pi/2$. Fig. 6.11a shows the maximum reflectance, R, as a function of the number of periods, N, when the acoustic impedance mismatch is $\hat{Z} = 2$ (black) and $\hat{Z} = 1.5$ (red, dashed). As N increases, the maximum reflectance increases until a constant value of approximately 1 is reached. The higher acoustic impedance mismatch multilayer requires only 5 periods to achieve a reflectance of 1, while a lower acoustic impedance mismatch requires about 8. In-

creasing the number of periods beyond 8 will have no further effect on the reflectance of the coating but will increase the complexity of the fabrication process.

The acoustic impedance mismatch can be used to control the width of the high-reflectance band. For example, as demonstrated in Fig. 6.10d, if wider bands of high-reflectance are required for an application, then a higher acoustic impedance mismatch should be chosen (in this case, $\hat{Z} = 10$). However, increasing the acoustic impedance mismatch decreases the sonic transit time in the high impedance layers. If the high impedance layers have a fixed thickness of 1mm, then to ensure the sonic transit time is the same in every layer, the thickness of the low impedance layers must be decreased. The relationship between the acoustic impedance mismatch, $\hat{Z}$, and the thickness of the layers is shown in Fig. 6.11b.



(a) (b)

Figure 6.11: Designing high-reflectance coatings: in (a), the reflectance, R at odd integer values of $\hat{\omega} = \pi/2$ is shown as a function of the number of periods, N, of alternating high and low impedance layers, when the acoustic impedance mismatch is $\hat{Z} = 2$ (black) and $\hat{Z} = 1.5$ (red, dashed). Increasing the number of periods will result in higher maximum reflectance. However, a lower acoustic impedance mismatch requires more periods to achieve maximum reflectance. In (b), the thickness of the low impedance layers (shown in black) must change as the acoustic impedance mismatch, $\hat{Z}$, changes to ensure the sonic transit time stays the same in every layer because the high impedance layers have a fixed thickness of 1mm (shown in grey).

Without acoustic absorption, the sum of the transmittance and reflectance is:

$$R + T = 1,$$

due to the conservation of acoustic energy, and the transmittance, T_{0S}, in layer S can

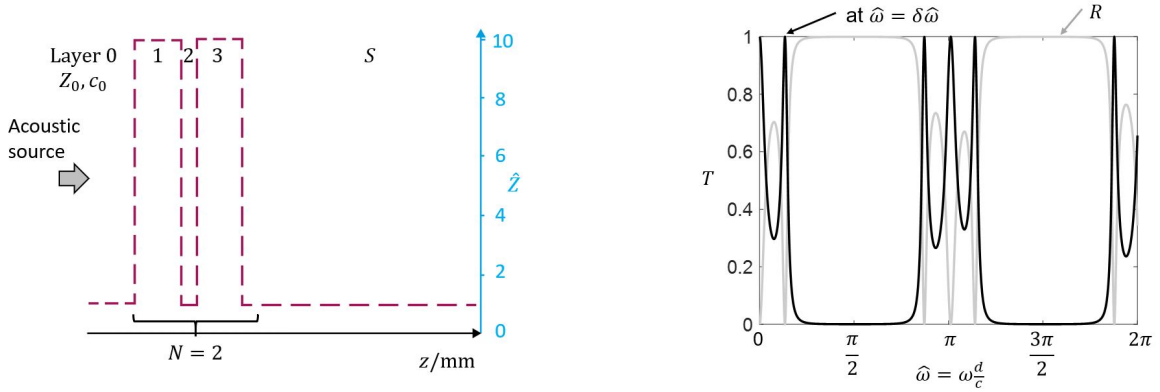
calculated using Eq. 3.31 from Chapter 3. When $A_0 = 1$,

$$T_{0S} = \frac{Z_0}{Z_S}\frac{|A_S|^2}{|A_0|^2} = \frac{Z_0}{Z_S}|p_s(z,\omega)|^2 \tag{6.24}$$

where p_S is the acoustic signal detected at a fixed z-position in layer S.

For the quarter-wave plate stack with two periods and an acoustic impedance mismatch of $\hat{Z} = 10$ (shown again in Fig. 6.12a), the transmittance in layer S is shown in Fig. 6.12b. As expected, there are low-transmission bands centred around odd integer values of $\hat{\omega} = \pi/2$, where the layers act as quarter-wave plates, but more interestingly, to either side of the peaks in transmission at $\hat{\omega} = \pi$, is an additional peak, i.e., at $\hat{\omega} = n\pi \pm \delta\hat{\omega}$, and for this structure $\delta\hat{\omega} = 0.13\pi$. These are the same low-frequency peaks seen in the frequency spectrum of the acoustic signal detected from a photoacoustic structure with two absorbing layers, as was shown in Chapter 5 for optically thin (Fig. 5.5) and optically thick absorbers (Fig. 5.6).

It was already noted from the reflectances in Fig. 6.10 that the number of oscillations of the ripple increased as the number of periods was increased and that the magnitude of these subsidiary peaks increased as the acoustic mismatch increased. Thus, it can be concluded that these additional peaks in the transmittance are also dependent on the number of periods and the acoustic impedance mismatch.



(a) (b)

Figure 6.12: Low transmittance: without acoustic absorption, a high-reflectance coating results in low transmission through the quarter-wave stack, shown in (a) where, $N = 2$ and $\hat{Z} = 10$. In (b), the transmittance (black) has low-transmittance bands, centred at $\hat{\omega} = \pi/2$, and high transmittance peaks at $\hat{\omega} = n\pi \pm \delta\hat{\omega}$, where $\delta\hat{\omega} = 0.13\pi$. (The reflectance, R, has been shown again in grey to confirm that $R + T = 1$.)

Before discussing the reappearance of $\delta\hat{\omega}$ further, the properties of the subwavelength acoustic structures explored so far in this Chapter are summarised. When irradiated by an external acoustic source, it has been found that:

- a single quarter-wave plate can be used as an anti-reflection coating because it has a phase thickness of $\phi = \pi/2$ at a target frequency, f_0.
- To achieve zero reflectance, the quarter-wave plate must have an acoustic impedance, Z_1, that satisfies the condition:

$$Z_1^2 = Z_0 Z_S,$$

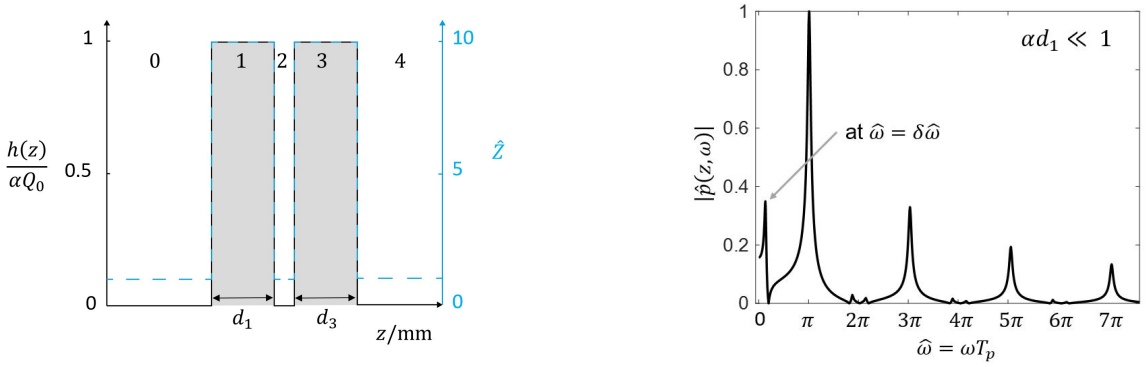
  where, Z_0 and Z_S are the impedances of the substrates.
- When such a material cannot be found, the single quarter-wave plate can be replaced by three symmetric layers. The multilayer stack has an equivalent acoustic impedance, Z_E, and phase thickness, ϕ_E, that satisfy the conditions for zero-reflectance, without constraining the three layers to specific materials.
- Then, the phase thickness, and hence the thickness, of the layers can be derived using,

$$\tan \phi_B = \frac{1}{\tan 2\phi_A} \frac{2Z_A Z_B}{(Z_A^2 + Z_B^2)}, \tag{6.18}$$

  and Eq. 6.16.
- Finally, a stack of quarter-wave plates, with alternating layers of high and low acoustic impedance, can be used as a high-reflectance coating, where
  - increasing the number of periods, N, increases the reflectance at the target frequency and the number of oscillations between the high-reflectance bands,
  - increasing the acoustic impedance mismatch, $\hat{Z}$, increases the -3dB bandwidth of the high-reflectance band, and the magnitude of the ripple between the high-reflectance bands.

Now consider the photoacoustic structure which generated the acoustic signal where the low-frequency peak at $\hat{\omega} = \delta\hat{\omega}$ was first observed. The signal was modelled by Sun et al with optically thin absorbers [23], and then with optically thick absorbers in Chapter 5. Recall that two optically absorbing layers (layers 1 and 3) were separated by a low impedance, transparent layer (layer 2), where the acoustic impedance mismatch between the absorbers and surrounding media was $\hat{Z} = 10$ (shown again in Fig. 6.13a). When irradiated by a light source on the left, the absorbing layers each generated an acoustic signal of pulse width, T_p, and its frequency spectrum, detected in layer 4, had resonant peaks at odd integer values of $\hat{\omega} = \pi$, where $\hat{\omega} = \omega T_p$

(shown again in Fig. 6.13b). A low-frequency peak was also observed and Sun et al. approximated its position, $\delta\hat{\omega}$, using a mass-spring analogy [23].



(a) (b)

Figure 6.13: Revisiting the two-absorber structure from Ch 5: in (a) two absorbing layers are separated by a transparent layer, where the acoustic impedance mismatch is $\hat{Z} = 10$ (blue). The heating function of each layer is shown in black and shaded. When layers 1 and 3 are optically thin, the heating function is constant. The frequency spectrum of the signal detected in layer 4 is shown in (b) and has resonant peaks at odd integer values of π and a low frequency peak at $\delta\hat{\omega}$.

At the end of Chapter 5, it was noted that, in the short-pulse regime, the generated acoustic signal had a wavelength, cT_p, that was always less than or equal to the dimensions of the absorbers (d_1 and d_3), i.e.,

$$c_1 T_p \leq d_1,$$

where $c_1 = c_3$ and $d_1 = d_3$.

Furthermore, when the sonic transit time in both the absorbing and transparent layers was the same, such that,

$$\frac{d_1}{c_1} = \frac{d_2}{c_2} = \frac{d_3}{c_3}, \tag{6.25}$$

then all three layers had a thickness equal to the acoustic wavelength. In the context of the subwavelength structures discussed so far in this Chapter, this means that, at the same frequency, all three layers act as half-wave plates, with a π phase thickness.

Next, consider the high-reflectance structure, shown in Fig. 6.12a, with alternating layers of high and low impedance, which also have an acoustic impedance mismatch of $\hat{Z} = 10$ and equal sonic transit time. However, the structure has no optically absorbing layers and was irradiated by an external acoustic source. Its transmittance is shown in Fig 6.12b and has maxima at *all* integer values of $\hat{\omega} = \pi$, where the layers

acted as half-wave plates, and minima at integer values of $\hat{\omega} = \pi/2$, where the layers acted as quarter-wave plates. The acoustic signal, $|p_s(z,\omega)|$, in layer S (not shown) has the same properties because when $A_0 = 1$,

$$T_{0S} = \frac{Z_0}{Z_S}|p_s(z,\omega)|^2. \tag{6.24}$$

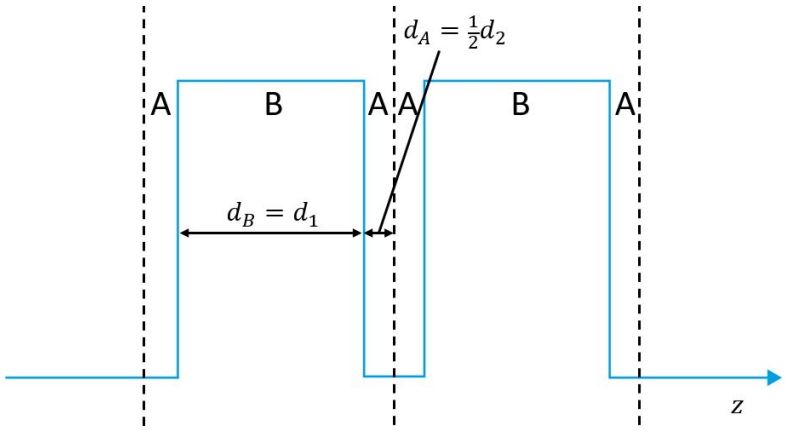


Figure 6.14: Two-stack symmetric multilayer: the structure in Fig. 6.13a can be considered as a stack of two symmetric multilayers, where the 'A' layers have the same acoustic impedance as the transparent media ($Z_A = Z_2$) and half the thickness ($d_A = d_2/2$). The 'B' layers, have the same acoustic impedance and thickness as the absorbing layers, i.e. $Z_B = Z_1 = Z_3$ and $d_B = d_1 = d_3$.

There were also subsidiary peaks to either side of the resonant peaks and these can be explained by considering the structure in Fig. 6.12a as a stack of two symmetric multilayers, illustrated in Fig. 6.14, where now

$$\hat{Z} = \frac{Z_1}{Z_2} = \frac{Z_B}{Z_A} = 10, \tag{6.26}$$

and

$$d_A = \frac{d_2}{2}, \quad d_B = d_1, \tag{6.27}$$

and thus, the phase can be expressed as:

$$\phi_A = \frac{1}{2}\phi_B. \tag{6.28}$$

In Section 6.1, it was shown that a symmetric multilayer will act as an anti-reflection quarter-wave plate if the phase thickness of layer B, ϕ_B, satisfies the expression in

Eq. 6.18, i.e., when

$$\tan^2\phi_B = \frac{2(Z_A)(10Z_A)}{100Z_A^2 + Z_A^2}$$
$$\phi_B = \tan^{-1}\left(\sqrt{\frac{20}{101}}\right) = 0 \pm 0.13\pi, \pi \pm 0.13\pi, \text{etc.} \tag{6.29}$$

and hence, the *two*-stack symmetric multilayer will act as a half-wave plate when $\phi_B = n\pi \pm 0.13\pi$, where n is an integer. Thus, in summary, the transmittance of the high-reflectance coating (two-stack multilayer), irradiated by an external acoustic source, is at a maximum when:

- each layer has a thickness of a half-wave plate: $d_1 = d_2 = d_3 = T_p/2$ and hence, $\phi_1 = \phi_2 = \phi_3 = \omega T_P = \pi$,
- and when the total thickness of the equivalent two-stack symmetric multilayer is a half-wave plate, i.e. when $\phi_1 = \phi_2 = \phi_3 = n\pi \pm 0.13\pi$, where n is an integer.

Thus, by comparing Fig. 6.13b and Fig. 6.12, it can now be seen that when photoacoustic sources are included in the high-reflectance coating (Fig. 6.13), the resonant peaks at even integer values of π and the minima at $\pi/2$ are removed and the magnitude of the resonant peaks at odd integer values of π and the subsidiary peaks to either side of them are no longer uniform. These effects can be explained by complex analysis of the poles and zeros of the transfer-matrix when acoustic sources are not neglected, as will be discussed in Chapter 7.

6.3 Using subwavelength layers to improve emission efficiency

A photoacoustic source produces two pulses of equal magnitude, propagating in opposite directions, as illustrated in Fig. 6.15a. Thus, when a detector is placed to the right of the source, it measures only half of the generated signal. In Chapter 4, it was shown that a mechanical barrier, placed to the left of the source, reflected the left-travelling component back toward the detector (Fig. 6.15b). In work by Lee et al [50], the interface between PDMS and glass was used to reflect the acoustic signal generated by an ultrathin Cr layer (thickness of 100nm), where the reflectance between PDMS and glass, R_{PG} is given by:

$$R_{PG} = \left|\frac{1-\hat{Z}}{1+\hat{Z}}\right|^2 = 0.75 \tag{6.30}$$

and is independent of frequency. However, in this chapter it has been shown that the reflectance at an interface can be increased to approximately 1 at a target frequency by using a high-reflectance coating, comprised of alternating layers of high and low impedance material (see Fig. 6.15c).

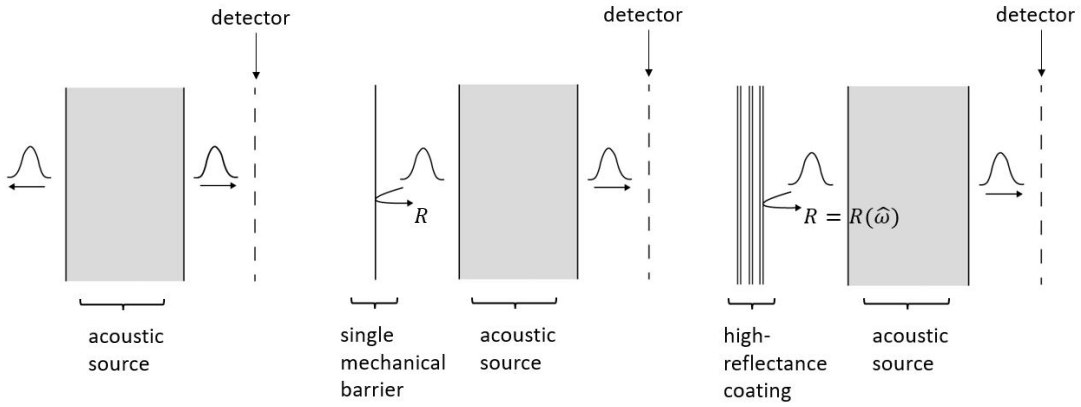
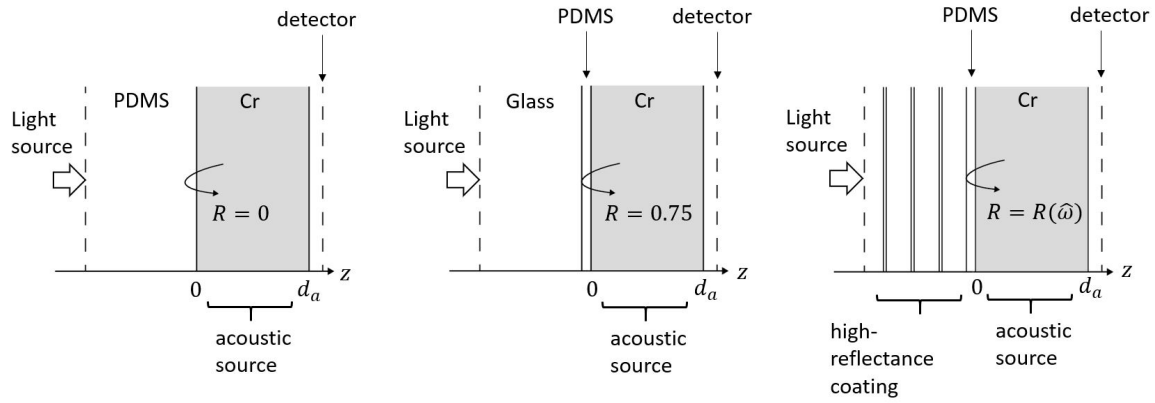


Figure 6.15: Controlling reflections: in (a) the acoustic source (shaded region) generates two pulses of equal magnitude, propagating in opposite directions. A detector positioned to the right of the source will only detect the right-travelling pulse; the left-travelling pulse is lost in the semi-infinite layer on the left. To counter this, a mechanical barrier, or backing layer, can be placed to the left of the acoustic source, as in (b). Then, the left-travelling signal will be reflected at the interface and travel towards the detector. However, the amplitude of the reflected signal can be increased even further by using a high-reflectance coating, as illustrated in (c). Using the correct combination of materials, the coating can increase the proportion of signal reflected back toward the detector to almost 1.

In Fig. 6.16, a single chromium (Cr) layer, acting as the photoacoustic source, is modelled with three different 'backing' conditions. The first structure, shown in Fig. 6.16a, has no backing layer; the Cr layer is sandwiched between two semi-infinite substrates of PDMS and there are no interfaces to the left of $z = 0$. In the second structure, shown in Fig. 6.16b, a transparent layer of PDMS, with a half-wavelength thickness, separates the acoustic source from the semi-infinite glass substrate on the left, i.e., there is one interface to the left of $z = 0$. The third structure has been designed to optimise the reflection of the left-travelling components generated in the acoustic source. A high-reflectance coating has been placed to the left of the acoustic source, as shown in Fig. 6.16c. The high-reflectance coating is made up of three periods of high and low impedance materials, in this case, glass and PDMS, respectively, and each layer has a quarter-wavelength thickness. Thus,

as demonstrated earlier in the section, the reflectance from the coating will no longer be fixed at $R = 0.75$, but will vary with frequency, i.e., $R = R(\omega)$.



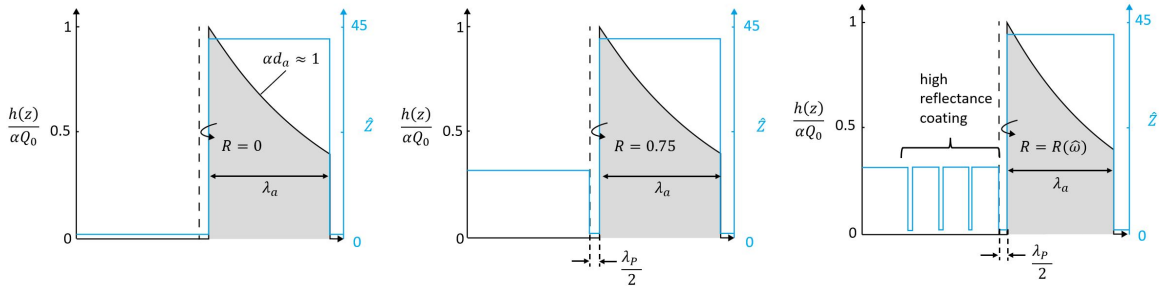
(a) (b) (c)

Figure 6.16: Improving emission efficiency: in the same way that a backing layer can be used to reflect some of the left-travelling components, generated by an acoustic source (Cr-layer, shaded), back toward a detector on the right, a high-reflectance coating can be used to reflect even more of the left-travelling signal. In (a), an 100nm-thick Cr layer acts as an acoustic source, surrounded by two semi-infinite layers of PDMS. There are no interfaces to the left of $z = 0$. In (b), a PDMS layer, with thickness of a half-wavelength, separates the source from a glass substrate on the left. Thus, there is a single interface to the left of the acoustic source, and the reflectance between glass and PDMS is 0.75. In (c), a quarter-wave plate stack, comprised of alternating layers of glass and PDMS, acts as a high-reflectance coating to the left of the source.

As in Lee et al [50], the thickness of the single layer of chromium is 100nm and it absorbs approximately 60% of the irradiating light energy. This corresponds to an optical absorption coefficient of $\alpha = 9.2 \times 10^6 \mathrm{m}^{-1}$ and the optical thickness, αd_a, is approximately 1. When irradiated by light in the short-pulse regime ($\tau_p = 10^{-12}$s), the Cr layer generates an acoustic signal of pulse width:

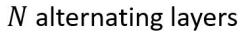
$$T_p = \tau_{aco} = \min\left(\frac{1}{\alpha c_a}, \frac{d_a}{c_a}\right) = \frac{d_a}{c_a} = 1.7 \times 10^{-11}\mathrm{s}. \tag{4.2}$$

Thus, if optical absorption is assumed to follow Beer's Law, then the heating function will decay exponentially across the absorbing layer, as shown in black (shaded) in Fig. 6.17 for each structure. The material properties and thickness of each layer can be found in Table 6.3.



(a) (b) (c)

Figure 6.17: In all three structures in Fig. 6.16, the heating function (black, shaded) decays exponentially across the Cr layer and the acoustic impedance mismatch, $\hat{Z}$, relative to PDMS, is shown in blue. When irradiated by light in the short-pulse regime ($\tau_p = 10^{-12}$s), the generated acoustic signal has a pulse width of $T_p = \frac{d_a}{c_a}$, where d_a and c_a are the thickness and speed of sound of the Cr layer. The thickness of each layer can be found in Table 6.3.



Material	Glass	PDMS	Glass	PDMS	Cr	PDMS
$Z \times 10^6$/ kg m^{-2} s^{-1}	14.4	1.01	14.4	1.01	42.8	1.01
d/ nm	24.5 ($= \frac{\lambda_G}{4}$)	4.15 ($= \frac{\lambda_P}{4}$)	24.5 ($= \frac{\lambda_G}{4}$)	8.30 ($= \frac{\lambda_P}{2}$)	100 ($= \lambda_a$)	-



Table 6.3: A table of material properties and layer thicknesses for the multilayered structure shown in Fig. 6.17c.

In Fig. 6.18a, the reflectance of the acoustic signal is shown as a function of frequency for all three backing conditions and the following observations can be made:

- There is no reflectance of left-travelling components in the semi-infinite PDMS layer (orange, dashed).
- When a half-wave PDMS layer separates the source from the glass substrate on the left (structure shown in Fig. 6.17b), the reflectance is 0.75 (Eq. 6.30) and is constant at all frequencies (grey).
- When a high reflectance coating is used to the left of the acoustic source (structure shown in Fig. 6.17c), the reflectance of the left-travelling components (black) increases to approximately 1 when the frequency is at an odd integer value of $\hat{\omega} = 2\pi$. At these frequencies, the Cr layer has a thickness equal

to the acoustic wavelength, and the layers of the high reflectance coating are quarter-wave plates.

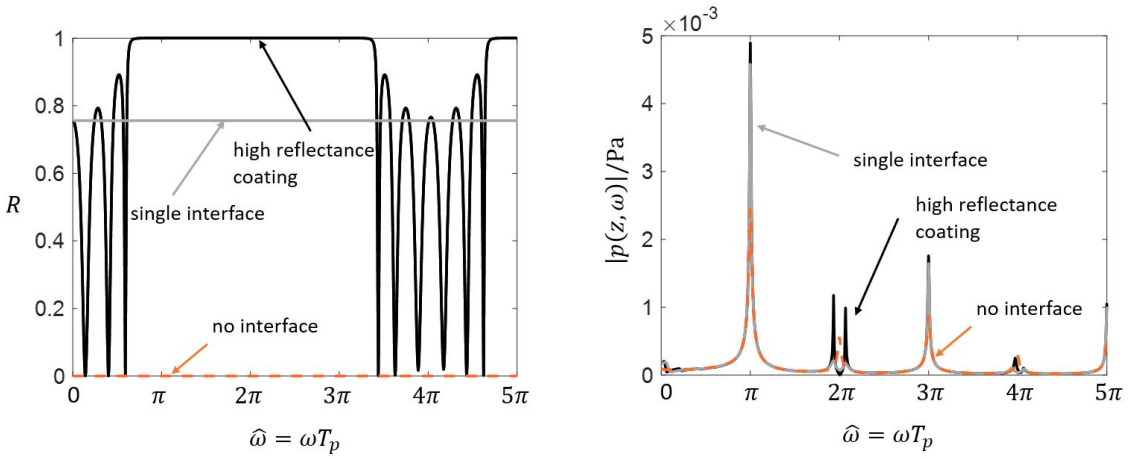


Figure 6.18: Increased reflectance: for the three structures shown in Fig. 6.17, the reflectance and acoustic signal are shown as a function of normalised frequency in (a) and (b), respectively. In (a), when there is no interface to the left of the acoustic source, the reflectance, R, is zero (orange, dashed) and the corresponding detected signal in (b) is comprised of only the right-travelling components, i.e. half of the total generated acoustic signal. When a single interface is positioned to the left of the acoustic source, the reflectance, shown in grey in (a), increases to 0.75 and the magnitude of the odd resonant peaks of the spectrum, shown in (b), increases by 86%. If a high-reflectance coating is used to reflect left-travelling components of the acoustic signal, then in (a) the reflectance becomes frequency-dependent, as shown in black and the corresponding detected signal in (b) has odd resonant peaks with double the magnitude compared to the no-interface case, and the even resonant peaks have disappeared.

The frequency spectrum of the acoustic signal, detected in the right-hand substrate, is shown in Fig. 6.18b for each of the three backing conditions and the differences in the spectra can be summarised:

- Without any backing layer, there are resonant peaks at odd integer values of π, which decay with $\hat{\omega}$ (orange, dashed). There are also resonant peaks at even integer values of π, due to the shape of the absorption profile of the Cr layer (see Appendix A.1).

- With a glass-PDMS interface to the left of the Cr layer, the reflection of the left-travelling component has resulted in a 86% increase in the magnitude of the

resonant peaks at odd integer values of π (shown in grey). However, the peaks at even integer values have now decreased because at these frequencies, the PDMS layer between the acoustic source and glass substrate acts as a half-wave plate and reflected components destructively interfere.

- When the high-reflectance coating is positioned to the left of the acoustic source, the magnitude of the peaks at odd integer values of π increases by a further 13.2% (shown in black) and are now double the size of the resonant peaks produced with no interface in the PDMS layer. But again, at even integer values of π, there are no longer resonant peaks due to destructive interference.

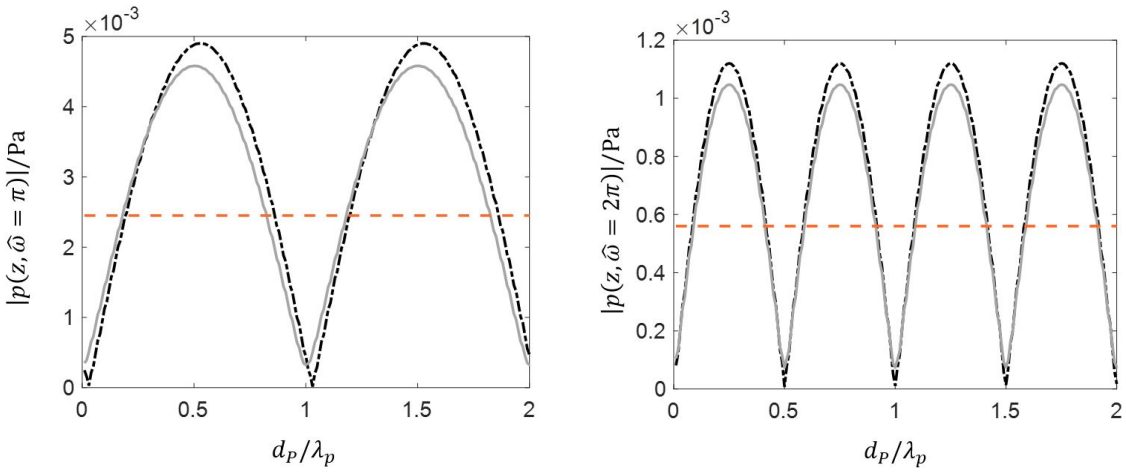


Figure 6.19: Positioning the reflective surface: the distance between the acoustic source and the reflective surface, i.e., the thickness of the PDMS layer in the structures in Fig. 6.17, must also be controlled to ensure the maximum detected signal. The amplitude of the detected signal is shown as a function of the thickness of the PDMS layer, when the frequency is fixed at (a) $\hat{\omega} = \pi$ and (b) $\hat{\omega} = 2\pi$. When there is no interface, the amplitude is constant at all thicknesses (shown in orange, dashed) in both (a) and (b). However, when a single interface or a high-reflectance coating is used, the amplitude of the acoustic signal (shown in grey and in black, dash-dotted, respectively) at both frequencies oscillates with the thickness of the PDMS layer. Note, the acoustic wavelength in the PDMS layer is $\lambda_P = 16.6$nm when the generated acoustic pulse width is $T_p = 1.7 \times 10^{-11}$s.

The destructive interference caused by the PDMS layer to the left of the acoustic source has been investigated further. In both of the structures in Figs. 6.17b and 6.17c, the acoustic source is separated from the reflecting surface by a half-wavelength thick PDMS layer. The PDMS thickness was chosen to ensure that the reflected pulses

arrive at the detector in phase and maximise the amplitude of the detected signal when the target frequency is $\hat{\omega} = \pi$. Fig. 6.19 shows the effect of the thickness of the PDMS layer on the amplitude of the detected signal, measured at a fixed frequency of $\hat{\omega} = \pi$ in (a), and at $\hat{\omega} = 2\pi$ in (b).

When just a single interface is used to reflect left-travelling components back towards the detector on the right, the magnitude of the acoustic signal at $\hat{\omega} = \pi$, shown in grey (solid) in Fig. 6.19a, is at a maximum (4.58 mPa) when the PDMS layer has a thickness equal to an odd integer of half-wavelengths, i.e., when $d_P/\lambda_P = 0.5, 1.5$, etc., where d_P is the thickness of the PDMS layer and λ_P is the wavelength of the acoustic signal in the PDMS layer. Similarly, when a high-reflectance coating is used to reflect the left-travelling components, the detected signal, shown in Fig. 6.19a in black (dashed), reaches a peak amplitude of 4.90 mPa at odd integers of half-wavelengths.

Contrary to this, the amplitude of the *second* resonant peak (at $\hat{\omega} = 2\pi$) is maximised by a different thickness of PDMS compared to the first resonant peak. As shown in Fig. 6.19b, when the fixed frequency is equal to $\hat{\omega} = 2\pi$, the amplitude of the detected signal is maximised when the PDMS layer has a thickness equal to an odd integer of *quarter*-wavelengths, i.e. when $d_P/\lambda_P = 0.25, 0.75$, etc. for both the single-interface and high-reflectance coating (shown in grey and black, respectively).

Hence, the thickness of every layer of a multilayered structure must be considered if an enhancement in amplitude is required at a target frequency. In this Section, the amplitude of the acoustic signal detected on the right-hand side of the acoustic source has been maximised at a target frequency of $\hat{\omega} = \pi$ by:

- irradiating the acoustic source by light in the short-pulse regime, such that the thickness of the acoustic source was equal to the generated acoustic wavelength.
- A high-reflectance coating positioned to the left of the acoustic source enabled approximately all of the left-travelling signal to be reflected back to the right by using alternating layers of high and low acoustic impedance materials, each with a quarter-wavelength thickness.
- Positioning the coating a half-wavelength away from the acoustic source ensured that the reflected components all arrived in phase and so the amplitude of the acoustic signal at $\hat{\omega} = \pi$ was increased.

6.3.1 Subwavelength structures with distributed heat sources

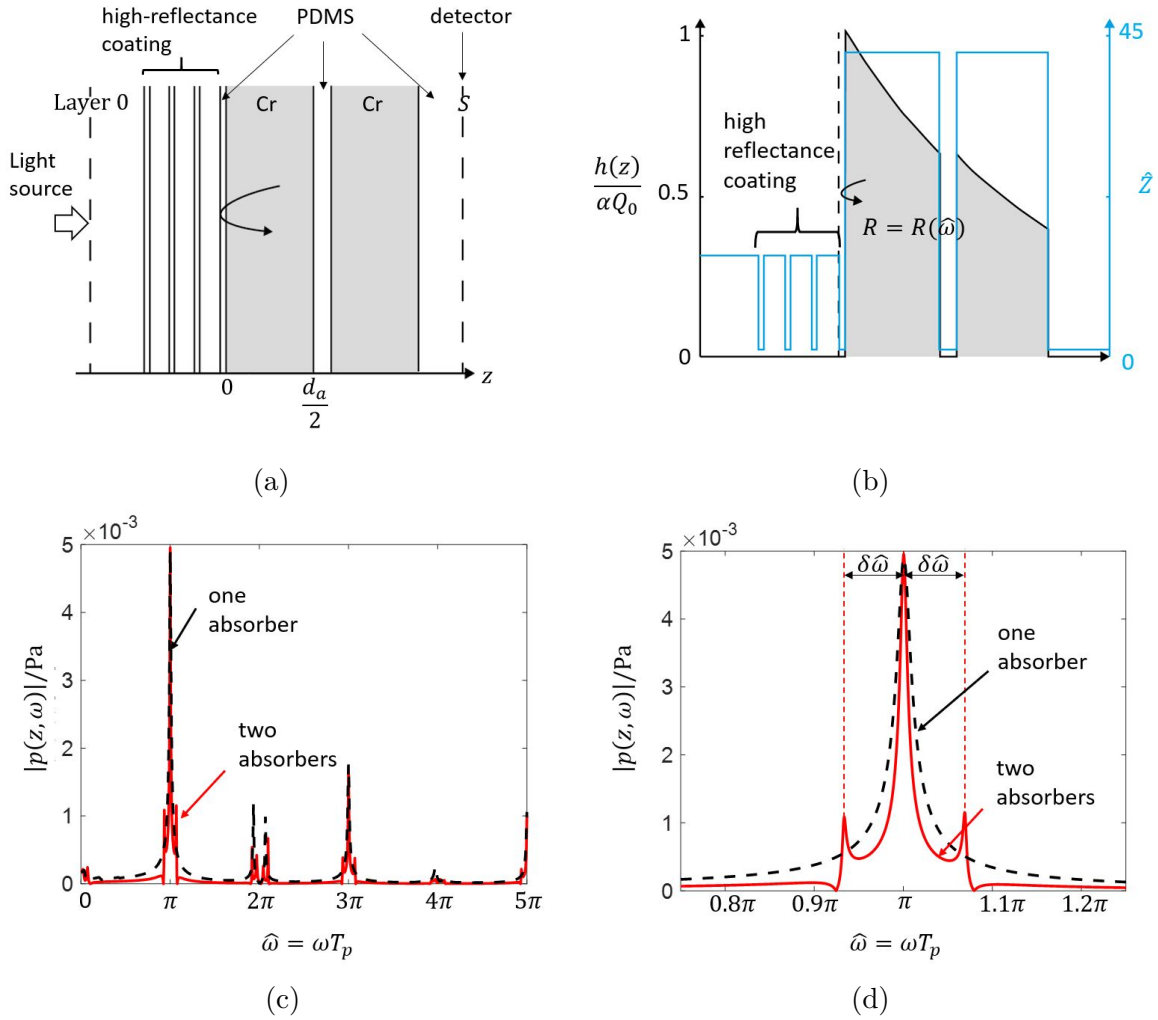


Figure 6.20: The effect of distributed heat sources on emission efficiency: (a) the 100nm-thick Cr layer has been replaced by two 50nm-thick Cr layers, separated by a transparent PDMS layer. The three layers all have the same sonic transit time, equal to the acoustic pulse width. In (b), the heating function (black) and acoustic impedance mismatch (blue), $\hat{Z}$, of each layer is shown. The frequency spectrum in (c) of the acoustic signal has odd resonant peaks with the same amplitude as those from the 100nm-thick Cr structure (black, dashed), but the shape of the peaks has changed, with subsidiary maxima appearing to either side due to the symmetric nature of the two absorbers and their acoustic impedance mismatch with the surrounding media. In (d), the first resonant peak for one (black, dashed) and two (red) absorbers has been shown. With two absorbers, subsidiary peaks appear to either side of the resonant peak, at $\hat{\omega} = \delta\hat{\omega}(= 0.7)$.

If the single 100-nm thick Cr layer in Fig. 6.17c is replaced by two 50nm-thick Cr layers, separated by a single transparent layer of PDMS, then the resultant multilayer structure has both distributed heat sources and a high-reflectance coating and all the layers have a thickness of less than or equal to the acoustic wavelength (Fig. 6.20a). When irradiated by light from the left-hand side, light absorption is greatest in the left-hand absorbing layer and decays according to Beer's law, as shown in Fig. 6.20b.

The performance of the high-reflectance coating (not shown) is the same as it was for the single Cr layer (Fig. 6.18a). However, the corresponding frequency spectrum of the detected signal, shown in red in Fig. 6.20c, has some differences. The stop-bands, or bands of low signal amplitude, between the resonant peaks have flattened compared to the single absorber structure (black) and subsidiary maxima have appeared to either side of the resonant peaks (shown in Fig. 6.20d at $\pi \pm \delta\hat{\omega}$) because, once again, the two-absorber structure is equivalent to a two-stack symmetric multilayer and acts as a half-wave plates at this frequency.

The use of distributed sources has not led to an increase in the amplitude of the detected signal at the resonant frequencies when the optical absorption in the sources has been assumed to follow Beer's law. However, in Chapter 7, the use of optical resonance between the sources and the suitability of Beer's Law will be discussed.

6.4 Summary

In this chapter, acoustic subwavelength structures have been investigated. First, the detected acoustic signal was simulated when the structures were irradiated by an external acoustic source and it was found that:

- a single layer with a quarter-wavelength thickness at a target frequency can be used as an anti-reflection coating. To achieve zero reflectance, the material of the layer must have an acoustic impedance, Z_1, that satisfies the following condition:

  $$Z_1^2 = Z_0 Z_S,$$

  where Z_0 and Z_S are the impedances of the substrates.

- If a material cannot be found to satisfy the zero-reflectance condition, then a symmetric multilayer can be used. Due to its symmetry, an equivalent acoustic impedance, Z_E, and phase thickness, ϕ_E, were derived, using the transfer-matrix method from Chapter 3, such that the equivalent parameters satisfied the conditions for zero-reflectance, rather than the materials themselves.

- High-reflectance coatings can be made from a stack of quarter-wave plates, with alternating high and low acoustic impedance layers. By increasing the number of layers and acoustic impedance mismatch, the amplitude and width of the high reflectance bands was increased.

Then, the two-absorber structure from Chapter 5 was revisited. When irradiated by light in the short-pulse regime, the structure generated an acoustic signal and because all the layers had the same sonic transit time, the frequency spectrum of the detected signal had resonant peaks at odd integer values of π. There was also a low-frequency peak in the spectrum at $\delta\hat{\omega} = 0.13\pi$, which, when previously investigated by Sun et al [23], was approximated using a mass-spring analogy. However, in the context of subwavelength structures, the frequency $\delta\hat{\omega}$ was derived using symmetric multilayers and further anomalies, like the zero between $\delta\hat{\omega}$ and the first harmonic, can explained by complex analysis of zeros and poles of the transfer-matrix when the source terms were included.

Finally, a high-reflectance coating was used to increase the magnitude of the resonant peaks in the spectrum of the detected signal by improving the emission efficiency of the acoustic source in one direction. Left-travelling components were reflected back toward the detector on the right and it was found that:

- using a single interface, the additional reflected components reached the detector and increased the magnitude of the odd resonant peaks by 86%, corresponding to the reflection coefficient at the interface.

- Replacing the single interface with a high reflectance coating increased the magnitude of the odd resonant peaks by about 99%.

- Using two absorbing layers, rather than one, did not change the performance of the high-reflection coating and did not alter the magnitude of the resonant peaks. However, the shape of these peaks was changed, with subsidiary peaks appearing to either side due to the symmetric multilayer effect of the two absorbers.

Thus, a high reflectance coating, comprised of quarter-wave layers of alternating high and low impedance material (in this case, glass and PDMS, respectively), can be used to increase the amplitude of the acoustic signal by about 13% at a target frequency, compared to previously-used methods, which used just a single interface to reflect left-travelling components back toward a detector on the right. The results

shown in this chapter indicate that utilising acoustic resonance will strongly enhance the amplitude of the detected signal at a desired frequency and thus, could improve conversion efficiency of a photoacoustic composite. Such performance enhancements could be useful in applications requiring high-amplitude photoacoustic signals, such as photoacoustic imaging [91–94] and photoacoustic transmitters [49, 50].

In the final example of this chapter, it was shown that there was no change in the amplitude of the resonant peaks in the frequency spectrum of the generated acoustic signal when only a single 100nm-thick chromium layer was used compared to when two 50nm-thick Cr layers were used. However, in reality, the optical absorption in ultrathin layers of chromium depends greatly on the amount of optical reflection in the structure [51]. Therefore, using Beer's Law to approximate light absorption may no longer be adequate. Instead, a more appropriate function that takes into account the reflection of light, must be used. This will be discussed in the following chapter.

Chapter 7

Discussion and future work

In this chapter the work presented in this thesis will be discussed and placed in the context of previous research. The aim of the project was to formulate a one-dimensional model of a multilayered photoacoustic structure with distributed heat sources, using a general heating function that does not limit the absorption profile of any optically-absorbing layers. In order to achieve this, the objectives of the project, given in Chapter 1, were:

1. to derive a one-dimensional model capable of simulating a multilayered structure in which any layer is optically absorbing and the optical absorption can be weak or strong and can include any enhancements to the absorption profile due to interference effects;

2. to formulate the model in the frequency-domain such that the resonant behaviour of the generated acoustic signal can be explored and understood, and;

3. to use the formulated model to optimise the emission efficiency of a photoacoustic structure in one direction using subwavelength layers and careful material selection.

In **Section 7.1**, the first objective will be reviewed and the limitations of the derived model will be discussed, along with areas of future work. In **Section 7.2**, the second objective will be considered and the resonant effects of both light and sound will be discussed. In **Section 7.3**, the third objective will be examined and future work on the use of acoustic subwavelength structures in the short- and long-pulse regime will be presented. Finally, in **Section 7.4**, the identified areas of future work will be recapped.

7.1 Limitations of the model

In Chapter 3, the transfer-matrix method was used to solve the governing photoacoustic equation:

$$\Big[\nabla^2 - \frac{1}{c^2}\frac{\partial^2}{\partial t^2}\Big]p(\mathbf{r},t) = -\frac{\beta}{C_p}\frac{\partial H(\mathbf{r},t)}{\partial t} \tag{2.1}$$

and in Chapters 4 and 5, the simulated photoacoustic signal generated from a structure was verified using data from previous work [15,16,23]. The model derived in this work fulfills the first objective of the project and is capable of simulating the signal generated from a multilayered structure with more than one optically-absorbing layer. Unlike in previous work [23,24], the absorption profile of the layers can be constant, exponentially-decaying, or follow a function of the user's choosing. However, several important assumptions have been made in the formulation of the model and will be considered in the following section.

7.1.1 Heat conduction and viscosity

By solving Eq. 2.1, it has been assumed that the effect of heat conduction and viscosity can be considered negligible and so the equations describing the propagation of heat and elastic waves can be decoupled. The coupled optically-induced thermoelastic equations were considered in work by Hu et al. [24,25], where a model was formulated to calculate the unknown thermal conductivity and thermal contact resistance of a sample from its generated photoacoustic signal. However, for applications outside gas spectroscopy, heat conduction can be neglected, which simplifies the formulation considerably.

In work by Gutierrez-Reyes et al [19], this assumption of negligible heat conduction was considered. The authors compared the simulated photoacoustic signal with and without heat conduction and found that the generated acoustic field could by separated into a photoacoustic response and a photothermal response. The acoustic field associated with the photothermal response was about seven orders of magnitude smaller than the photoacoustic response and arrived at a detector several orders of magnitude later. On this basis, many authors have assumed that heat conduction can be neglected when the sound is generated much faster than the time taken for heat to diffuse away from the light deposition region [5,12,13,15,16,20–22]. The condition for negligible heat conduction can be expressed as [5],

$$l_{aco} >> l_{th}, \tag{7.1}$$

where, $l_{aco} = c\tau_{aco}$ is the length scale for optical absorption, $l_{th} = \sqrt{\alpha_{th}\tau_{aco}}$ is the length scale for thermal diffusivity, $\alpha_{th} = K/(\rho C_p)$ is the thermal diffusivity [m^2 s], and K is the thermal conductivity [W $m^{-1}K^{-1}$].

Recall that, the acoustic relaxation time can be expressed as,

$$\tau_{aco} = \min\left(\frac{d}{c}, \frac{1}{\alpha c}\right), \tag{4.2}$$

where, d, c, and α are the thickness, speed of sound, and optical absorption coefficient of the acoustic source.

Thus, from Eq. 4.2, if the thickness of the absorbing layer, d, is very small, or the absorption coefficient of the material, α, is very high, such that the acoustic relaxation time is very small, then the time scale for thermal diffusion may need to be considered. For example, chromium (Cr) has a thermal diffusivity of about $2.9 \times 10^{-5}m^2s^{-1}$ and a speed of sound of $5940ms^{-1}$ and so the thermal diffusion time is greater than or equal to the acoustic relaxation time when its thickness or its optical penetration depth is less than 5nm. Therefore, for the structures considered in Chapter 6, neglecting heat conduction was acceptable because the thickness and optical penetration depth of the Cr layer were always greater than 5nm. However, photoacoustic composites comprised of ultrathin metallic films are increasingly being fabricated, e.g., the 3nm-thick Cr layer in Ref. [51], and so the effect of heat transport should be considered [103]. Thus, the incorporation of heat transport effects in the transfer-matrix model formulated in this work is a necessary area of future work if the model is used to simulate an ultrathin-film composites. Without including the effects of heat transport, it is suggested that the predicted signals will be larger and arrive at a detector faster than a more realistic formulation.

7.1.2 Acoustic attenuation

When both heat conduction and viscosity effects are neglected, the attenuation of the acoustic signal has not been considered. The attenuation of sound can be included in the model by defining a complex wavenumber, given in Chapter 3 as:

$$k_q \rightarrow k'_q + ik''_q, \tag{3.19}$$

where $k'_q = 2\pi f/c_q$ is the real part, and k''_q is the imaginary part and represents acoustic attenuation [83]. The imaginary part k''_q is a function of the bulk and shear viscosities of the qth layer but can be approximated using the power law [104]:

$$k''_q = k''_{0,q} f^y \quad , \tag{7.2}$$

where $k''_{0,q}$ and y are material properties derived from experimental data. For example in water, $k''_{0,w} = 2.2 \times 10^{-3}$ and $y = 2$ [105] and so the complex wavenumber (Fig. 7.1) is dominated by the imaginary part when:

$$f >> \frac{2\pi}{k''_{0,w} c_w} = 1.9\text{MHz}, \tag{7.3}$$

where the subscript w denotes the material properties of water.

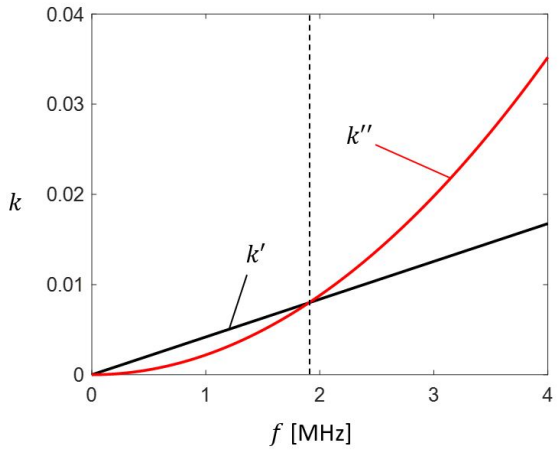


Figure 7.1: Acoustic attenuation: the complex acoustic wave number, k, has a real component, $k' = \frac{2\pi f}{c}$, and an imaginary component, k'', that represents the acoustic attenuation. If the acoustic attenuation is approximated using the power-law (Eq. 7.2) , then the acoustic wave number of water is dominated by the imaginary part at frequencies greater than 1.9MHz.

The damping effect of viscosity and heat conduction will broadened and lower the amplitude of the generated photoacoustic signal as it propagates through water at these frequencies [103]. Therefore, the short- and long-pulse regime, used in this work to calculate the width of the generated acoustic pulse, may no longer be applicable when acoustic attenuation is included and hence, the design of subwavelength features, without knowing the generated acoustic wavelength, will be more difficult.

7.1.3 Acoustic dispersion

The frequency-dependency of other material properties has also not been considered in the model. For example, when designing a high-reflectance coating at a target frequency in Chapter 6, it has been assumed that the material properties of the coating will be the same in the mega-hertz (MHz) frequency range as in the giga-hertz (GHz) range. In Fig. 6.10d, the reflectance was shown for a structure with five

alternating layers of high and low impedance materials, with an acoustic impedance mismatch of 10. Bands of high reflectance were centred around odd integer values of $\hat{\omega} = \pi/2$ ($f = \frac{c}{4d} = 1.2$MHz), where each layer acted as a quarter-wave plate. When the target frequency is increased to 120MHz, the performance of the coating is shown in Fig. 7.2. The two coatings, comprised of the same materials, have the same reflectance profile, centred around the two different target frequencies.

Layer No.	Material	Z/Z_w	d/μm
0	Water	1	-
1(H)	-	10	10
2(L)	Water	1	$10/\sqrt{10}$
S	Water	1	-

Table 7.1: Layer materials and properties of the high-reflectance coating with target frequency, $f_0 = 120$MHz. The structure has five periods ($N = 5$) of layers 1 and 2.

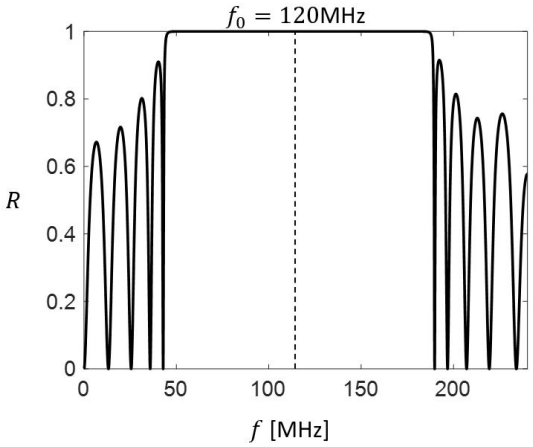


Figure 7.2: Non-dispersive: when the material properties of the high-reflectance coating are assumed to be non-dispersive, the performance of the coating is the same if the target frequency is 1.2MHz (Fig. 6.10d) or 120MHz (shown here).

In reality, however, the speed of sound and density are dispersive properties and thus, rather than being assumed to be constant at all frequencies, a frequency-dependent relationship should be used, i.e.,

$$c = c(\omega), \tag{7.4}$$

particularly in applications operating beyond the mega-hertz frequency range.

Hence, the performance of a structure at 1.2MHz may not be the same as at 120MHz. For the structures given in this work, which operated at relatively low frequencies (e.g., 1-10MHz), the assumptions of non-dispersive and lossless media were appropriate but as applications drive progress into the giga-hertz frequency range, the effect of acoustic attenuation and dispersion should be considered as design modifications may need to be made to ensure the structure still operates with the desired enhancements.

In this section, the attainment of the first objective has been discussed; a one-dimensional model of a photoacoustic structure with distributed heat sources has been successfully formulated. However, there are several limitations of the formulation, which although appropriate for the structures explored in this work, should be considered when simulating ultrathin-film multilayers operating at higher frequency. These are areas of future work and include:

- the incorporation of heat conduction, which would result in less incident optical energy being converted to sound, and hence a lower predicted conversion efficiency;
- the effects of acoustic attenuation, which again, would result in lower predicted conversion efficiencies, as less acoustic energy would reach the detector; and finally,
- the use of frequency-dependent material properties, particularly at higher frequencies, where it cannot be assumed that the speed of sound, or density, of a material is constant.

7.2 Resonant effects

The second objective of the project was to explore the resonant behaviour of the generated acoustic signal. The model in this work was formulated in the frequency-domain, making it ideal for such analysis. In photoacoustics, there can be both optical and acoustical resonance. Optical subwavelength structures have already been shown experimentally to improve the optical absorption of a thin-film photoacoustic structure [50, 51]. In Lee et al [50], an optical resonant cavity was created by sandwiching a transparent PDMS layer between a thin film of chromium (Cr) and aluminium (Al) and the light reflected by the Al layer enhanced the absorption in the thin Cr film. However, the analogous use of acoustic resonance in photoacoustic structures has been less well-researched. In this work, the use of acoustic subwavelength structures to enhance the photoacoustic signal has been investigated.

7.2.1 Acoustic resonance

To study the frequency response of the generated photoacoustic signal, the simplest formulation was to assume that optical absorption followed Beer's law and decayed exponentially across the absorbing layer. This travelling-wave model of light does not

take into account optical interference (to be discussed in the next section). However by using Beer's law, an investigation of the differences in the signals generated by optically-thin and optically-thick absorbers was undertaken, which, to the best of the author's knowledge, has not been done before.

First, the generated acoustic pulse width was calculated. As discussed in Chapter 4, when a photoacoustic structure is irradiated by light with a pulse width, τ_p, in the short-pulse regime, the generated acoustic pulse has a width, T_p, equal to the acoustic relaxation time, τ_{aco}. The acoustic relaxation time depends on the optical thickness, αd_a, of the absorbing layer:

$$\tau_{aco} = \min\left(\frac{d_a}{c_a}, \frac{1}{\alpha c_a}\right). \tag{4.2}$$

and so despite having very different optical absorption profiles (as shown in Fig. 4.1), the acoustic signal generated from an optically-thin layer ($\alpha d_a << 1$) has the same pulse width as that generated from an absorber where $\alpha d_a = 1$. In both cases, the acoustic pulse width is given by:

$$T_p = \tau_{aco} = \frac{d_a}{c_a}, \tag{7.5}$$

where d_a and c_a are the thickness and speed of sound of the absorbing layer.

This is a significant result in the context of acoustic resonant effects because it means that the dimensions of the absorber, d_a, are the same as the acoustic wavelength, $c_a T_p$. Furthermore, if the sonic transit time is the same in every layer, such that

$$\frac{d_a}{c_a} = \frac{d_t}{c_t}, \tag{7.6}$$

where the subscripts a and t denote absorbing and transparent layers, then every qth layer has a thickness equal to the wavelength of sound, i.e.,

$$d_q = c_q T_p, \tag{7.7}$$

and at the same frequency, will all act as a half-wave plate or quarter-wave plate.

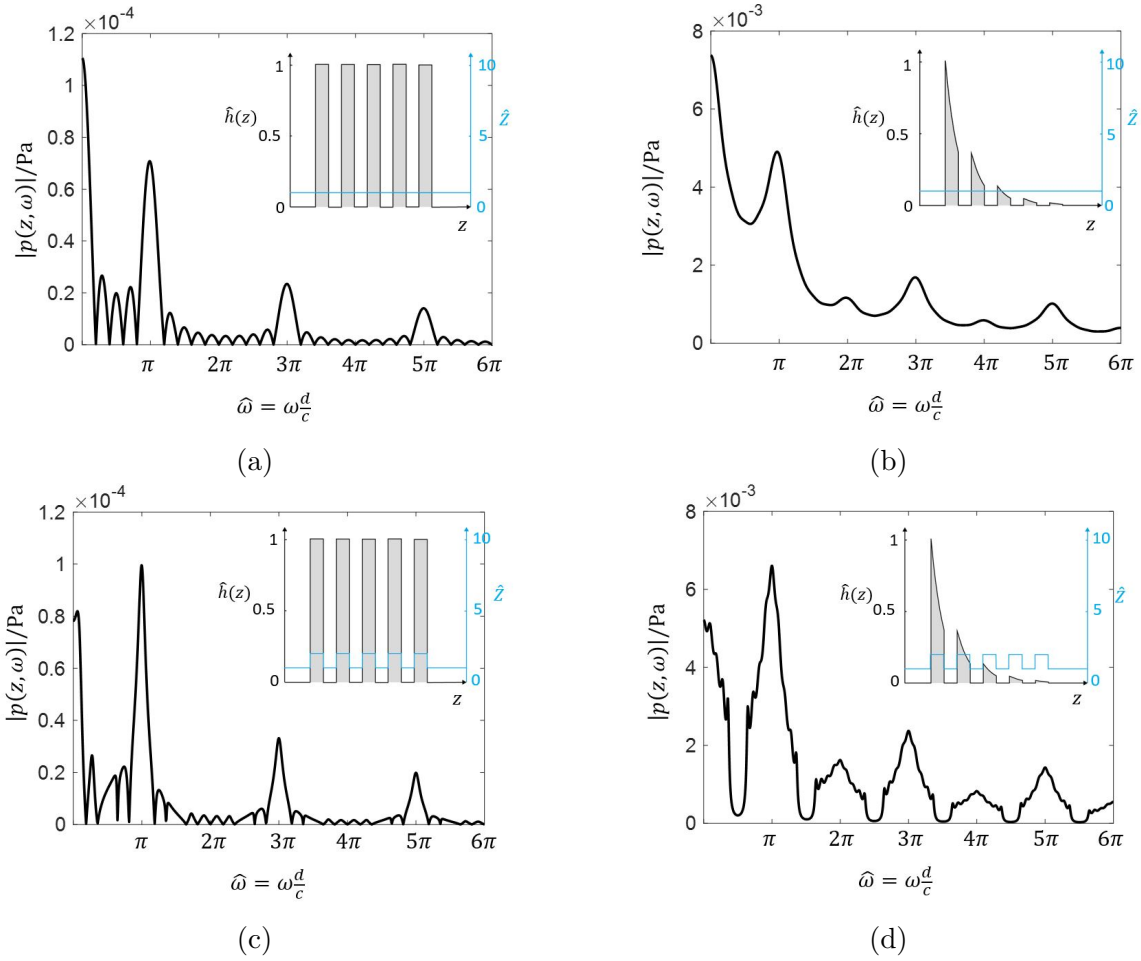


Figure 7.3: Resonant effects from optically-thin (left panel) and optically-thick absorbers (right panel): the frequency spectrum of the generated acoustic signal from five absorbers, separated by five transparent layers, is shown in (a) and (b) when the structure has no mechanical barriers ($\hat{Z} = 1$) and in (c) and (d), when the acoustic impedance mismatch between the absorbing and transparent layers is $\hat{Z} = 2$. Unlike optically-thin absorbers, when the absorbers are optically thick ($\alpha d = 1$), there are additional resonant peaks at even integer values of $\hat{\omega} = \pi$ and increasing the acoustic impedance mismatch from 1 to 2, results in distinct stop bands, centred around integer values of $\hat{\omega} = \pi/2$.

Thus, even without mechanical barriers (and hence, without acoustic reflections), resonant peaks can be observed in the frequency spectrum of the acoustic signal generated by a multilayered structure, shown in Figs. 7.3a and 7.3b. This was observed in work by Sun et al [23] for optically-thin absorbers, but has not been demonstrated for optically-thick absorbers. Importantly, for a structure with optically-thin absorbers, the resonant peaks appear only at odd integer values of the normalised frequency $\hat{\omega} = \pi$, shown in Fig. 7.3a, and the spectrum is zero at even integer values of π with

side lobes in between. However, a structure with optically-thick absorbing layers generates an acoustic signal with resonant peaks at odd and even integer values of π, and any side lobes are suppressed (Fig. 7.3b).

When mechanical barriers were introduced, such that the structure consisted not only of absorbing and transparent layers but also of alternating high and low acoustic impedance materials, the same resonant effects could be seen. Again, optically-thin structures generated signals with resonant peaks only at odd integer values of π, but with mechanical barriers, the shape of the peaks were much sharper, as shown in Fig. 7.3c. Furthermore, the amplitude of the first resonant peak, relative to the zero-frequency peak, increased because reflections inverted the polarity of the signal resulting in large oscillations between positive and negative pressure, with a period of $2T_p$.

Most striking, however, was the distinct bands of low amplitude signal, or stop-bands, produced in the frequency spectrum of the acoustic signal generated from optically-thick absorbers with mechanical barriers, shown in Fig. 7.3d. These stop-bands, and the subsidiary peaks to either side of the resonant peaks, were derived for a structure with just two absorbers in Chapter 6 (but the same derivation applies to the five-absorber structure and its generated signal in Fig. 7.3d). It was shown that each of the alternating layers of high and low acoustic impedance acted as a half-wave plate when the normalised frequency was an integer value of π. Furthermore, the multilayer structure could also be considered as a stack of two symmetric three-layered structures, and that when the thickness of each equivalent symmetric stack was a half-wave plate, a subsidiary peak appeared in the frequency spectrum of the acoustic signal.

Therefore, the performance of multilayered photoacoustic structure can be controlled in the same way as a high-reflectance acoustic coating (also shown in Chapter 6), i.e., increasing the number of alternating layers and the acoustic impedance mismatch between them will result in wider stop-bands and more subsidiary peaks.

The derivation of the position of each subsidiary peak, using the transfer-matrix method described in Chapter 3, is a important improvement on the approximation previously used in work by Sun et al [23]. These features can also be described by analysing the poles and zeros of the transfer-matrix model with and without acoustic sources. Such analysis is an area of further work, however, in short: consider a multilayered structure like the one simulated in Chapter 5, and shown again in Figs. 7.4a and 7.4b, with and without acoustic sources, respectively.

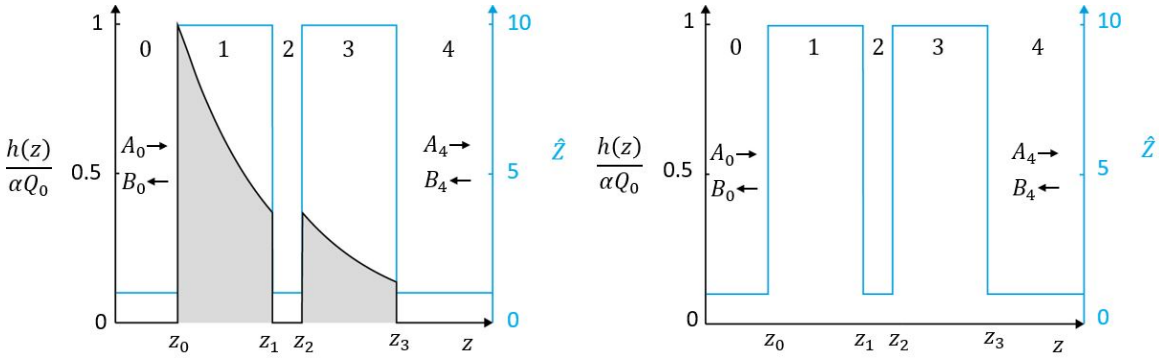


Figure 7.4: The effect of light-generated acoustic sources on the coefficients of the acoustic signal: in (a) the two-absorber structure is irradiated by light and layers 1 and 3 generate an acoustic signal. In (b) the structure has no absorbing layers and is instead irradiated by an external acoustic source from the left. However, the coefficients of the left and right-travelling components in layer 4, A_4 and B_4, respectively, can be calculated by the transfer-matrix method described in Ch. 3 and compared.

The coefficients of the left- and right-travelling components of the acoustic signal in the qth layer, A_q and B_q, respectively, can be derived using the formulation in Chapter 3. If a detector is placed in layer 4, then A_4 and B_4 can be derived in terms of A_0 and B_0. For the structure in (a), which is irradiated by a light source and generates an acoustic signal in layers 1 and 3, the coefficients in layer 4 can be expressed as:

$$\begin{pmatrix} A_4 \\ B_4 \end{pmatrix} = [T_4][T_3][T_2][T_1][T_0] \begin{pmatrix} A_0 \\ B_0 \end{pmatrix} + [T_4]\Big\{(N_3)_{z_3} - [T_3](N_3)_{z_2}\Big\} + [T_4][T_3][T_2]\Big\{(N_1)_{z_1} - [T_1](N_1)_{z_0}\Big\}, \quad (7.8)$$

where, $[T_4]$, $[T_3]$, $[T_2]$, $[T_1]$, and $[T_0]$ are the propagation matrices of layers 4, 3, 2, 1, and 0, respectively, and the acoustic source terms for layer 1 and 3 are N_1 and N_3. Both the source terms and the propagation matrix of any layer were defined in Chapter 3, Eqs. 3.4 and 3.7, respectively. However, for ease, the expression in Eq. 7.8 is written as:

$$\begin{pmatrix} A_4 \\ B_4 \end{pmatrix} = \begin{bmatrix} m_{11}^4 & m_{12}^4 \\ m_{21}^4 & m_{22}^4 \end{bmatrix} \begin{pmatrix} A_0 \\ B_0 \end{pmatrix} + \begin{pmatrix} n_{11}^3 \\ n_{21}^3 \end{pmatrix} + \begin{pmatrix} n_{11}^1 \\ n_{21}^1 \end{pmatrix}, \quad (7.9)$$

where,

$$\begin{bmatrix} m_{11}^4 & m_{12}^4 \\ m_{21}^4 & m_{22}^4 \end{bmatrix} = [T_4][T_3][T_2][T_1][T_0], \quad (7.10)$$

and,

$$\begin{pmatrix} n_{11}^3 \\ n_{21}^3 \end{pmatrix} = [T_4]\Big\{(N_3)_{z_3} - [T_3](N_3)_{z_2}\Big\}, \tag{7.11}$$

and, similarly, the source terms from layer 1 are,

$$\begin{pmatrix} n_{11}^1 \\ n_{21}^1 \end{pmatrix} = [T_4][T_3][T_2]\Big\{(N_1)_{z_1} - [T_1](N_1)_{z_0}\Big\}. \tag{7.12}$$

As described in Chapter 3, there are no left-travelling waves in layer 4 ($B_4 = 0$), and thus, A_4 can be found from Eq. 7.9 and is given by:

$$A_4 = \frac{m_{22}^4(n_{11}^3 + n_{11}^1) - (n_{21}^3 + n_{21}^1)m_{12}^4}{m_{22}^4}. \tag{7.13}$$

However, for the structure in (b), where there are no internal acoustic sources, and an external acoustic source irradiates the structure from the left ($A_0 = 1$), then the coefficients in layer 4 can be found much more straightforwardly:

$$\begin{pmatrix} A_4 \\ B_4 \end{pmatrix} = [T_4][T_3][T_2][T_1][T_0] \begin{pmatrix} A_0 \\ B_0 \end{pmatrix} \tag{7.14}$$

$$= \begin{bmatrix} m_{11}^4 & m_{12}^4 \\ m_{21}^4 & m_{22}^4 \end{bmatrix} \begin{pmatrix} A_0 \\ B_0 \end{pmatrix} \tag{7.15}$$

and, again, $B_4 = 0$ so the right-travelling component of the signal in layer 4 can be expressed as:

$$A_4 = \frac{m_{22}^4 m_{11}^4 - m_{21}^4 m_{12}^4}{m_{22}^4}. \tag{7.16}$$

By inspecting Eqs. 7.13 and 7.16, it can be seen that the poles of the frequency response (the denominators) are the same in both cases, but the zeros (the numerators) are different.

Thus, the signal detected in layer 4 for both structures has the same salient features, but the strength of them is changed by the values of the zeros, as shown in Fig. 7.5. Further investigation into the values of the zeros, and their dependency on optical absorption, is an area of further work and could be a useful tool for the design and analysis of photoacoustic structures.

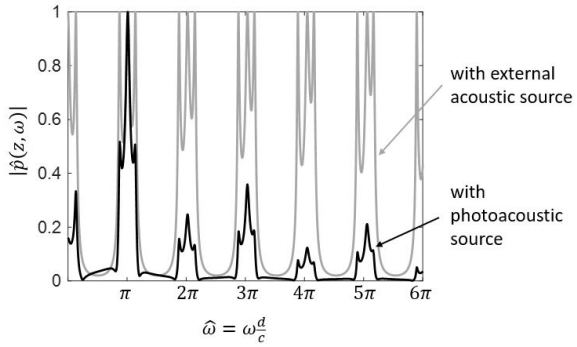


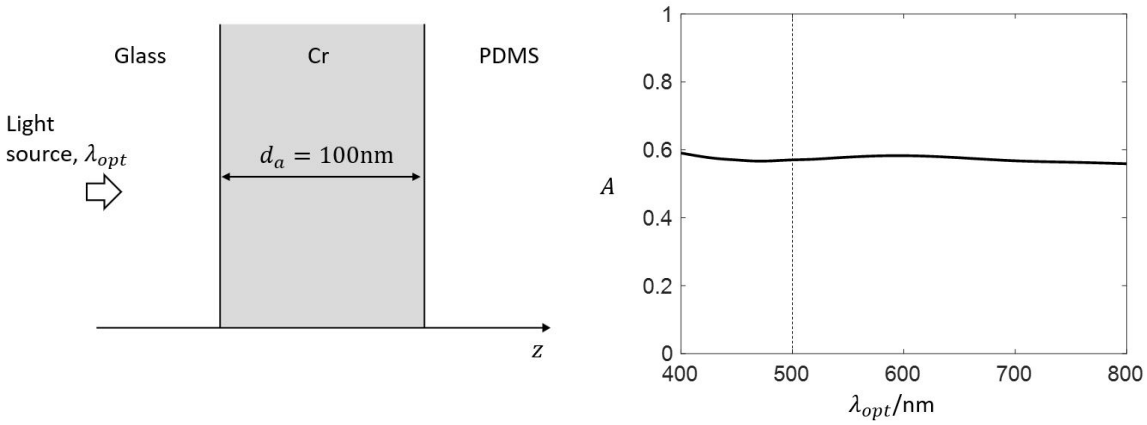
Figure 7.5: The effect of zeros: a structure with acoustic sources has a frequency response function, which describes the coefficients of the acoustic signal in one layer compared to in layer 0, with the same poles but different zeros compared to the frequency response from the equivalent structure with no acoustic sources, which is irradiated by an external acoustic source. As a result, the detected signal in layer 4 has the same salient features, i.e., peaks and troughs at the same frequencies, but the magnitude of the features is different because they are controlled by the zeros.

In this research, the acoustic subwavelength features of a photoacoustic structure have been used to create resonant effects in the generated acoustic signal. Thin-film multilayered structures with optically-thin absorbers have been modelled before [23], but in this work the signals generated by acoustic subwavelength structures with optical absorbers with large optical thicknesses have been simulated and compared. Rather than describing any interference effects using a mass-spring analogy, the position of resonant peaks, stop-bands, and subsidiary peaks in the frequency spectra of the generated signals have been derived by considering the wavelength of the generated acoustic signal and the phase thickness of each layer. Furthermore, the complex analysis of the transfer-matrix describing the frequency response of the acoustic signal has been identified as another method for probing the characteristics of the frequency spectrum and is a useful area of future work. The understanding of these behaviours is crucial to the careful geometric and material design of photoacoustic composites with enhanced conversion efficiency, as will be discussed in the Section 7.3.

7.2.2 Optical resonance

In order to investigate the acoustic resonance effects of the subwavelength structures, the irradiating light was assumed to be a travelling wave and optical reflections were ignored. However, in the following section, the inclusion of optical interference will be discussed.

Consider a single layer of chromium (Cr) with a thickness of 100nm, shown in Fig. 7.6a. When irradiated by light (with wavelength, λ_{opt}) from the left, the far-field optical absorption, A, of the Cr layer does not vary with the wavelength of the incident light, as shown in Fig. 7.6b, and is about 0.6.



(a) (b)

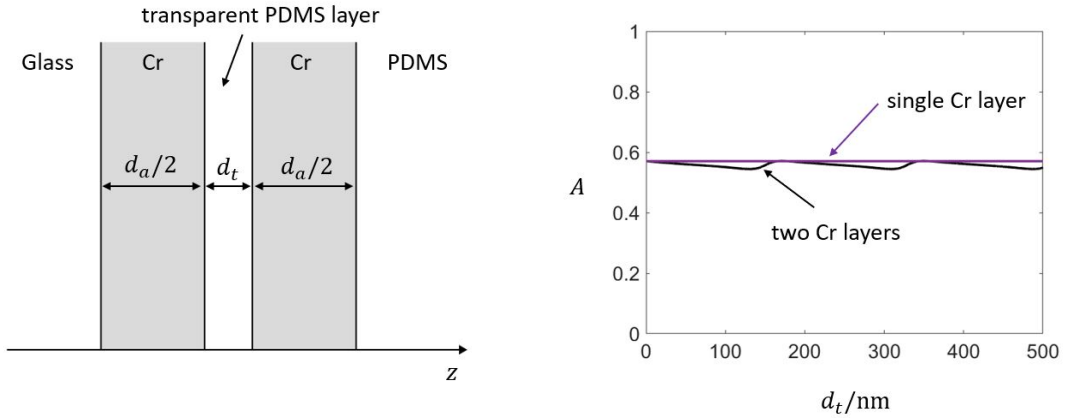
Figure 7.6: Far-field optical absorption: in (a) a single 100nm-thick layer of chromium (Cr) is irradiated by light with wavelength, λ_{opt} from the left. The far-field optical absorption of the structure is shown as a function of λ_{opt} in (b). The optical absorption is flat and $A = 0.57$ when $\lambda_{opt} = 500$nm.

When optical absorption is assumed to follow Beer's Law then an optical absorption coefficient can be defined as:

$$\alpha = \frac{-\ln(1-0.6)}{100 \times 10^{-9}} = 9.2 \times 10^{-6}\text{m}^{-1} \quad , \tag{7.17}$$

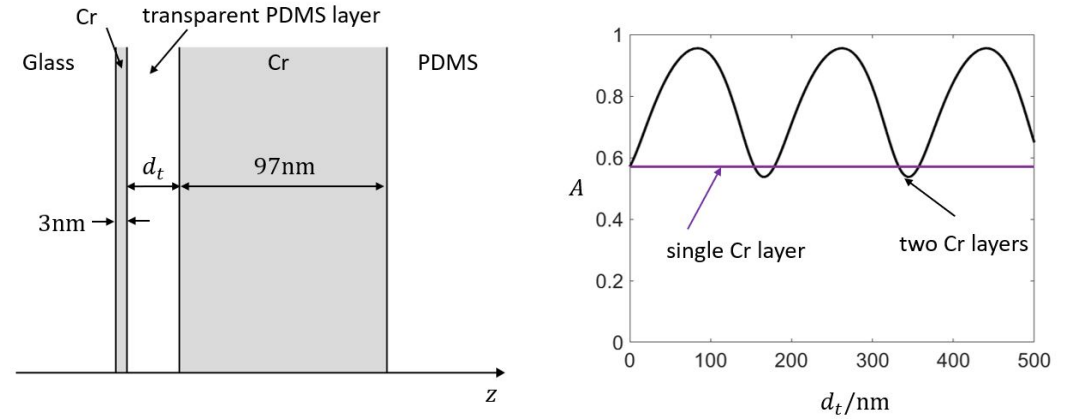
Using this optical absorption coefficient, the same amount of optical absorption occurred in the single layer of 100nm-thick Cr (Fig. 6.17c) as in two 50nm-thick layers of Cr (Fig. 6.20d). However, when the reflection of light is considered, the far-field absorption of the two Cr layers is no longer constant but varies with the thickness of the transparent layer, d_t, between them, due to constructive interference.

When the thickness of the two layers of Cr is 50nm (shown in Fig. 7.7a), the effect of optical interference is small. As shown in Fig. 7.7b, the far-field absorption (black) only drops by 3% (when $d_t = 130 + n180$ nm, where $n = 0, 1$, etc), relative to the far-field absorption from a single 100nm-thick Cr layer (shown in purple). Thus, the effect of optical reflections is small and Beer's law is an appropriate approximation of optical absorption in the two 50nm-thick layers of Cr.



(a) (b)

Figure 7.7: Distributed heat sources with optical reflections: the photoacoustic structure in (a) has two absorbing layers of chromium (Cr) with thicknesses of 50nm, separated by a transparent PDMS layer of thickness, d_t. When the structure is irradiated by light ($\lambda_{opt} = 500$nm) from the left, the far-field absorption, A, in (b) is shown in black. In contrast to the constant absorption of the single 100nm-thick Cr layer (shown in purple), the far-field absorption varies with the thickness of the PDMS layer, d_t. However, absorption drops by only 3% when $d_t = 130, 310, 490$nm, etc.

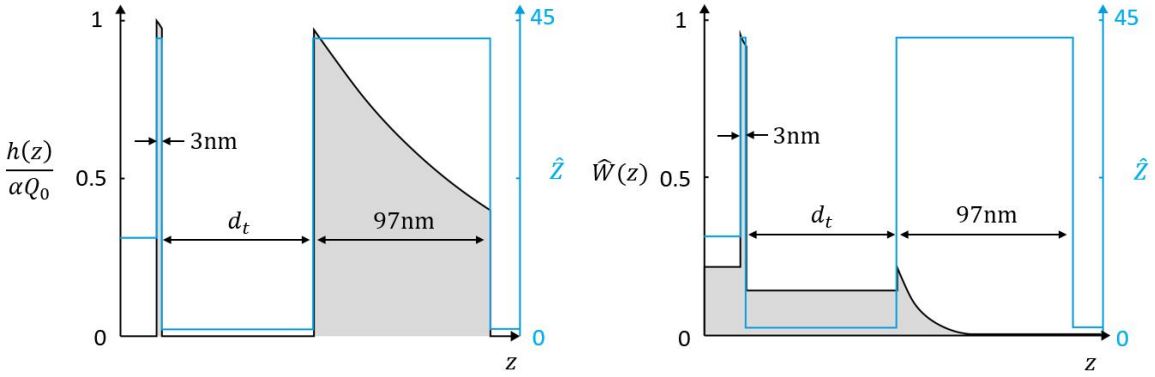


(a) (b)

Figure 7.8: Enhanced optical absorption due to optical interference: In (a) two chromium (Cr) absorbers with thicknesses of 3nm and 97nm, are separated by a transparent PDMS layer with thickness, d_t. When irradiated by light ($\lambda_{opt} = 500$nm) from the left side, the far-field absorption, A, is shown in (b) as a function of d_t (black) and can be compared to the absorption for a single 100nm-thick (purple) at the incident wavelength of light. The single Cr layer has constant far-field absorption but the two Cr layers have a far-field absorption that varies with d_t.

However, when the two Cr layers have thicknesses of 3nm and 97nm, as shown

in Fig. 7.8a, the effect of constructive interference is much more significant and the far-field absorption varies between 54% and 96%, depending on the thickness of the PDMS layer, d_t (Fig. 7.8b). To find the optical energy density in each layer, rather than the far-field optical absorption, the electric and magnetic field vectors have been calculated using the transfer-matrix method derived in Macleod's 'Thin-film Optical Filters' [35]. Fig. 7.9 compares (a) the normalised heating function, $\hat{h}(z)$, when Beer's Law has been assumed and (b) the calculated stored optical energy density, $\hat{W}(z)$, in each layer of the structure. The stored energy density is much lower in the second 97nm-thick Cr layer, which suggests that, by neglecting optical reflections, Beer's law might overestimate the amount of optical absorption in this layer.



(a) (b)

Figure 7.9: Optical energy with and without reflections: for the structure shown in Fig. 7.8a, the heating function, $h(z)$, is shown in (a) in black (shaded) when Beer's Law has been used to approximate optical absorption. In (b), optical reflections have been considered and the normalised stored optical energy density, $\hat{W}(z)$, for the same structure is shown. The acoustic impedance mismatch, $\hat{Z}$, is shown in blue.

One can speculate that, in reality, the acoustic signal generated from the second layer will be much smaller and thinner than the heating function using Beer's Law suggests. The use of the calculated stored energy density as a replacement of the spatial heating function, $h(z)$, is a potentially fruitful area for future work because it includes the effects of optical reflections, and any enhancements in optical absorption this may induce. However, the short- and long-pulse regime may no longer be applicable as it relies on the definition of the optical absorption coefficient, which is not compatible with the inclusion of optical reflections, and thus, a further study of the acoustic wavelength of generated signals would be necessary.

In summary, the effect of optical interference is relatively small when the photoacoustic structure is comprised of two 50nm-thick Cr layers. However, as the layers get thinner, as in Zheng et al's design [51], the stored optical energy density may be a more realistic representation of the spatial heating function of the photoacoustic equation, compared to a simple decaying exponential. In this way, photoacoustic structures could be designed to be optically subwavelength, and hence enhance optical absorption, as well as inducing acoustic resonant effects (objective 2).

7.3 The short- and long-pulse regime

Finally, in Chapter 6 it was shown that an acoustic high-reflectance coating can be used to improve the emission efficiency of a photoacoustic source in one direction (objective 3). In contrast to previous methods used in the literature [51, 76] where emission efficiency was enhanced using an interface with a constant reflectance to reflect left-travelling waves back to a detector on the right, in this work a high reflectance coating with a frequency-dependent reflectance has been used to increase the amplitude of the photoacoustic signal at a target frequency. The photoacoustic source was optically-thin and was irradiated by light in the short-pulse regime and so the generated acoustic signal had a pulse width equal to $T_p = d_a/c_a$, where d_a and c_a were the thickness and speed of sound of the absorber. Hence, the generated signal had an acoustic wavelength in the qth layer of $c_q T_p$. At the same frequency, the layers of the high-reflectance coating had to be a quarter-wavelength thick, i.e.,

$$d_{HR} = \frac{1}{4} c_{HR} T_p = \frac{1}{4} c_{HR} \left(\frac{d_a}{c_a} \right), \tag{7.18}$$

where the subscript HR denotes the layers of the high-reflectance coating and a denotes the absorbing layer.

In this way, the short- and long-pulse regime, which dictates the width of the generated acoustic pulse, T_p, is crucial when designing photoacoustic structures with acoustic resonant effects. In the highly-efficient structure in Chapter 6, the photoacoustic absorber was optically thin and so generated an acoustic pulse with width $T_p = d_a/c_a$ in the short-pulse regime. However, if the optical thickness had been much greater than 1, i.e. $\alpha d >> 1$, then according to the short- and long-pulse regime, the acoustic pulse width would instead be given by:

$$T_p = \tau_{aco} = \frac{1}{\alpha c_a}. \tag{7.19}$$

In order for the high-reflectance coating to remain effective, the thickness of the layers would have to be changed to

$$d_{HR} = \frac{1}{4} c_{HR} T_p = \frac{1}{4} c_{HR} \left(\frac{1}{\alpha c_a} \right). \tag{7.20}$$

In this work, the performance of highly-absorbing ($\alpha d >> 1$) photoacoustic structures was not explored. This is because for a structure with more than one highly-absorbing layer, the absorbing layer closest to the light source absorbs all the incident optical energy and and so is equivalent to a structure with a single absorbing layer, as shown in Fig. 7.10. However, resonant effects can still be induced in the detected acoustic signal because the generated acoustic pulse width is smaller than the dimensions of the structure. Thus, if the absorbing and transparent layers are also alternating layers of high and low acoustic impedance, the generated acoustic signal and its reflections will interfere.

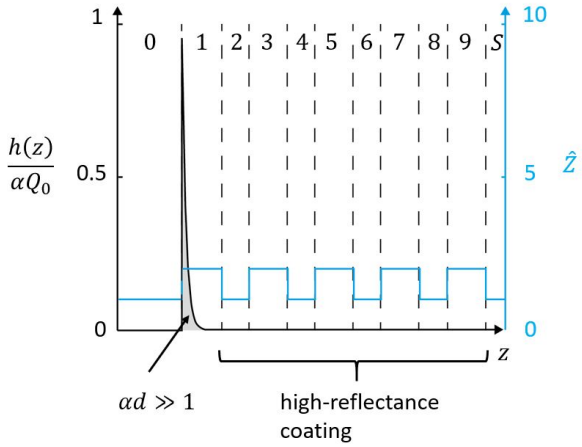


Figure 7.10: Highly-absorbing layers in the short-pulse regime: for a structure with alternating layers of absorbing (odd-layers) and transparent (even-layers) media, with high and low acoustic impedance, if the optical thickness of the absorbing layers is very high ($\alpha d >> 1$), only layer 1, closest to the light source, generates an acoustic signal. However, the other odd layers can still act as an acoustic high-reflectance coating. As a result, resonant peaks will still appear in the frequency spectrum of the detected acoustic signal (not shown). The acoustic impedance mismatch, $\hat{Z}$, is shown in blue and the heating function, when irradiated by light from the left (short-pulse regime), is shown in black (shaded). All the layers have the same sonic transit time.

Structures irradiated in the long-pulse regime were also not modelled in this work. In the long-pulse regime, the acoustic pulse width, T_p, is independent of the geometry of the absorber and is equal to the pulse width of the input light, τ_p. Such structures were used by Lee et al [76] and Rajagopal and Cox [15] to increase the amplitude

of the photoacoustic signal arriving at a detector. The generated acoustic signals were much wider than the dimensions of the structure and so any time delay between reflections was small and the signals overlapped. However, the same acoustic resonant effects, discussed in Chapter 6 in the short-pulse regime, can be induced in structures irradiated by light in the long-pulse regime. For optically-thick absorbers the acoustic relaxation time is given by:

$$\tau_{aco} = 1/(\alpha c_a) \tag{7.21}$$

and so, the acoustic wavelength, cT_p, will be less than or equal to the dimensions of the absorber if the input light source has a pulse width greater than $1/(\alpha c_a)$ but less than d_a/c_a, in other words when:

$$d_a/c_a > \tau_p >> \tau_{aco}. \tag{7.22}$$

Thus, in order to achieve objective 3, the photoacoustic structure does not need to be limited to irradiating light in the short-pulse regime and enhanced emission efficiency can still be induced by a high-reflectance coating. The design of a subwavelength photoacoustic structure in the long-pulse regime is another interesting area of future work because it would increase the number of potential designs, using different laser pulse widths, which may be useful in applications where the pulse of the input light source is non-adjustable.

7.4 Further work

The areas of future work identified in this chapter can be summarised as:

- the inclusion of heat-transport and viscous effects, along with acoustic attenuation, in the formulation derived in this work. All of which may decrease the amplitude of the predicted acoustic signal arriving at a detector, and may broadened the width of the acoustic signal;

- the consideration of dispersive media, i.e., materials that have properties that are frequency-dependent, which could alter the performance of a photoacoustic composites depending on the frequency it is operated at;

- the complex analysis of the transfer-matrix describing the frequency response of the generated acoustic signal. Such analysis may be used to characterise the behaviour of the generated acoustic signal, including the magnitude of resonant peaks in the frequency spectrum and the width of any stop-bands;

- the use of the stored optical energy density as a more realistic heating function in the governing photoacoutic equation, which takes into account optical reflections, and hence can be used to design a photoacoustic composite which combines optical resonance and acoustic resonance to achieve higher photoacoustic conversion efficiency;
- the use of long-pulse input light to irradiate photoacoustic structures with acoustic subwavelength features and the effect it has on the performance of the composite.

7.5 Summary

In this work, a one-dimensional model of a photoacoustic structure has been formulated. The formulation is capable of modelling structures with optically-thin and optically-thick absorbers. However, by retaining a general expression for the heating function, this formulation has the potential to model structures with optical reflections.

In this chapter, the limitations of the model have been identified. These include the neglect of:

- heat transport,
- acoustic attenuation, and
- dispersion.

For the structures examined in this work, it was shown that these assumptions were appropriate. However, as photoacoustic structures get thinner and the desired signals have frequencies in the gigahertz range, such assumptions will be no longer be suitable and thus attempts to include the effects of heat conduction, viscosity, and dispersion in the model should made.

The second objective of this work was to explore and understand the resonant effects of subwavelength structures. In this work, only the *acoustic* resonant effects were investigated. Optical resonant effects were ignored by using Beer's law to approximate the optical absorption. It was found that, in the short-pulse regime, acoustic sources are always subwavelength and hence, if the sonic transit time is the same in both the absorbing and transparent layers, resonant peaks appear in the frequency spectrum of the detected signal. This was shown for optically-thin *and* optically-thick absorbers and the latter has not appeared in previous literature, to the best of the

author's knowledge. Indeed, interesting features appeared in the frequency spectrum of structures with optically-thick absorbers when mechanical barriers were present. There were:

- twice as many resonant peaks, compared to optically-thin absorbers, and
- distinct stop-bands.

These features were explored further by irradiating the equivalent structure without acoustic sources ($\alpha = 0$) with an external acoustic source. Then, comparing the frequency spectra with ($\alpha \neq 0$) and without ($\alpha = 0$) acoustic sources, the effect of the internal photoacoustic sources could be seen. In this chapter, these features were explained by complex analysis of the transfer-matrix with and without source terms. It was demonstrated that for the two structures, the signal detected in the fourth layer had a frequency response function with the same poles (denominators) but different zeros (numerators). As a result, the two frequency spectra of the deteced signal had the same salient features, due to the shared poles, but the strength of the features was different, due to the zeros.

Finally, as an area for further work, the inclusion of optical reflections has been explored. The stored optical energy density has been identified as a potential replacement for Beer's law. Using this function would enable the design of structures that were optically *and* acoustically subwavelength, and thus result in an optimised photoacoustic conversion efficiency.

In Section 7.3, the third objective has been discussed. Using an acoustic high-reflectance coating, a highly-efficient photoacoustic structure has been designed. Contrary to previous work [76], where a single interface was used to reflect left-travelling acoustic components back toward a detector on the right, in this work a stack of quarter-wave plates with alternating high and low acoustic impedance has been used to increase the reflectance from 0.86 to about 1 at a target frequency. As a result, the amplitude of the detected acoustic signal increased by about 15% at the desired frequency, compared to previous methods. Such an enhancement demonstrates the potential benefits of designing photoacoustic composites with acoustic resonant properties.

The structure was irradiated by light in the short pulse regime and had optically thin absorbers. However, the performance of the high-reflectance coating is not limited to these conditions. For example, a structure with optically-thick absorbers irradiated by light in the long-pulse regime can still produce an acoustic pulse with

a wavelength greater than the dimensions of the absorber as long as the input pulse width, τ_p, satisfies the following condition:

$$\frac{d_a}{c_a} > \tau_p >> \frac{1}{\alpha c_a}, \tag{7.23}$$

where d_a, c_a, and α are the thickness, speed of sound, and optical absorption coefficient of the absorbing layer.

Such a structure would generate an acoustic signal with resonant peaks in the frequency spectrum when the sonic transit time in every layer was the same. The design of a photoacoustic structure in the long-pulse regime with subwavelength dimensions would mean that a composite with nanoscale dimensions would not need to be irradiated by light with a picosecond pulse width and thus would increase the number of potential designs for a given application.

In the final section of this chapter, the identified areas of future work have been summarised and in the next chapter, the conclusions of the research project will be given.

Chapter 8

Conclusions

Single photoacoustic sources have been well-modelled because analytical solutions to the governing photoacoustic equation can be derived. Photoacoustic structures with several absorbing layers are more difficult to model. However, experimental results have demonstrated that planar thin-film composites, comprised of absorbing and transparent layers have increased photoacoustic conversion efficiency. Thus, the ability to model such structures and optimise their geometric and material design would be useful.

One-dimensional models of photoacoustic structures with distributed heat sources have already been formulated. There are two well-known ones. The first was formulated by Sun et al [23] and used a transfer-matrix method to solve the photoacoustic equation. The absorbing layers were optically-thin and thus had a uniform absorption profile. The second formulation was derived by Hu et al [24] and, rather than a constant optical absorption profile, the authors limited their work to absorbers with exponentially decaying absorption profiles (optically-thick). They also included the effects of heat transport for the purpose of gas spectroscopy applications and as a result the formulation was much more cumbersome than the one derived in this work.

In this work, the transfer-matrix method has been used to derive a model of the photoacoustic signal generated by a structure in which any layer can be optically absorbing. By means of a heating function, the generality of the model has been retained so that the acoustic sources can be optically-thin, thick, or include the effects of optical interference.

The model was verified using existing analytical models for a single acoustic source and with the results given by Sun et al [23] for optically-thin absorbers. Then, a comparison of the generated acoustic signal, in the time and frequency domain, from optically-thin and optically-thick absorbers was given. It was found that:

- in both cases, the frequency spectrum of the signal generated by a structure with distributed heat sources had resonant peaks even without mechanical barriers (and hence no reflections).

- However, optically-thick absorbers generated an acoustic signal with twice as many resonant peaks and without any side lobes.

- When mechanical barriers were added, the signal from the optically-thick absorbers had distinct stop-bands in its frequency spectrum.

The presence of these stop-bands was investigated by removing the acoustic sources from the structure, i.e. by setting the optical absorption coefficient to zero ($\alpha = 0$), and considering the signal generated from the equivalent structure irradiated by an external acoustic source. By comparing the frequency spectra with ($\alpha \neq 0$) and without absorbers ($\alpha = 0$), it was found that:

- alternating layers of high and low acoustic impedance media all acted as quarter-wave plates, and hence as a high-reflectance coating, at the same frequency if the sonic transit time was the same in every layer (and equal to the generated acoustic pulse width, T_p).

- the symmetry of the quarter-wave plate stack meant that an equivalent acoustic impedance and equivalent phase shift was defined and that when the phase shift across symmetric sections of the structure were equal to π, then subsidiary peaks appeared in the frequency spectrum of the detected signal. To the best of the author's knowledge, this result has not been derived before and is an improvement on the explanation previously given by Sun et al [23], who used a mass-spring analogy to approximate the position of subsidiary peaks.

- Using complex analysis, the poles and zeros of the transfer function describing frequency response of the acoustic signal were used to explain the salient features of the signal's frequency spectrum for a structure where $\alpha = 0$ and $\alpha \neq 0$.

These acoustic resonant effects were used to design a highly-efficient photoacoustic source. Rather than using a single interface to reflect left-travelling waves toward a detector on the right [15, 76], a quarter-wave plate stack was used, which had a reflectance of about 1 at the target frequency. The optimised structure led to about a 15% increase in the amplitude of the detected acoustic signal at the desired frequency and demonstrated the potential benefits of designing photoacoustic composites with

acoustic subwavelength features for the enhancement of the photoacoustic conversion efficiency.

Finally, in Chapter 7, the limitations of the model were given. It was noted that as the layers of the photoacoustic composite get thinner:

- heat-transport should not be neglected because the time for heat diffusion will be comparable to the time for sound generation.
- Acoustic attenuation, due to dispersion and viscous effects, should be considered and would result in a broadened photoacoustic pulse which would not follow the short- and long-pulse regime.

Furthermore, when nanosecond laser pulses are used to generate an acoustic signal from a structure with nanoscale dimensions, neglecting optical reflections, which is implicit when optical absorption is assumed to follow Beer's law, is no longer appropriate. The use of the stored optical energy density was examined as an alternative to an exponentially decaying heating function and it was posited that such a model would enable the design of a photoacoustic structure with enhanced performance due to optical *and* acoustic interference.

It was also shown that a highly-efficient structure is not confined to the short-pulse regime and that resonant effects can be induced using a laser in the long-pulse regime as long as the absorbing layers are optically thick ($\alpha d >> 1$). This increases the flexibility and number of potential designs for a given application.

Lastly, a summary of future work was given, all of which aim to improve the validity of the model formulated in this work in response to the trends in the applications of photoacoustic composites, namely, toward thinner layers, operating at higher frequencies.

Appendix A

Deriving Fourier transform pairs of generated acoustic signals

When the optical thickness, αd, of an absorbing layer is no longer much less than one, the generated acoustic signal is not uniform but varies with time, mirroring the absorption profile of the layer. If the absorption profile, $A(z)$, is assumed to follow Beer's law, then

$$A(z) = e^{-\alpha z} \tag{A.1}$$

Thus, in the time the acoustic signal detected on the opposite of the absorber to the irradiating light source, will take the form, $e^{+\alpha ct}$, where α and c are the optical absorption coefficient and speed of sound in the absorber. However, this is only the case for the duration of acoustic pulse, T_p, at all other times, the acoustic signal is zero. Thus, the acoustic pulse can be expressed mathematically by multiplying the function $e^{+\alpha ct}$ by a rectangular function of width T_p.

A.1 A single exponential pulse

When there is only one absorber, and hence one acoustic pulse, the appropriate segment of the temporal function, $e^{+\alpha ct}$, is extracted using a single rectangular function:

$$f(t) = \Pi\left(\frac{t - (t_0 + T_p/2)}{T_p}\right) e^{+\alpha ct} \tag{A.2}$$

where, in Fig. A.1, t_0 is the time at which $e^{+\alpha ct} = p(z, t_1)$.

The Fourier transform of $f(t)$ is given by:

$$\begin{aligned} F(\omega) &= \int_{t_0}^{t_0+T_p} e^{+\alpha ct} e^{-i\omega t} dt \\ &= \int_{t_0}^{t_0+T_p} e^{-i(\omega+\alpha c)t} dt \end{aligned} \tag{A.3}$$

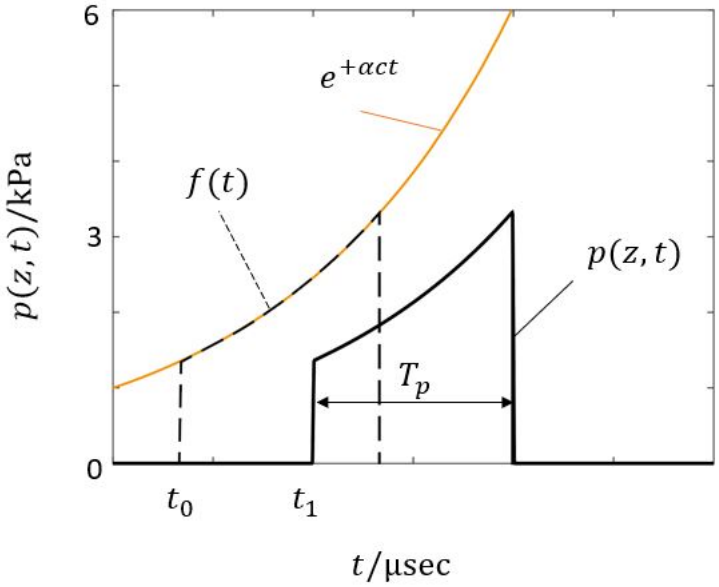


Figure A.1: The profile of the acoustic signal in the time domain, $p(z,t)$, can be considered as a segment of the function, $e^{+\alpha ct}$, with width, T_p, and shifted to ensure $t_0 = t_1$.

To proceed, a change of variable is made, so:

$$u = t - (t_0 + T_p/2)$$

Thus, the integral in Eq. A.3 becomes:

$$\begin{aligned} F(\omega) &= \int_{-T_p/2}^{+T_p/2} e^{-i(\omega+\alpha c)(u+t_0+T_p/2)} du \\ &== T_p e^{-i(\omega+i\alpha c)(t_0+T_p/2)} \frac{\sin((\omega+i\alpha c)T_p/2)}{(\omega+i\alpha c)T_p/2} \end{aligned} \tag{A.4}$$

Furthermore, recall that when $t = t_0$, the function $e^{+\alpha ct}$ was equal to the amplitude of $p(z,t)$ at $t = t_1$, however, this does not mean that $t_0 = t_1$. To ensure that the function $f(t)$ arrives at the detector at the same as $p(z,t)$, it must be shifted by a time $t_1 - t_0$, i.e.,

$$f(t - (t_1 - t_0)) = p(t), \tag{A.5}$$

where $f(t)$ is defined in Eq. A.2.

Thus, using the sifting theorem, the Fourier transforms of $f(t - (t_1 - t_0))$ is given by:

$$f(t - (t_1 - t_0)) \Leftrightarrow F(\omega) e^{-i\omega(t_1 - t_0)}, \tag{A.6}$$

and hence, the frequency spectrum, $p(z,\omega)$ can be expressed as:

$$\begin{aligned} p(z,\omega) &= F(\omega)e^{-i\omega(t_1-t_0)} \\ &= \left[T_p e^{-i(\omega+i\alpha c)(t_0+T_p/2)}\frac{\sin((\omega+i\alpha c)T_p/2)}{(\omega+i\alpha c)T_p/2}\right]e^{-i\omega(t_1-t_0)} \end{aligned} \tag{A.7}$$

and when $t_1 = T_p$ and αc is very small, this expression simplifies to the one found in Eq. 4.10 for a shifted rectangular function.

A.2 Five rectangular pulses

If a single shifted-rectangular pulse is given by:

$$p_{max}\Pi\left(\frac{t-3T_p/2}{T_p}\right) \tag{A.8}$$

where T_p is the width and the pulse is centred at $t = 3T_p/2$, then a train of five rectangular pulses with a period of T can be expressed using superposition as:

$$\begin{aligned} \Pi_5(t) = \Pi\left(\frac{t-3T_p/2}{T_p}\right) + \Pi\left(\frac{t-3T_p/2-T}{T_p}\right) + \Pi\left(\frac{t-3T_p/2-2T}{T_p}\right) \\ + \Pi\left(\frac{t-3T_p/2-3T}{T_p}\right) + \Pi\left(\frac{t-3T_p/2-4T}{T_p}\right). \end{aligned} \tag{A.9}$$

Using the sifting theorem, $\Pi(t-\tau) \Leftrightarrow e^{-i\omega\tau}\hat{\Pi}(\omega)$, the Fourier transform of Eq. A.9 is given by:

$$\hat{\Pi}_5(\omega) = p_{max}T_p e^{-i\omega\frac{3T_p}{2}}\left(1+e^{-i\omega T}+e^{-i\omega 2T}+e^{-i\omega 3T}+e^{-i\omega 4T}\right)\frac{\sin(\omega T_p/2)}{\omega T_p/2}. \tag{A.10}$$

The terms inside the brackets in Eq. A.10 can be expressed using the geometric sum:

$$\begin{aligned} \left(1+e^{-i\omega T}+e^{-i\omega 2T}+e^{-i\omega 3T}+e^{-i\omega 4T}\right) &= \frac{1-e^{-i\omega 5T}}{1-e^{-i\omega T}} \\ &= \frac{e^{-i\omega\frac{5T}{2}}(e^{+i\omega\frac{5T}{2}}-e^{-i\omega\frac{5T}{2}})}{e^{-i\omega\frac{T}{2}}(e^{+i\omega\frac{T}{2}}-e^{-i\omega\frac{T}{2}})} \\ &= e^{-i\omega 2T}\frac{\sin(5\omega T/2)}{\sin(\omega T/2)}, \end{aligned} \tag{A.11}$$

and so Eq. A.10 can be simplified:

$$\hat{\Pi}_5(\omega) = p_{max}T_p e^{-i\omega\frac{3T_p}{2}}\left(e^{-i\omega 2T}\frac{\sin(5\omega T/2)}{\sin(\omega T/2)}\right)\frac{\sin(\omega T_p/2)}{\omega T_p/2}. \tag{A.12}$$

When $T = 2T_p$, as in Fig. 5.3a, Eq. A.12 becomes:

$$\hat{\Pi}_5(\omega) = p_{max} T_p e^{-i\omega \frac{3T_p}{2}} \left(e^{-i\omega 4T_p} \frac{\sin(5\omega T_p)}{\sin(\omega T_p)} \right) \frac{\sin(\omega T_p/2)}{\omega T_p/2} \tag{A.13}$$

Finally, Eq. A.13 can be converted into normalised frequency, $\hat{\omega} = \omega T_p$:

$$\hat{\Pi}_5(\omega) = p_{max} T_p e^{-i\frac{3}{2}\hat{\omega}} \left(e^{-i4\hat{\omega}} \frac{\sin(5\hat{\omega})}{\sin(\hat{\omega})} \right) \frac{\sin(\hat{\omega}/2)}{\hat{\omega}/2} \tag{A.14}$$

A.3 Five exponential pulses

Like in Section B.1 for a single exponential pulse, a train of five exponential pulses can be extracted from the function $e^{+\alpha ct}$ by using five shifted rectangular functions, $\Pi(t/T_p)$, where T_p is the pulse width.

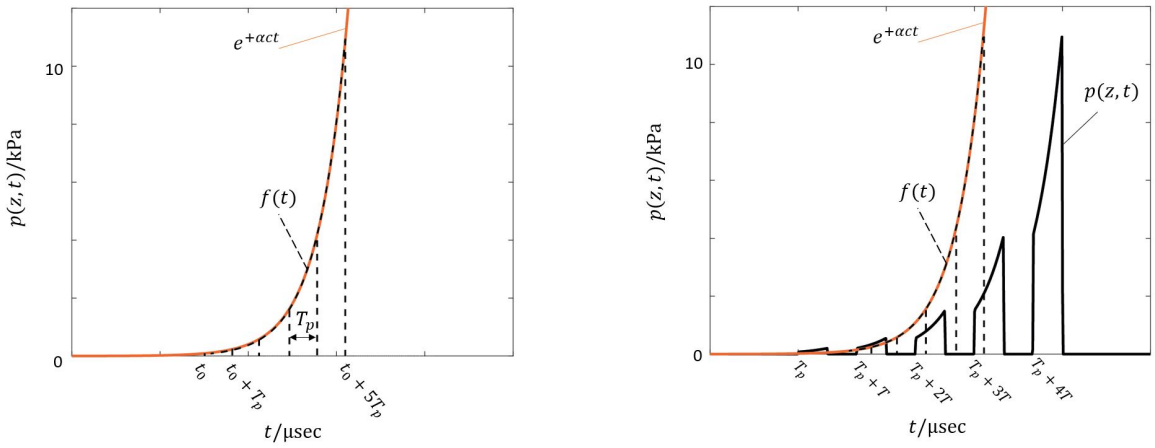


Figure A.2: Segmenting and shifting: in (a) $f(t)$ is the product of the function, $e^{+\alpha c_a t}$, with five shifted rectangular functions to create five sections of equal width. In order to recreate the five pulses in the temporal acoustic signal, $p(z,t)$, in (b), the five sections of $f(t)$ must be shifted to the appropriate time.

First, an expression for the train of exponential pulses in the time domain must be found. Light irradiating the five absorbing layers is in the short pulse regime and so the width of the pulses, T_p, must be equal to the acoustic relaxation time,

$$T_p = \tau_{aco}, \tag{A.15}$$

where, the acoustic relaxation time is defined as $\tau_{aco} = \min\left(\frac{1}{\alpha c_a}, \frac{d_a}{c_a}\right)$, where α, c_a, and d_a are the optical absorption coefficient, speed of sound, and thickness of the

absorber. When the optical thickness is equal to 1 ($\alpha d_a = 1$), the acoustic relaxation time, and hence, the acoustic pulse width, is equal to d_a/c_a. The shifted rectangular functions, used to extract five segments of the function $e^{+\alpha_a c_a t}$, must have a pulse width of

$$T_p = d_a/c_a.$$

Illustrated in Fig. A.2a, the function, $f(t)$, can be expressed as the product of the function $e^{+\alpha c_a t}$ with the sum of five shifted rectangular pulses, i.e.,

$$f(t) = f_1 + f_2 + f_3 + f_4 + f_5, \tag{A.16}$$

where,

$$\begin{aligned}
f_1 &= e^{+\alpha c_a t}\Pi\left(\frac{t-(t_0+T_p/2)}{T_p}\right),\\
f_2 &= e^{+\alpha c_a t}\Pi\left(\frac{t-(t_0+3T_p/2)}{T_p}\right),\\
f_3 &= e^{+\alpha c_a t}\Pi\left(\frac{t-(t_0+5T_p/2)}{T_p}\right),\\
f_4 &= e^{+\alpha c_a t}\Pi\left(\frac{t-(t_0+7T_p/2)}{T_p}\right),\\
f_5 &= e^{+\alpha c_a t}\Pi\left(\frac{t-(t_0+9T_p/2)}{T_p}\right).
\end{aligned} \tag{A.17}$$

and, t_0 is the time at which $e^{+\alpha c_a t} = p(z, t = T_p)$.

The Fourier transform of the f_1 in Eq. A.16 has already been found in Section B.1:

$$e^{+\alpha c_a t}\Pi\left(\frac{t-(t_0+T_p/2)}{T_p}\right) \Leftrightarrow T_p e^{-i(\omega+i\alpha c_a)(t_0+T_p/2)}\frac{\sin\left((\omega+i\alpha c_a)\frac{T_p}{2}\right)}{(\omega+i\alpha c_a)\frac{T_p}{2}}. \tag{A.18}$$

Using the same method, the Fourier transform of f_2 in Eq. A.16 can be found:

$$\mathscr{F}\left(e^{+\alpha c_a t}\Pi\left(\frac{t-(t_0+3T_p/2)}{T_p}\right)\right) = \int_{t_0+T_p}^{t_0+2T_p} e^{+\alpha c_a t}e^{-i\omega t}dt, \tag{A.19}$$

Let the change of variable be: $u = t - (t_0 + 3T_p/2)$, and the integral in Eq. A.19

becomes:

$$\begin{aligned}
&\int_{-T_p/2}^{+T_p/2} e^{-i(\omega+i\alpha c_a)(u+(t_0+3T_p/2))}du \\
&= \frac{e^{-i(\omega+i\alpha c_a)(t_0+3T_p/2)}}{-i(\omega+i\alpha c_a)}\left[e^{-i(\omega+i\alpha c_a)T_p/2} - e^{+i(\omega+i\alpha c_a)T_p/2}\right] \\
&= e^{-i(\omega+i\alpha c_a)(t_0+3T_p/2)}\frac{2\sin\left((\omega+i\alpha c_a)\frac{T_p}{2}\right)}{(\omega+i\alpha c_a)} \\
&= T_p e^{-i(\omega+i\alpha c_a)(t_0+3T_p/2)}\frac{\sin\left((\omega+i\alpha c_a)\frac{T_p}{2}\right)}{(\omega+i\alpha c_a)\frac{T_p}{2}}. \qquad \text{(A.20)}
\end{aligned}$$

In the same fashion, the Fourier transform of the third, fourth, and fifth terms in Eq. A.16 can be found and thus,

$$\mathscr{F}\left(f(t)\right) = F(\omega) = F_1 + F_2 + F_3 + F_4 + F_5, \qquad \text{(A.21)}$$

where,

$$\begin{aligned}
F_1 &= T_p e^{-i(\omega+i\alpha c_a)(t_0+T_p/2)}\frac{\sin\left((\omega+i\alpha c_a)\frac{T_p}{2}\right)}{(\omega+i\alpha c_a)\frac{T_p}{2}}, \\
F_2 &= T_p e^{-i(\omega+i\alpha c_a)(t_0+3T_p/2)}\frac{\sin\left((\omega+i\alpha c_a)\frac{T_p}{2}\right)}{(\omega+i\alpha c_a)\frac{T_p}{2}}, \\
F_3 &= T_p e^{-i(\omega+i\alpha c_a)(t_0+5T_p/2)}\frac{\sin\left((\omega+i\alpha c_a)\frac{T_p}{2}\right)}{(\omega+i\alpha c_a)\frac{T_p}{2}}, \\
F_4 &= T_p e^{-i(\omega+i\alpha c_a)(t_0+7T_p/2)}\frac{\sin\left((\omega+i\alpha c_a)\frac{T_p}{2}\right)}{(\omega+i\alpha c_a)\frac{T_p}{2}}, \\
F_5 &= T_p e^{-i(\omega+i\alpha c_a)(t_0+9T_p/2)}\frac{\sin\left((\omega+i\alpha c_a)\frac{T_p}{2}\right)}{(\omega+i\alpha c_a)\frac{T_p}{2}}.
\end{aligned}$$

However, to recreate $p(z,t)$, each pulse must arrive at the correct time. Importantly, the time at which the function $e^{+\alpha c_a t}$ has the same amplitude that $p(z,t)$ does at time T_p, does not necessarily equal T_p and so each term in Eq. A.16 must be shifted and then the sifting theorem can be used with Eq. A.21 to calculate the

corresponding Fourier transform:

$$\begin{aligned}
f_1(t-(T_p-t_0)) &\Leftrightarrow e^{-i\omega(T_p-t_0)}F_1,\\
f_2(t-((T_p+T)-(t_0+T_p))) &\Leftrightarrow e^{-i\omega((T_p+T)-(t_0+T_p))}F_2,\\
f_3(t-((T_p+2T)-(t_0+2T_p))) &\Leftrightarrow e^{-i\omega((T_p+2T)-(t_0+2T_p))}F_3,\\
f_4(t-((T_p+3T)-(t_0+3T_p))) &\Leftrightarrow e^{-i\omega((T_p+3T)-(t_0+3T_p))}F_4,\\
f_5(t-((T_p+4T)-(t_0+4T_p))) &\Leftrightarrow e^{-i\omega((T_p+4T)-(t_0+4T_p))}F_5.
\end{aligned} \tag{A.22}$$

When $T = 2T_p$, the sum of the five shifted Fourier transforms in Eq. A.22 becomes:

$$\begin{aligned}
F(\omega) = e^{-i\omega(T_p-t_0)}T_p e^{-i(\omega+i\alpha c_a)(t_0+T_p/2)}\frac{\sin\left((\omega+i\alpha c_a)\frac{T_p}{2}\right)}{(\omega+i\alpha c_a)\frac{T_p}{2}}\Bigg(1+e^{-i\omega T_p}e^{-i(\omega+i\alpha c_a)T_p}\\
+e^{-i\omega 2T_p}e^{-i(\omega+i\alpha c_a)2T_p}+e^{-i\omega 3T_p}e^{-i(\omega+i\alpha c_a)3T_p}\\
+e^{-i\omega 4T_p}e^{-i(\omega+i\alpha c_a)4T_p}\Bigg)
\end{aligned} \tag{A.23}$$

The geometric sum can be used to simplify the expression in brackets in Eq. A.23 so that:

$$\begin{aligned}
F(\omega) &= e^{-i\omega(T_p-t_0)}T_p e^{-i(\omega+i\alpha c_a)(t_0+T_p/2)}\frac{\sin\left((\omega+i\alpha c_a)\frac{T_p}{2}\right)}{(\omega+i\alpha c_a)\frac{T_p}{2}}\left(\frac{1-e^{-i\omega 5T_p}e^{-i(\omega+i\alpha c_a)5T_p}}{1-e^{-i\omega T_p}e^{-i(\omega+i\alpha c_a)T_p}}\right)\\
&= e^{-i(4\omega T_p - i\alpha c_a\frac{5T_p}{2})}e^{-i\omega(\frac{3T_p}{2}-t_0)}\frac{\sin\left((\omega+i\alpha c_a)\frac{T_p}{2}\right)}{(\omega+i\alpha c_a)\frac{T_p}{2}}\frac{\sin((\omega+i\frac{\alpha c_a}{2})5T_p)}{\sin((\omega+i\frac{\alpha c_a}{2})T_p)},
\end{aligned} \tag{A.24}$$

which can be expressed in terms of the normalised frequency, $\hat{\omega} = \omega T_p$, i.e.,

$$F(\hat{\omega}) = e^{-i(4\hat{\omega}-i\frac{5}{2}\alpha c_a T_p)}e^{-i\hat{\omega}(\frac{3}{2}-\hat{t}_0)}\frac{\sin\left(\frac{1}{2}(\hat{\omega}+i\alpha c_a T_p)\right)}{\frac{1}{2}(\hat{\omega}+i\alpha c_a T_p)}\frac{\sin(5(\hat{\omega}+i\frac{\alpha c_a T_p}{2}))}{\sin(\hat{\omega}+i\frac{\alpha c_a T_p}{2})}. \tag{A.25}$$

where, $\hat{t}_0 = t_0/T_p$. Recall that, in this example, $T_p = d_a/c_a$ and so the term $\alpha c_a T_p$, which appears repeatedly in Eq. A.25, reduces to:

$$\alpha c_a T_p = \alpha c_a\left(\frac{d_a}{c_a}\right) = \alpha d_a. \tag{A.26}$$

and hence, when the absorbers are optically thin ($\alpha d_a << 1$), the expression in Eq. A.25 tends to the expression found in Eq. A.14 for the Fourier transform of a train of rectangular pulses.

List of Publications

Patterson, I. and Stavrinou, P. (2023). *Photoacoustic signals from thin-film structures with distributed sources.* [Manuscript in Preparation]. Department of Engineering Science, University of Oxford.

This manuscript is largely based on the work from Chapter 2. It describes the formulation of a one-dimensional model of the acoustic signal generated from a multilayered photoacoustic composite with distributed heat sources, without limiting the optical thickness of the absorbing layers.

Patterson, I. and Stavrinou, P. (2023). *Complex Analysis of Distributed Heat Sources.* [Manuscript in Preparation]. Department of Engineering Science, University of Oxford.

This manuscript combines the work on acoustic interference found in Chapters 6 (Sec. 6.2) and 7 (Sec. 7.2.1). It explores the differences in the zeros and poles of the transfer matrix for a multilayered photoacoustic structure with and without distributed heat sources. The relationship between the zeros and the position of subsidiary peaks in the resultant frequency spectrum is investigated.

References

[1] A. Fitzpatrick, A. Singhvi, and A. Arbabian, "An airborne sonar system for underwater remote sensing and imaging," *IEEE Access*, vol. 8, pp. 189945–189959, 2020.

[2] Z. Ji, Y. Fu, J. Li, Z. Zhao, and W. Mai, "Photoacoustic communication from the air to underwater based on low-cost passive relays," *IEEE Communications Magazine*, vol. 59, pp. 140–143, 1 2021.

[3] S. Manohar and D. Razansky, "Photoacoustics: a historical review," *Adv. Opt. Photon.*, vol. 8, pp. 586–617, Dec 2016.

[4] P. Beard, "Biomedical photoacoustic imaging," *Interface Focus*, vol. 1, no. 4, pp. 602–631, 2011.

[5] T. Lee, H. W. Baac, Q. Li, and L. J. Guo, "Efficient photoacoustic conversion in optical nanomaterials and composites," *Advanced Optical Materials*, 2018.

[6] H. W. Baac, J. G. Ok, A. Maxwell, K.-T. Lee, Y.-C. Chen, A. J. Hart, Z. Xu, E. Yoon, and L. J. Guo, "Carbon-nanotube optoacoustic lens for focused ultrasound generation and high-precision targeted therapy.," *Scientific reports*, vol. 2, p. 989, 2012.

[7] S. Noimark, R. J. Colchester, B. J. Blackburn, E. Z. Zhang, E. J. Alles, S. Ourselin, P. C. Beard, I. Papakonstantinou, I. P. Parkin, and A. E. Desjardins, "Carbon-nanotube–pdms composite coatings on optical fibers for all-optical ultrasound imaging," *Advanced Functional Materials*, vol. 26, 2016.

[8] A. D. Silva, C. A. Henriques, D. V. Malva, M. J. Calvete, M. M. Pereira, C. Serpa, and L. G. Arnaut, "Photoacoustic generation of intense and broadband ultrasound pulses with functionalized carbon nanotubes," *Nanoscale*, vol. 12, pp. 20831–20839, 10 2020.

[9] Y. Hou, J.-S. Kim, S. Ashkenazi, M. O'Donnell, and L. J. Guo, "Optical generation of high frequency ultrasound using two-dimensional gold nanostructure," *Applied Physics Letters*, vol. 89, p. 093901, 8 2006.

[10] Y. Hou, J.-S. Kim, S. Ashkenazi, S.-W. Huang, L. J. Guo, and M. O'donnell, "Broadband all-optical ultrasound transducers," 2007.

[11] N. Wu, Y. Tian, X. Zou, V. Silva, A. Chery, and X. Wang, "High-efficiency optical ultrasound generation using one-pot synthesized polydimethylsiloxane-gold nanoparticle nanocomposite," *Journal of the Optical Society of America B*, vol. 29, p. 2016, 8 2012.

[12] N. Baddour and A. Mandelis, "The effect of acoustic impedance on subsurface absorber geometry reconstruction using 1d frequency-domain photoacoustics," *Photoacoustics*, vol. 3, pp. 132–142, 12 2015.

[13] E. Svanström, T. Linder, and T. Löfqvist, "Analytical one-dimensional model for laser-induced ultrasound in planar optically absorbing layer," *Ultrasonics*, vol. 54, pp. 888–893, 3 2014.

[14] Q. Shan, A. Kuhn, P. A. Payne, and R. J. Dewhurst, "Characterisation of laser-ultrasound signals from an optical absorption layer within a transparent fluid," *Ultrasonics*, vol. 34, pp. 629–639, 8 1996.

[15] S. Rajagopal and B. T. Cox, "Modelling laser ultrasound waveforms: The effect of varying pulse duration and material properties," *The Journal of the Acoustical Society of America*, vol. 149, p. 2040, 3 2021.

[16] D. Cywiak, M. D. Barreiro-Argüelles, M. Cywiak, A. Landa-Curiel, C. Garcia-Segundo, and G. Gutierrez-Juárez, "A one-dimensional solution of the photoacoustic wave equation and its relationship with optical absorption," *International Journal of Thermophysics*, vol. 34, pp. 1473–1480, 10 2013.

[17] G. J. Diebold, M. I. Khan, and S. M. Park, "Photoacoustic "signatures" of particulate matter: Optical production of acoustic monopole radiation," *Science*, vol. 250, pp. 101–104, 10 1990.

[18] G. J. Diebold, T. Sun, and M. I. Khan, "Photoacoustic monopole radiation in one, two, and three dimensions," *Physical Review Letters*, vol. 67, pp. 3384–3387, 12 1991.

[19] E. Gutiérrez-Reyes, C. García-Segundo, A. García-Valenzuela, R. Ortega, C. Buj, and F. Filbir, "Heat transport considerations in the mathematical analysis of the photoacoustic and photothermal effects," *Journal of Physics Communications*, vol. 3, p. 085007, 8 2019.

[20] S. M. Park, M. I. Khan, H. Z. Cheng, and G. J. Diebold, "Photoacoustic effect in strongly absorbing fluids," *Ultrasonics*, vol. 29, pp. 63–67, 1 1991.

[21] F. Herrerías-Azcué, A. González-Vega, J. Torres-Arenas, and G. Gutiérrez-Juárez, "Solution for the photoacoustic wave equation with a single spatial degree of freedom, beer's law absorption of radiation and mechanical barriers," *Modern Physics Letters B*, 2013.

[22] E. Gutiérrrez-Reyes, C. García-Segundo, A. García-Valenzuela, B. Reyes-Ramírez, G. Gutiérrez-Juárez, and A. Guadarrama-Santana, "Analysis of the transfer function for layered piezoelectric ultrasonic sensors," *AIP Advances*, vol. 7, p. 065106, 6 2017.

[23] T. Sun, H. X. Chen, and G. J. Diebold, "Distributed source photoacoustic generation of ultrasound," *Ultrasonics*, vol. 32, pp. 265–270, 1 1994.

[24] H. Hu, X. Wang, and X. Xu, "Generalized theory of the photoacoustic effect in a multilayer material," *Journal of Applied Physics*, vol. 86, p. 3953, 9 1999.

[25] H. Hu, W. Zhang, J. Xu, and Y. Dong, "General analytical solution for photoacoustic effect with multilayers," *Applied Physics Letters*, vol. 92, p. 014103, 1 2008.

[26] S. Kang, Y. Yoon, J. Kim, and W. Kim, "Thermoelastic response of thin metal films and their adjacent materials," *Applied Physics Letters*, vol. 102, p. 021908, 1 2013.

[27] A. Rosencwaig and A. Gersho, "Theory of the photoacoustic effect with solids," *Journal of Applied Physics*, vol. 47, no. 1, pp. 64–69, 1976.

[28] L. B. Kreuzer and C. K. N. Patel, "Nitric oxide air pollution: Detection by optoacoustic spectroscopy," *Science*, vol. 173, no. 3991, pp. 45–47, 1971.

[29] A. Rosencwaig, "Photoacoustic spectroscopy of solids," *Optics Communications*, vol. 7, no. 4, pp. 305 – 308, 1973.

[30] M. W. Schellenberg and H. K. Hunt, "Hand-held optoacoustic imaging: A review," *Photoacoustics*, vol. 11, pp. 14–27, 9 2018.

[31] E. Biagi, F. Margheri, and D. Menichelli, "Efficient laser-ultrasound generation by using heavily absorbing films as targets," *IEEE Transactions on Ultrasonics, Ferroelectrics and Frequency Control*, vol. 48, pp. 1669–1680, 2001.

[32] D. Vella, A. Mrzel, A. Drnovšek, V. Shvalya, and M. Jezeršek, "Ultrasonic photoacoustic emitter of graphene-nanocomposites film on a flexible substrate," *Photoacoustics*, vol. 28, p. 100413, 12 2022.

[33] X. Du, J. Li, G. Niu, J.-H. Yuan, K.-H. Xue, M. Xia, W. Pan, X. Yang, B. Zhu, and J. Tang, "Lead halide perovskite for efficient optoacoustic conversion and application toward high-resolution ultrasound imaging," *Nature Communications 2021 12:1*, vol. 12, pp. 1–9, 6 2021.

[34] L. I. Epstein, "The design of optical filters," *JOSA, Vol. 42, Issue 11, pp. 806-810*, vol. 42, pp. 806–810, 11 1952.

[35] H. A. Macleod, "Thin-film optical filters," *Thin-Film Optical Filters, Fourth Edition*, pp. 1–782, 1 2010.

[36] W. Weinstein, "Computations in thin film optics," *Vacuum*, vol. 4, pp. 3–19, 1 1954.

[37] Y. Liu, Y. Cai, Y. Zhang, A. Tovstopyat, S. Liu, and C. Sun, "Materials, design, and characteristics of bulk acoustic wave resonator: A review," *Micromachines*, vol. 11, 7 2020.

[38] Y. Zou, C. Gao, J. Zhou, Y. Liu, Q. Xu, Y. Qu, W. J. Liu, J. B. W. Soon, Y. Cai, and C. Sun, "Aluminum scandium nitride thin-film bulk acoustic resonators for 5g wideband applications," *Microsystems Nanoengineering*, vol. 8, 12 2022.

[39] N. D. Lanzillotti-Kimura, A. Fainstein, B. Jusserand, A. Lemaître, O. Mauguin, and L. Largeau, "A periodic thin film filters for acoustic phonons," *Journal of Physics: Conference Series*, vol. 92, 12 2007.

[40] P. Basséras, S. M. Gracewski, G. W. Wicks, and R. J. Miller, "Optical generation of high-frequency acoustic waves in gaas/alxga1xas periodic multilayer structures," *Journal of Applied Physics*, vol. 75, p. 2761, 6 1998.

[41] W. Maryam, A. V. Akimov, R. P. Campion, and A. J. Kent, "Dynamics of a vertical cavity quantum cascade phonon laser structure," *Nature Communications 2013 4:1*, vol. 4, pp. 1–6, 7 2013.

[42] F. Gao, R. Kishor, X. Feng, S. Liu, R. Ding, R. Zhang, and Y. Zheng, "An analytical study of photoacoustic and thermoacoustic generation efficiency towards contrast agent and film design optimization," *Photoacoustics*, 2017.

[43] S. Noimark, R. J. Colchester, R. K. Poduval, E. Maneas, E. J. Alles, T. Zhao, E. Z. Zhang, M. Ashworth, E. Tsolaki, A. H. Chester, N. Latif, S. Bertazzo, A. L. David, S. Ourselin, P. C. Beard, I. P. Parkin, I. Papakonstantinou, and A. E. Desjardins, "Polydimethylsiloxane composites for optical ultrasound generation and multimodality imaging," *Advanced Functional Materials*, vol. 28, p. 1704919, 2 2018.

[44] T. Buma, M. Spisar, and M. O'Donnell, "High-frequency ultrasound array element using thermoelastic expansion in an elastomeric film," *Applied Physics Letters*, vol. 79, pp. 548–550, 7 2001.

[45] W. Huang, W. Y. Chang, J. Kim, S. Li, S. Huang, and X. Jiang, "A novel laser ultrasound transducer using candle soot carbon nanoparticles," *IEEE Transactions on Nanotechnology*, vol. 15, pp. 395–401, 5 2016.

[46] H. W. Baac, J. G. Ok, T. Lee, and L. J. Guo, "Nano-structural characteristics of carbon nanotube-polymer composite films for high-amplitude optoacoustic generation," *Nanoscale*, vol. 7, pp. 14460–14468, 9 2015.

[47] R. J. Colchester, C. A. Mosse, D. S. Bhachu, J. C. Bear, C. J. Carmalt, I. P. Parkin, B. E. Treeby, I. Papakonstantinou, and A. E. Desjardins, "Laser-generated ultrasound with optical fibres using functionalised carbon nanotube composite coatings," *Applied Physics Letters*, vol. 104, p. 173502, 4 2014.

[48] B. Y. Hsieh, J. Kim, J. Zhu, S. Li, X. Zhang, and X. Jiang, "A laser ultrasound transducer using carbon nanofibers-polydimethylsiloxane composite thin film," *Applied Physics Letters*, vol. 106, 1 2015.

[49] S. H. Lee, M. A. Park, J. J. Yoh, H. Song, E. Y. Jang, Y. H. Kim, S. Kang, and Y. S. Yoon, "Reduced graphene oxide coated thin aluminum film as an optoacoustic transmitter for high pressure and high frequency ultrasound generation," *Applied Physics Letters*, vol. 101, 12 2012.

[50] T. Lee and L. J. Guo, "Highly efficient photoacoustic conversion by facilitated heat transfer in ultrathin metal film sandwiched by polymer layers," *Advanced Optical Materials*, vol. 5, 2017.

[51] C. Zheng, H. Zhu, Z. Xu, R. K. Sinha, Q. Li, and P. Ghosh, "High-efficient photoacoustic generation with an ultrathin metallic multilayer broadband absorber," *Optics Express*, vol. 29, p. 8490, 3 2021.

[52] D. Lee, D. M. Nguyen, and J. Rho, "Acoustic wave science realized by metamaterials," *Nano Convergence*, vol. 4, 2017.

[53] M. Maliński, "Influence of internal reflections of light on spectral characteristics of photoacoustic signal," *Opto-Electronics Review*, vol. 18, pp. 474–477, 12 2010.

[54] Y. Wang, K. Deng, S. Xu, C. Qiu, H. Yang, and Z. Liu, "Applications of antireflection coatings in sonic crystal-based acoustic devices," *Physics Letters A*, vol. 375, pp. 1348–1351, 3 2011.

[55] C. Peng, M. Chen, J. B. Spicer, and X. Jiang, "Acoustics at the nanoscale (nanoacoustics): A comprehensive literature review.: Part i: Materials, devices and selected applications," *Sensors and actuators. A, Physical*, vol. 332, 12 2021.

[56] S.-S. Li, H.-C. Feng, H. T. Liu, al, Q. Wang, Y. Zou, J. Zhang, S. Son, M. Kim, L. C. Ho, K. Song, J.-H. Kwak, J. J. Park, and S. Hur, "Acoustic metasurfaces for efficient matching of non-contact ultrasonic transducers," *Smart Materials and Structures*, vol. 30, p. 085011, 6 2021.

[57] T. Lee and H. Iizuka, "Sound propagation across the air/water interface by a critically coupled resonant bubble," *PHYSICAL REVIEW B*, vol. 102, p. 104105, 2020.

[58] S. Qu, N. Gao, A. Tinel, B. Morvan, V. Romero-García, J. P. Groby, and P. Sheng, "Underwater metamaterial absorber with impedance-matched composite," *Science Advances*, vol. 8, p. 4206, 5 2022.

[59] E. Bok, J. J. Park, H. Choi, C. K. Han, O. B. Wright, and S. H. Lee, "Metasurface for water-to-air sound transmission," 2018.

[60] K. Im and Q. H. Park, "Omni-directional and broadband acoustic anti-reflection and universal acoustic impedance matching," *Nanophotonics*, vol. 11, pp. 2191–2198, 4 2022.

[61] A. Huynh, N. D. Lanzillotti-Kimura, B. Jusserand, B. Perrin, A. Fainstein, M. F. Pascual-Winter, E. Peronne, and A. Lemaître, "Subterahertz phonon dynamics in acoustic nanocavities," *Physical Review Letters*, vol. 97, p. 115502, 9 2006.

[62] I. Koń, F. Domingue, A. Reinhardt, H. Jacquinot, M. Borel, M. Gorisse, G. Parat, F. Casset, D. Pellissier-Tanon, J. F. Carpentier, L. Buchaillot, and B. Dubus, "Guided acoustic wave resonators using an acoustic bragg mirror," *Applied Physics Letters*, vol. 96, p. 223504, 6 2010.

[63] Y. F. Wang, Y. Z. Wang, B. Wu, W. Chen, and Y. S. Wang, "Tunable and active phononic crystals and metamaterials," *Applied Mechanics Reviews*, vol. 72, 7 2020.

[64] Z. Liu, X. Zhang, Y. Mao, Y. Y. Zhu, Z. Yang, C. T. Chan, and P. Sheng, "Locally resonant sonic materials," *Science*, vol. 289, pp. 1734–1736, 9 2000.

[65] A. J. Kent, A. V. Akimov, D. J. Farmer, J. Bailey, J. S. Sharp, and N. A. Gippius, "High-frequency acousto-optic effects in bragg reflectors," *Optics Express, Vol. 22, Issue 12, pp. 15218-15231*, vol. 22, pp. 15218–15231, 6 2014.

[66] M. Shen and W. Cao, "Acoustic bandgap formation in a periodic structure with multilayer unit cells," *Journal of Physics D: Applied Physics*, vol. 33, p. 1150, 5 2000.

[67] B. Xiong, C.-Y. Li, H. Jing, J. He, M. Wang, R. Peng, Y. Zhou, R. Peng, M. Wang, and M. Wang, "Metasurface-assisted broadband optical absorption in ultrathin perovskite films," *Optics Express, Vol. 29, Issue 12, pp. 19170-19182*, vol. 29, pp. 19170–19182, 6 2021.

[68] T. Lee and H. Iizuka, "Heavily overdamped resonance structurally engineered in a grating metasurface for ultra-broadband acoustic absorption," *Applied Physics Letters*, vol. 113, p. 101903, 9 2018.

[69] V. G. Veselago, "The electrodynamics of substances with simultaneously negative values of ϵ and ," *Soviet Physics Uspekhi*, vol. 10, pp. 509–514, 4 1968.

[70] A. J. Ward and J. B. Pendry, "Refraction and geometry in maxwell's equations," *Journal of Modern Optics*, vol. 43, pp. 773–793, 1996.

[71] P. N. Stavrinou and L. Solymar, "The propagation of electromagnetic power through subwavelength slits in a metallic grating," *Optics Communications*, vol. 206, pp. 217–223, 6 2002.

[72] D. R. Smith, J. B. Pendry, and M. C. Wiltshire, "Metamaterials and negative refractive index," *Science*, vol. 305, pp. 788–792, 8 2004.

[73] R. B. Greegor, C. G. Parazzoli, J. A. Nielsen, M. A. Thompson, M. H. Tanielian, and D. R. Smith, "Simulation and testing of a graded negative index of refraction lens," *Applied Physics Letters*, vol. 87, 8 2005.

[74] B. Wood, J. B. Pendry, and D. P. Tsai, "Directed subwavelength imaging using a layered metal-dielectric system," *Physical Review B*, vol. 74, p. 115116, 9 2006.

[75] J. B. Pendry, D. Schurig, and D. R. Smith, "Controlling electromagnetic fields," *Science*, vol. 312, pp. 1780–1782, 6 2006.

[76] T. Lee, Q. Li, and L. J. Guo, "Out-coupling of longitudinal photoacoustic pulses by mitigating the phase cancellation," *Scientific Reports*, vol. 6, pp. 1–9, 2 2016.

[77] V. E. Gusev, A. A. Karabutov, V. E. Gusev, and A. A. Karabutov, "Laser optoacoustics," *STIA*, vol. 93, p. 16842, 1991.

[78] M. L. Khan, T. Sun, and G. J. Diebold, "Photoacoustic waves generated by absorption of laser radiation in optically thin layers," *Journal of the Acoustical Society of America*, vol. 93, pp. 1417–1425, 3 1993.

[79] Z. Bozóki, A. Miklós, and D. Bicanic, "Photothermoelastic transfer matrix," *Applied Physics Letters*, vol. 64, pp. 1362–1364, 3 1994.

[80] T. Sun and G. J. Diebold, "Generation of ultrasonic waves from a layered photoacoustic source," *Nature*, vol. 355, pp. 806–808, 1992.

[81] B. E. Treeby and B. T. Cox, "k-wave: Matlab toolbox for the simulation and reconstruction of photoacoustic wave fields," *Journal of biomedical optics*, vol. 15, p. 021314, 2010.

[82] J. Li, Z. Wang, L. Jiang, Z. Yu, X. Ge, J. Ou-Yang, X. Yang, X. Tian, H. Tian, and B. Zhu, "High efficiency and anomalous photoacoustic behavior in vertical cnts array," *Energy Environmental Materials*, 1 2022.

[83] B. G. Martin, "Theory of the acoustical properties of symmetric multilayer structures," *Journal of Applied Physics*, vol. 66, pp. 1931–1934, 9 1989.

[84] I. G. Calasso, W. Craig, and G. J. Diebold, "Photoacoustic point source," *Physical Review Letters*, vol. 86, pp. 3550–3553, 4 2001.

[85] A. D. Pierce, *Acoustics: An Introduction to Its Physical Principles and Applications*. Springer International Publishing, 3 ed., 2019.

[86] T. M. Inc., "Matlab version: 9.13.0 (r2022b)," 2022.

[87] C. Shannon, "Communication in the presence of noise," *Proceedings of the IRE*, vol. 37, pp. 10–21, jan 1949.

[88] A. Prost, F. Poisson, and E. Bossy, "Photoacoustic generation by a gold nanosphere: From linear to nonlinear thermoelastics in the long-pulse illumination regime," *Physical Review B - Condensed Matter and Materials Physics*, vol. 92, 9 2015.

[89] R. N. Bracewell, *The Fourier Transform and Its Applications*. McGraw-Hill, 1965.

[90] T. Lee, J. G. Ok, L. J. Guo, and H. W. Baac, "Low f-number photoacoustic lens for tight ultrasonic focusing and free-field micro-cavitation in water," *Applied Physics Letters*, vol. 108, 3 2016.

[91] D. M. McCann and M. C. Forde, "Review of ndt methods in the assessment of concrete and masonry structures," *NDT and E International*, vol. 34, pp. 71–84, 2001.

[92] M. Xu and L. V. Wang, "Photoacoustic imaging in biomedicine," *Review of Scientific Instruments*, vol. 77, 2006.

[93] D. Kim, M. Ye, and C. P. Grigoropoulos, "Pulsed laser-induced ablation of absorbing liquids and acoustic-transient generation," *Applied Physics A: Materials Science and Processing*, vol. 67, pp. 169–181, 1998.

[94] A. Agarwal, S. W. Huang, M. O'Donnell, K. C. Day, M. Day, N. Kotov, and S. Ashkenazi, "Targeted gold nanorod contrast agent for prostate cancer detection by photoacoustic imaging," *Journal of Applied Physics*, vol. 102, 2007.

[95] B. G. Martin, "Antireflection properties of a graded-impedance stack of acoustical symmetric multilayers," *Journal of Applied Physics*, vol. 71, pp. 2549–2551, 3 1992.

[96] U. Schallenberg, "Design principles for broadband ar coatings," *https://doi.org/10.1117/12.797708*, vol. 7101, pp. 68–75, 9 2008.

[97] B. G. Martin, "Theory of the acoustical properties of multilayer and superlattice structures using an optical approach," *The Journal of the Acoustical Society of America*, vol. 95, pp. 1658–1660, 3 1994.

[98] B. G. Martin, "Acoustical properties of symmetric multilayers," *The Journal of the Acoustical Society of America*, vol. 91, pp. 1469–1473, 3 1992.

[99] B. G. Martin, Z. Y. Cheng, and C. C. Lee, "Theory of symmetric multilayer structures as layer replacements for chebyshev acoustic antireflection coatings," *The Journal of the Acoustical Society of America*, vol. 87, pp. 193–200, 1 1990.

[100] M. Born and E. Wolf, "Elements of the theory of interference and interferometers," *Principles of Optics*, pp. 256–369, 1 1980.

[101] P. Yeh, *Optical waves in layered media*. Wiley, 1988.

[102] J. D. Joannopoulos, S. G. Johnson, J. N. Winn, and R. D. Meade, "Photonic crystals: Molding the flow of light," *Photonic Crystals: Molding the Flow of Light (Second Edition)*, 10 2011.

[103] L. Xiong, J. M. Ruddock, and G. J. Diebold, "Photoacoustic transients generated by laser irradiation of thin films," *Photoacoustics*, vol. 3, pp. 60–63, 6 2015.

[104] B. E. Treeby and B. T. Cox, "Modeling power law absorption and dispersion in viscoelastic solids using a split-field and the fractional laplacian a),"

[105] J. M. Pinkerton, "The absorption of ultrasonic waves in liquids and its relation to molecular constitution," *Proceedings of the Physical Society. Section B*, vol. 62, p. 129, 2 1949.